UNIVERSIDADE ESTADUAL DE CAMPINAS
Instituto de Geociências

LEONARDO BRENGUERE LEÃO LOPES

EVOLUÇÃO TERMOCRONOLÓGICA E REATIVAÇÕES RÚPTEIS DA ZONA DE CISALHAMENTO PERNAMBUCO, PROVÍNCIA BORBOREMA, BRASIL

LOW-TEMPERATURE THERMOCHRONOLOGY AND BRITTLE REACTIVATIONS OF THE PERNAMBUCO SHEAR ZONE, BORBOREMA PROVINCE, BRAZIL

CAMPINAS

2023

UNIVERSIDADE ESTADUAL DE CAMPINAS
Instituto de Geociências

LEONARDO BRENGUERE LEÃO LOPES

EVOLUÇÃO TERMOCRONOLÓGICA E REATIVAÇÕES RÚPTEIS DA ZONA DE CISALHAMENTO PERNAMBUCO, PROVÍNCIA BORBOREMA, BRASIL

LOW-TEMPERATURE THERMOCHRONOLOGY AND BRITTLE REACTIVATIONS OF THE PERNAMBUCO SHEAR ZONE, BORBOREMA PROVINCE, BRAZIL

DISSERTAÇÃO APRESENTADA AO INSTITUTO DE GEOCIÊNCIAS DA UNIVERSIDADE ESTADUAL DE CAMPINAS PARA OBTENÇÃO DO TÍTULO DE MESTRE EM GEOCIÊNCIAS NA ÁREA DE GEOLOGIA E RECURSOS NATURAIS

DISSERTATION PRESENTED TO THE INSTITUTE OF GEOSCIENCES OF THE UNIVERSITY OF CAMPINAS TO OBTAIN THE DEGREE OF MASTER IN GEOSCIENCES IN THE AREA OF GEOLOGY AND NATURAL RESOURCES

ORIENTADOR: Prof. Dr. Wagner da Silva Amaral

ESTE EXEMPLAR CORRESPONDE À VERSÃO FINAL DA DISSERTAÇÃO DEFENDIDA PELO ALUNO LEONARDO BRENGUERE LEÃO LOPES E ORIENTADA PELO PROF. DR. WAGNER DA SILVA AMARAL

CAMPINAS

2023

Ficha catalográfica
Universidade Estadual de Campinas
Biblioteca do Instituto de Geociências
Marta dos Santos - CRB 8/5892

Informações Complementares

Título em outro idioma: Low-temperature thermochronology and brittle reactivations of the Pernambuco shear zone, Borborema Province, Brazil
Palavras-chave em inglês:
Low-temperature thermochronology
Fission track
Apatite
Área de concentração: Geologia e Recursos Naturais
Titulação: Mestre em Geociências
Banca examinadora:
Wagner da Silva Amaral [Orientador]
Elson Paiva de Oliveira
Tiago Amâncio Novo
Data de defesa: 27-04-2023
Programa de Pós-Graduação: Geociências

Identificação e informações acadêmicas do(a) aluno(a)
- ORCID do autor: https://orcid.org/0000-0001-7053-2502
- Currículo Lattes do autor: http://lattes.cnpq.br/3473466080821646

UNIVERSIDADE ESTADUAL DE CAMPINAS

INSTITUTO DE GEOCIÊNCIAS

AUTOR: Leonardo Brenguere Leão Lopes

Evolução termocronológica e reativações rúpteis da Zona de Cisalhamento Pernambuco, Província Borborema, Brasil

Low-temperature thermochronology and brittle reactivations of the Pernambuco Shear Zone, Borborema Province, Brazil

ORIENTADOR: Prof. Dr. Wagner da Silva Amaral

Aprovado em: 27 / 04 / 2023

EXAMINADORES:

Prof. Dr. Wagner da Silva Amaral - Presidente

Prof. Dr. Tiago Amâncio Novo

Prof. Dr. Elson Paiva de Olivêira

A Ata de Defesa assinada pelos membros da Comissão Examinadora consta no processo de vida acadêmica do aluno.

Campinas, 27 de abril de 2023.

SÚMULA CURRICULAR

Leonardo Brenguere Leão Lopes

Geólogo (2013) pelo Instituto de Geociências da Universidade de São Paulo (USP), onde trabalhou com petrologia de rochas ígneas e metamórficas do sul de Minas Gerais, além de temas como isótopos instáveis e cartografia geológica. Mestre (2023) pelo Instituto de Geociências da Universidade Estadual de Campinas (Unicamp) onde trabalhou com termocronologia de baixa temperatura aplicada terrenos do Precambriano e reativações rúpteis na Província Borborema, NE Brasil.

Desde 2014, é pesquisador em geociências do Serviço Geológico do Brasil-CPRM (SGB), onde tem desenvolvido projetos regionais envolvendo mapeamento geológico, evolução tectônica de terrenos de alto grau metamórfico, granitogênese e metalogenia do ouro na porção norte do Estado do Mato Grosso (Província Mineral de Alta Floresta), na Bahia (Cráton São Francisco - Bloco Gavião Sul e adjacências) e na Província Borborema e Faixa Sergipana (Estados de Pernambuco e Sergipe). Atualmente integra a equipe do Centro de Geociências Aplicadas (CGA, antigo CEDES) no Escritório do Rio de Janeiro, responsável por projetos nacionais envolvendo inovação e tecnologia do setor de óleo e gás e da mineração, além da construção e implementação de laboratórios e rotinas analíticas.

AGRADECIMENTOS

RESUMO

O embasamento da Província Borborema (NE do Brasil) foi afetado por deformações durante o Fanerozóico, em resposta a pulsos tectônicos, bem como a eventos magmáticos, levando eventos de soerguimento e culminando com o rompimento de Gondwana Ocidental. Esses eventos combinados também levaram à formação de bacias intracontinentais, como Jatobá, Araripe e Rio do Peixe, com contexto deposicional e controles estruturais semelhantes. Essas bacias estão intrinsecamente relacionadas com as principais zonas de cisalhamento de escala continental do Ediacarano da Província Borborema, que foram reativadas durante o Fanerozóico. O momento, a duração e os mecanismos responsáveis por essas reativações ainda são incertos. Neste estudo, usamos termocronologia de baixa temperatura para obter as idades dos eventos de resfriamento e possíveis reativações da zona de cisalhamento de Pernambuco. O estudo se baseia em quinze novos resultados de traços de fissão de apatita (TFA), oito amostras de traços de fissão em zircão (TFZ) e doze amostras de apatita pelo método (U-Th)/He (AHe), do embasamento cristalino da Província Borborema e da Bacia de Jatobá, ao longo do *trend* leste-oeste da zona de cisalhamento Pernambuco. Os resultados mostram uma concentração de idades TFA no limite Jurássico–Cretáceo, com idades centrais variando de 80,4 ± 14,3 a 199,5 ± 13,3 Ma e com comprimentos de traços confinados médios variando de 10,82 ± 1,71 a 12,67 ± 1,32 µm. Os resultados TFZ resultaram em idades centrais que variam de 420,6 ± 64,2 a 752,2 ± 53,6 Ma. Os resultados de AHe mostram uma grande variação dentro das amostras, e as idades médias variam de 38 ± 22 a 103 ± 26 Ma. Modelagem inversa de história térmica de oito amostras do embasamento sugerem que durante o Paleozóico a área de estudo experimentou resfriamento acelerado após o ciclo orogênico do Brasiliano até o Siluriano–Devoniano, com taxas de resfriamento de 1,5 a 8,0 °C/m.a. Por outro lado, resfriamento monotônico foi registrado desde ca. 250–200 Ma para quase todas as amostras, enquanto as amostras mais próximas da falha de Ibimirim, a falha de borda da bacia de Jatobá, revelam um evento de resfriamento em ca. 140–115 Ma. Tal evento de resfriamento é interpretado como um evento de denudação associado à erosão sin-rifte de topografia preexistente, ligada à separação entre a América do Sul e a África. Além disso, modelagem térmica do conglomerado da falha de borda da Bacia de Jatobá revelou temperaturas máximas de soterramento de 70–105 °C até ca. 100–85 Ma. Usando estimativas de gradientes paleogeotérmicos médios, pode-se inferir que a Bacia de Jatobá experimentou uma denudação pós-rifte de aproximadamente 1,4 a 2,8 km de pilha sedimentar.

Palavras-chave: termocronologia de baixa temperatura; Província Borborema; zona de cisalhamento Pernambuco

ABSTRACT

The basement of Borborema Province (NE Brazil) was affected by deformation during the Phanerozoic, in response to tectonic pulses as well as magmatic events, leading to uplift and the West Gondwana break-up. These combined events also led to the formation of intracontinental basins, such as Jatobá, Araripe, and Rio do Peixe, with similar depositional context and structural controls. These basins are intrinsically related to major Ediacaran, continental-scale shear zones of the Borborema Province that were reactivated during the Phanerozoic. The timing, duration and driving forces of these reactivations are still an ongoing debate. In this study we use low-temperature thermochronology to constrain the timing of cooling and possible reactivations of the Pernambuco shear zone. We report on fifteen new apatite fission-track (AFT), eight zircon fission-track (ZFT) and twelve apatite (U-Th)/He (AHe) samples from both the Borborema Province crystalline basement and the Jatobá Basin, along the E-W structural trend of the Pernambuco shear zone. The results display a concentration of AFT ages in the Jurassic–Cretaceous boundary, with central ages ranging from 80.4 ± 14.3 to 199.5 ± 13.3 Ma and with mean track lengths ranging from 10.82 ± 1.71 to 12.67 ± 1.32 µm. ZFT results yield central ages spanning from 420.6 ± 64.2 to 752.2 ± 53.6 Ma. AHe results show a wide single grain ages variation within samples, and mean ages vary from 38 ± 22 to 103 ± 26 Ma. Inverse thermal modeling of eight basement samples suggests that during the Paleozoic the study area experienced accelerated cooling after the orogenic cycle until the Silurian–Devonian, with cooling rates from 1.5 to 8.0 °C/m.y. In contrast, monotonic cooling has been registered since ca. 250–200 Ma for almost all samples whereas samples closer to the Ibimirim fault, the border fault of the Jatobá basin, experienced a cooling event at ca. 140–115 Ma. Such a cooling event is interpreted as a denudation event associated with syn-rift erosion of preexisting topography, linked to the separation between South America and Africa. In addition to that, inverse thermal modeling of the conglomerate from the border fault of the Jatobá Basin revealed maximum burial temperatures of 70–105 °C until ca. 100–85 Ma. Using average paleogeothermal gradients estimates, we can infer that the Jatobá Basin experienced a post-rift denudation of approximately 1.4 to 2.8 km of sedimentary pile.

Keywords: low-temperature thermochronology; Pernambuco shear zone; Borborema Province

SUMÁRIO

CAPÍTULO 1

1. Aspectos introdutórios

Essa dissertação está inserida no contexto do projeto de P,D&I de ciência básica intitulado "Herança orogênica no controle da deformação intraplaca e desenvolvimento de bacias sedimentares durante a abertura do Oceano Atlântico no NE do Brasil." (processo 2018/00429-0). Esse projeto tem financiamento da Petrobras e o Serviço Geológico do Brasil é o principal órgão executor, com a Universidade Estadual de Campinas como parceira. Trata-se de um projeto multidisciplinar, com atuação principal na deformação rúptil da Província Borborema, no nordeste do Brasil (**Fig. 1**). Um dos objetivos do projeto é a datação direta dos eventos rúpteis (falhas) da Província Borborema. Com isso, as zonas de cisalhamento que foram reativadas principalmente durante o rifte do Cretáceo foram objeto de estudos, tanto as suas falhas, quanto as regiões do embasamento adjacente. Para dar suporte aos dados das idades das movimentações das falhas (obtidos com métodos de datação direta, como U-Pb em carbonato), optou-se por fazer um estudo nas regiões adjacentes com os métodos de termocronologia de baixa temperatura (40–300 °C) para avaliar as épocas de resfriamento acelerado e o comportamento térmico dessas descontinuidades crustais. A presente dissertação é um estudo de caso dessa abordagem na zona de cisalhamento Pernambuco e na região adjacente da Bacia de Jatobá.

Com isso é possível obter uma visão holística do estado termal da zona de cisalhamento Pernambuco e a área adjacente da Bacia de Jatobá desde o Paleozoico até o presente. Com a evolução térmica obtida a partir da modelagem da termocronologia de baixa temperatura, pode se avaliar os períodos de resfriamento acelerado, além dos períodos de aquecimento, inferindo sobre os processos de maior comprimento de onda (e.g., soerguimento/subsidência, atividade mantélica anômala, resistência lateral à deformação da placa) e dando substrato às interpretações de movimentação vertical de blocos na região de estudo.

2. Justificativa

A termocronologia de baixa temperatura vêm sendo empregada na Província Borborema e das bacias do Recôncavo, Tucano e Jatobá na abordagem das histórias de resfriamento e a evolução do relevo (Harman et al., 1998; Japsen et al., 2012; Jelinek et al., 2014, 2020; Morais Neto et al., 2006, 2009; Turner et al., 2008). Em resumo, esses estudos têm demonstrado que quatro estágios de resfriamento acelerado e exumação foram registrados na região: (1) quase todos os estudos sugeriram resfriamento acelerado durante o Cretáceo Inferior (ca. 130 a 90 Ma), que geralmente está relacionado a denudação da margem durante o rifteamento que culminou com a ruptura continental e a separação da América do Sul e da África; (2) um evento de resfriamento rápido do Cretáceo Superior–Paleógeno (ca. 80–60 Ma) foi relatado por Harman et al. (1998) e Japsen et al. (2012). Harman et al. (1998) propõem uma reativação da zona de cisalhamento de Pernambuco durante esse tempo, e relacionam isso a mudanças nos movimentos relativos das placas da América do Sul, África e Antártica. Por outro lado, Japsen et al. (2012) argumentam que houve soerguimento no nordeste do Brasil naquela época e foi causado pela resistência lateral ao movimento das placas, uma vez que é contemporâneo a uma diminuição na taxa de espalhamento da Cordilheira Meso-Atlântica e aos ciclos orogênicos dos Andes; (3) Japsen et al. (2012) e Turner et al. (2008) também propuseram um evento de resfriamento/soerguimento acelerado durante o Eoceno (ca. 48–38 Ma); (4) outro evento de resfriamento em ca. 20 Ma até os dias atuais é relatada por quase todos os autores usando

traços de fissão em apatita na Província Borborema, contudo não há consenso quanto às possíveis causas.
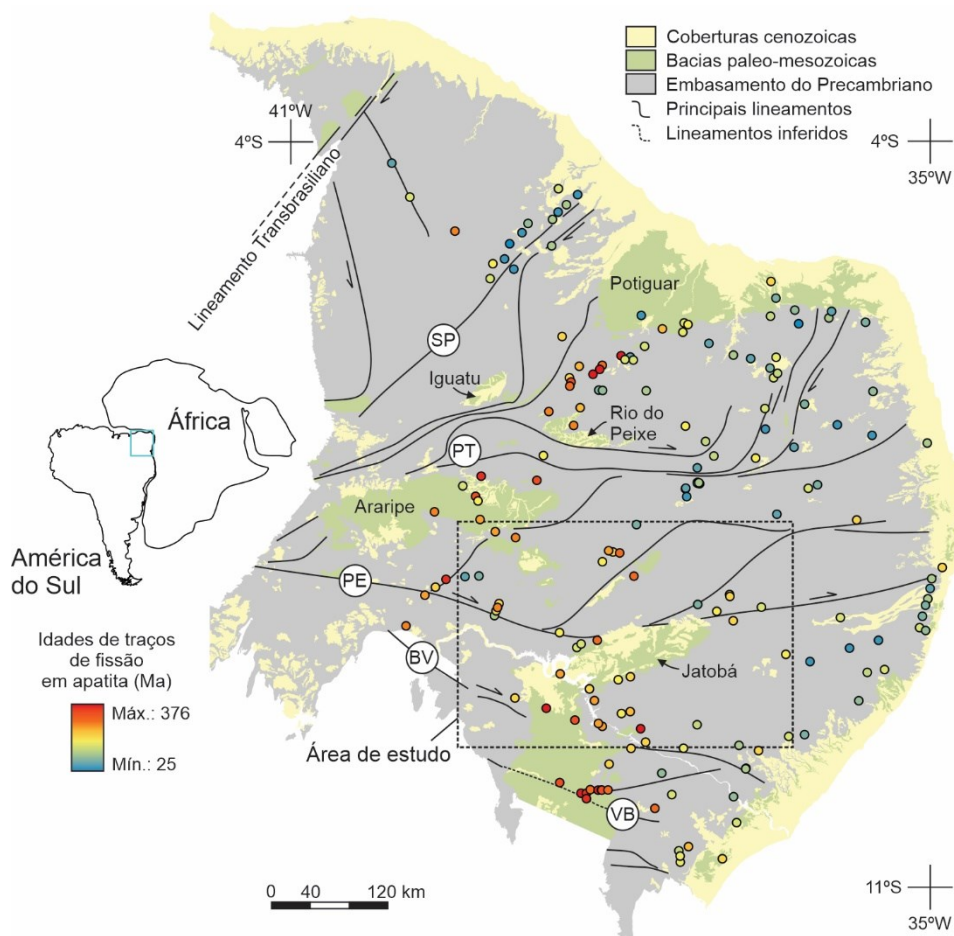
Fig. 1. Mapa simplificado com as principais estruturas e as bacias interiores da Província Borborema, baseado em Santos et al. (2021). As amostras de traços de fissão em apatita compiladas estão detalhadas no material suplementar. Os lineamentos prinpais são: zonas de cisalhamento (SP) Senador Pompeu, (PT) Patos, (PE) Pernambuco e (BV) Boa Vista, e a zona de transferência de Vaza Barris (VB).

Contudo, os trabalhos citados anteriormente tiveram pouco foco nas reativações rúpteis e na movimentação vertical de blocos da Província Borborema. Além disso, há evidências substanciais de reativações rúpteis das zonas de cisalhamento do nordeste do Brasil e até mesmo inversões de bacias interiores, como é o caso da Rio do Peixe e da Potiguar (Bezerra et al., 2011, 2020; Lima Neto et al., 2013; Vasconcelos et al., 2021). Nesse sentido, o objeto de estudo dessa dissertação é uma zona de cisalhamento de escala continental, a zona de cisalhamento Pernambuco (**Fig. 1**). O entendimento do comportamento térmico e do resfriamento das diferentes porções da zona de cisalhamento Pernambuco e da região adjacente da Bacia de Jatobá é fundamental para entender como e quando essas reativações aconteceram. Além do mais, a modelagem térmica de rochas de bacias sedimentares é importante para o entendimento do soterramento e posterior denudação das bacias, além de aspectos econômicos como a janela de maturação de óleo e gás.

3. Objetivos

Os objetivos dessa dissertação são:

1) Caracterização dos eventos de resfriamento utilizando a termocronologia de baixa temperatura, principalmente traços de fissão e (U-Th)/He, no estudo ao longo da zona de cisalhamento Pernambuco e a área adjacente da Bacia de Jatobá;

2) Tentativa de datar os eventos de movimentação vertical de blocos ao longo de zona de cisalhamento Pernambuco usando os métodos de termocronologia de baixa temperatura, ou pelo menos delimitar os períodos de resfriamento acelerado em que essa região foi submetida;

3) Comparar a história térmica obtida com traços de fissão em zircão com a história obtida a partir de $^{40}Ar/^{39}Ar$ compilada da literatura;

4) Modelar a história térmica dos sedimentos sin-rifte da Bacia de Jatobá.

4. Estrutura da dissertação

Esse trabalho de dissertação está dividido entre o capítulo introdutório, onde há a exposição dos aspectos introdutórios, justificativa e objetivos. O capítulo 2 é composto de uma revisão dos métodos de termocronologia de baixa temperatura, com aspectos simplificados, além de uma seção descrevendo a modelagem inversa. A parte final do capítulo 2 é a descrição detalhada dos processos de separação mineral utilizados pelo autor durante a dissertação. Os processos de separação mineral variam entre laboratórios, os aqui descritos foram utilizados pelo autor no Centro de Geociências Aplicadas no Escritório do Rio de Janeiro do Serviço Geológico do Brasil.

O capítulo 3 é um manuscrito em inglês intitulado "Low-temperature thermochronology and brittle reactivations of the Pernambuco Shear Zone, Borborema Province, Brazil" que será submetido para uma revista internacional. Nele contém os novos dados obtidos durante a dissertação, além de toda a descrição complementar dos métodos, o contexto geológico regional e as discussões. A seção *References* no final deste trabalho possui todas as referências de todos os capítulos. Os dados brutos, diagramas complementares e tabelas com os dados compilados estão contidos nos dados suplementares (*Supplementary material*).

CAPÍTULO 2

Métodos de termocronologia de baixa temperatura e suas aplicações

Nesta seção, as principais características da termocronologia de baixa temperatura serão brevemente apresentadas, com ênfase nos dois métodos principais: (1) traços de fissão (TF) e (2) (U-Th)/He (He). Esses métodos são baseados no decaimento espontâneo do urânio (U) e tório (Th) e são aplicados a minerais portadores desses elementos, sendo os principais apatita e zircão.

Todos os métodos de datação isotópica são de certa forma sensíveis à temperatura, e temperatura na qual um mineral, para um dado sistema, começa a registrar sua idade foi definida após Dodson (1973) introduzir o conceito de "temperatura de fechamento" (T_c), definido pela temperatura correspondente à idade aparente de um mineral. Entretanto, os traços de fissão, que são defeitos no retículo cristalino de um mineral formados continuamente a partir do decaimento do urânio, podem sofrer apagamento (os comprimentos das traços são encurtados) sobre determinados intervalos de temperatura. Se o resfriamento da amostra ocorrer de maneira gradual, o intervalo de temperatura em que ocorre o apagamento dos traços é denominado como a "zona de apagamento parcial" (ZAP) (em inglês: *partial annealing zone* - PAZ), ou seja, é o intervalo entre o encurtamento total dos traços (mais alta temperatura) e a preservação total do comprimento dos traços (mais baixa temperatura). Com isso, a idade de TF aparente de um mineral não será relativa a uma temperatura de fechamento mas relativa a esse intervalo. No caso do He, o mesmo conceito de um intervalo de temperatura entre a retenção total de He no retículo do mineral e a perda total do He por difusão, é conhecido como "zona de retenção parcial" (ZRP). Ambos os intervalos de temperatura irão variar com o mineral em questão, e elas serão detalhadas nas seções abaixo. Somente quando uma amostra sofre resfriamento de forma relativamente rápida através do ZAP ou ZRP, o conceito de temperatura de fechamento (T_c) pode ser usado (Dodson 1973). Embora seja útil na comparação entre os resultados de diferentes métodos termocronológicos, a premissa de um resfriamento rápido nem sempre é válida em terrenos cratônicos e faixas móveis que se encontram estáveis por muito tempo, onde as amostras podem ter estado por longos períodos nestas zonas, gerando algumas complicações para a interpretação dos resultados (e.g., Guenthner et al., 2013; Reiners, 2005). Além disso, o T_c, e o intervalo de temperatura de retenção do produto de decaimento radioativo, podem variar em função de diferentes fatores como dano por radiação, química mineral, o volume do grão e taxa de resfriamento (e.g., Fitzgerald & Malusà, 2019; Gleadow et al., 2002; Guenthner et al., 2013; Reiners, 2005; Shuster et al., 2006).

Com base nessas fundamentações, a termocronologia de baixa temperatura tem auxiliado na resolução de questões geológicos, além da evolução térmica e o resfriamento de terrenos nos mais diversos ambientes geológicos (e.g., Malusà & Fitzgerald, 2019), como: margens passivas continentais (e.g., Wildman et al., 2019), crátons (e.g., Kohn & Gleadow, 2019), orógenos (e.g., Schildgen & van der Beek, 2019), na exploração de hidrocarbonetos (e.g., Schneider & Issler, 2019) e no estudo de falhas (e.g., Tagami, 2019).

A época de movimentações de blocos, idades das falhas e suas características térmicas podem ser inferidos por métodos de termocronologia de baixa temperatura, seja com modelagem térmica estimando o *reset* (total ou parcial) dos cronômetros dentro de zonas de falha (e.g., Tagami, 2005, 2012, 2019), ou analisando a história térmica em perfis regionais de diferentes blocos separados por falhas, comparando seus modelos térmicos de exumação

diferencial (Stockli, 2005; Stockli et al., 2000). No trabalho de Tsukamoto et al. (2020) há uma compilação de diferentes técnicas de datação de falhas. Os autores ainda apresentam as temperaturas de fechamento de vários métodos de datação (para gradientes térmicos e taxas de resfriamento regulares) que são apresentadas na **Tabela 1**. No entanto, para resetar um cronômetro em um terreno já resfriado durante um evento instantâneo de aquecimento (e.g., terremoto), é necessário temperaturas muito mais altas durante um longo intervalo de tempo do que as apresentadas abaixo (Tagami, 2012).

Tabela 1. Temperatura de fechamento (T_c) e energia de ativação para os principais cronômetros utilizados para datação de rochas de falhas e para evolução térmica de terrenos. Baseado em Grün et al. (1999), Herman et al. (2010), King et al. (2016) e Reiners et al. (2005).

Sistema	Mineral	Temp. de fechamento (°C)	Energia de ativação (kJ/mol)
$^{40}Ar/^{39}Ar$ (K-Ar)	Hornblenda	500–600	270
	Biotita	350–400	210
	Muscovita	300–350	180
	Ilita	~ 260	220
	Feldspato K	150–350	170–210
Traços de fissão	Titanita	240–300 380–420	440–480
	Zircão	330–350	330–350
	Apatita	90–120	190
(U-Th)/He	Titanita	160–220	190
	Zircão	160–200	170
	Apatita	50–115	140
Ressonância de spin eletrônico	Quartzo	50–80	-
Luminescência (LOE)	Feldspato	40–90	-
	Quartzo	30–35	-

1. Traços de fissão

O método de traços de fissão (TF) é uma técnica de termocronologia de baixa temperatura aplicada na reconstrução e evolução do relevo, análise térmica de bacias, modelagem numérica de terrenos e erosão, intemperismo, denudação e soerguimento (e.g., Malusà & Fitzgerald, 2019). Os traços de fissão são pequenos defeitos cristalinos no retículo que se formam a partir do decaimento espontâneo do ^{238}U pela fissão nuclear, acumulando-se ao longo do tempo em minerais ricos em U (Tagami & O'Sullivan, 2005). Para medir o tempo desde que começaram a se acumular, deve-se determinar a quantidade de ^{238}U por unidade de volume (isótopo pai), bem como o número de traços de fissão espontânea por unidade de volume (no caso um *proxy* do isótopo filho). Basicamente, existem dois métodos utilizados para obter as idades de TF: 1) o método tradicional do detector externo (*external detector method* - EDM) (e.g., Donelick et al., 2005); e 2) ou o método por LA-ICP-MS (Hasebe et al., 2004). Na **Fig. 1** é apresentado um diagrama esquemático contendo os protocolos básicos de preparação da amostra e de análise de cada método. O EDM basicamente consiste na contagem de traços de fissão espontâneos na superfície polida do grão e os traços induzidos em um detector externo (geralmente uma mica que não possui ^{238}U) que é fixado em contato direto com o *mount* dos grãos. Ambos passam por irradiação em um reator nuclear. O processo de irradiação induz a produção de traços de fissão a partir do conteúdo de ^{235}U contido no grão, que irão penetrar a superfície do detector externo (mica). A densidade de traços induzidos por ^{235}U é usada como *proxy* para o conteúdo de ^{238}U no grão. Por fim, as densidades dos traços espontâneos é calculada no mineral (isótopo filho) e

a dos traços induzidos é contada no detector externo (isótopo pai). Elas serão usadas na equação da idade individual de cada grão (Donelick et al., 2005). Por outro lado, o método LA-ICP-MS é mais rápido, porque não é necessária a irradiação, além de evitar o manuseio de material radioativo. O método consiste basicamente em calcular a densidade de traços espontâneos no mineral de interesse e depois medir o conteúdo de ^{238}U na mesma área contada através de LA-ICP-MS (Donelick et al., 2005; Hasebe et al., 2004; Soares et al., 2014). Para ambos os métodos, são medidos traços confinados (em inglês, *mean track length* - MTL), que são traços espontâneos horizontais que estão abaixo da superfície exposta do cristal. Além da medida, mede-se o ângulo entre esse traço e o eixo C do grão, além do Dpar (diâmetro do buraco do traço atacado com a superfície, em μm) próximo ao traço. Esses valores são usados para estimar a quantidade de apagamento parcial (*partial annealing*) a qual uma amostra foi submetida, e são importantes para a construção dos modelos térmicos (Donelick et al., 2005).
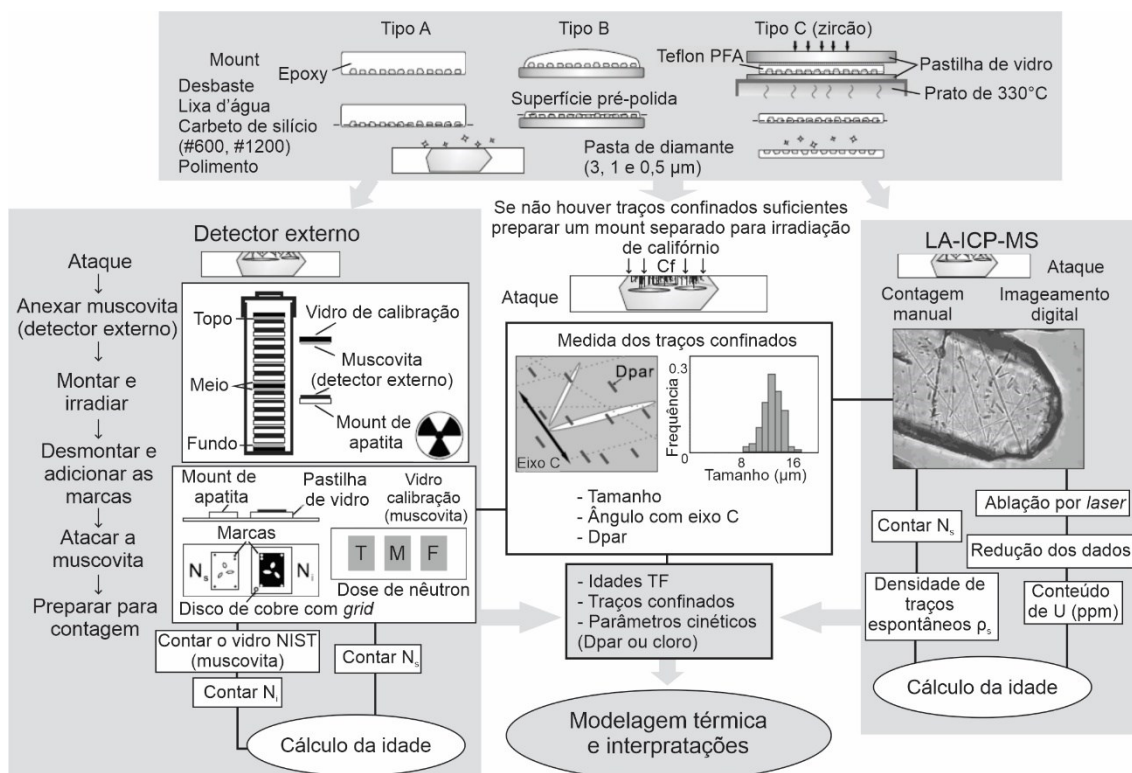
Fig. 1. Protocolos para análises de traços de fissão e preparação das amostras pelo detector externo (EDM) e por LA-ICP-MS modificado de Kohn et al. (2019). Dpar é medido paralelamente ao eixo cristalográfico C do mineral. N_s são os traços de fissão espontâneos do mineral e N_i são os traços induzidos contados na muscovita. ρ_s é a densidade de traços espontâneos (traços/cm^2). Para maiores detalhes, consultar Kohn et al. (2019).

Minerais em altas temperaturas não acumulam traços de fissão, porque qualquer traços formados são rapidamente apagados pela reorganização da rede cristalina. Quando um mineral começa a esfriar e passa ZAP, os traços de fissão começam a se acumular e a sofrer apagamento (Donelick et al., 2005). O processo de recozimento consiste na diminuição do comprimento do traço de fissão durante um intervalo de temperatura. Para apatita, que é sistema mais bem compreendido e mais comumente usado, a o intervalo de temperatura da ZAP varia entre aproximadamente 60 e 110 °C para um período de aquecimento de aproximadamente 10 m.a, mas isso também pode variar, por isso é necessário considerar os parâmetros composicionais de cada grão como a quantidade de cloro, ou uma *proxy* para esse conteúdo, o parâmetro cinético Dpar. Já para o traço de fissão em zircão, a ZAP varia entre aproximadamente 180 e 350

°C para aproximadamente 10 m.a. de aquecimento (e.g.,Tagami, 2005), mas esse intervalo varia com o grau de dano por radiação que o grão foi submetido.

No caso do estudo de zonas de falha, alguns trabalhos relataram casos com diminuições nos comprimentos dos traços e mudanças nas idades de TF em direção à zona de falha (Fernie et al., 2018; Heineke et al., 2019; Murakami et al., 2006; Murakami & Tagami, 2004; Wölfler et al., 2010). Além disso, alguns autores argumentam que é necessário um evento de cisalhamento e/ou aquecimento por fricção por tempo suficientemente longo, juntamente com a circulação eficiente de fluido, para que o sistema possa sofrer *reset* parcial no caso de TF em apatita e zircão (Tagami, 2012; Tsukamoto et al., 2020).

2. (U-Th)/He

O método é baseado nos produtos de decaimento radiométrico alfa (α) da cadeia do ^{238}U, ^{235}U, ^{232}Th e ^{137}Sm, resultando em partículas de ^{4}He que ficam retidas no retículo cristalino do mineral. (Farley, 2002; Reiners, 2005; Zeitler et al., 1987). O conceito do método é basicamente o mesmo descrito acima no TF, contudo em altas temperaturas o mineral não retém o ^{4}He produzido, que é perdido por difusão. Quando o mineral começa a esfriar e entra no intervalo definido como a zona de retenção parcial (ZRP), o ^{4}He começa a ser parcialmente acumulado. Quando um mineral atinge uma temperatura abaixo desse intervalo, todo o ^{4}He produzido é acumulado no mineral. A apatita fornece informações sobre temperaturas mais baixas em relação ao TF, com a ZRP de apatita entre 35 e 85 °C aproximadamente, em períodos de aquecimento relativamente curtos (Farley & Stockli, 2002). Já para zircão, o intervalo de temperatura da ZRP é de aproximadamente 130 a 200 °C (Reiners, 2005). Portanto, os intervalos de temperatura de retenção do isótopos filho em apatita e zircão tanto no sistema de TF e como (U-Th)/He são complementares e fornecem informações relevantes da história térmica da porção mais rasa da crosta continental (aproximadamente menos de 10 km) (Kohn & Gleadow, 2019).

A análise para se obter uma idade de (U-Th)/He consiste em aquecer o grão em uma linha de extração de gás à vácuo, liberando o ^{4}He que é medido em um espectrômetro de massas. Depois disso, o grão é dissolvido em ácido com traçadores e as quantidades de ^{238}U, ^{235}U, ^{232}Th e ^{137}Sm são medidas, geralmente em outro espectrômetro de massa, obtendo-se então uma idade individual de um grão. No geral, para uma amostra são realizadas as análises de 5 a 10 grãos, a depender da variação(Flowers & Kelley, 2011; Green & Duddy, 2018). Devido a ejeção de partículas α (^{4}He) a distâncias aproximadamente entre 10 a 20 μm, a camada mais exterior de um grão pode apresentar isótopos pai sem um isótopo filho. Para isso, é feito uma correção (F_T) na idade obtida que será uma função do volume do grão (Farley et al., 1996). Além disso, é bastante comum que exista variação das idades individuais dentro de uma mesma amostra. Para isso, é necessário avaliar fatores que podem explicar essa variabilidade, principalmente o dano por radiação, que é quantificado pelo conteúdo efetivo de urânio de uma amostra (eU=[U]+0.235*[Th]), e o tamanho do cristal (Farley, 2000; Flowers et al., 2009; Flowers & Kelley, 2011; Gautheron et al., 2009; Stockli et al., 2000). Outros fatores que podem explicar essa variação são: inclusões ricas em U-Th (Farley, 2002; Lippolt et al., 1994), implantação de ^{4}He por outros minerais próximos (Spiegel et al., 2009) e zonamento de U e Th (Farley, 2002).

Para realizar reconstruções de histórias termais complexas, uma abordagem multimétodo é desejável, datando as mesmas amostras por diferentes métodos (e minerais), estabelecendo marcadores termocronológicos e permitindo modelos mais robustos (Ketcham, 2019). Outra abordagem seria datar rochas diferentes ao longo perfil topográfico ou ao longo de blocos estruturais que foram movimentados, usando o mesmo método isotópico (Stockli et al., 2000). Em relação a movimentos da falha, o aquecimento por fricção e a percolação de fluidos ao longo de zona de falha podem resetar total ou parcialmente o sistema (U-Th)/He em alguns casos (e.g., Maino et al., 2015; Yamada et al., 2012). Além disso, avanços recentes na datação de hematita em planos de falha pelo método (U-Th)/He abrem novas perspectivas para os estudos da evolução termocronológica dos movimentos de falha (Ault et al., 2015).

3. Modelagem de história térmica

As modelagens de história térmica progressiva e inversa são usadas para extrair modelos geológicos de resfriamento e/ou aquecimento que melhor correspondam aos dados de termocronologia de baixa temperatura adquiridos para uma amostra (Ketcham, 2005). Os dois principais *softwares* utilizados pela comunidade de termocronologia são HeFTy (Ketcham, 2005) e QTQt (Gallagher, 2012). Uma avaliação estatística com comparação de alguns resultados foi realizada por Vermeesch & Tian (2014) e gerou um debate sobre as metodologias (Gallagher & Ketcham, 2018; Vermeesch & Tian, 2018). Os dados de entrada para os modelos de TF em apatita são: 1) idade individual de cada grão e o Dpar médio do grão, 2) medida de cada traço confinado, o seu ângulo com o eixo c e o Dpar. Para uma melhor confiabilidade do modelo, sugere-se uma quantidade de 100 traços confinados. Para os dados de He (apatita e zircão): 1) o tamanho do grão (raio equivalente calculado), 2) o conteúdo de U e Th, e 3) a idade e a incerteza não corrigida. Outro passo importante é adicionar *constraints* geológicos para impor restrições a possíveis histórias térmicas. São caixas de tempo e temperatura em que obrigatoriamente o modelo deve passar por elas. Esses *constraints* são definidos a partir da histórica geológica da região, como por exemplo uma não conformidade em que uma camada sedimentar com idade de deposição conhecida está em contato direto com uma rocha do embasamento que será modelada. Outro caso é de rocha vulcânica extrusiva que tem sua idade conhecida e está em contato direto com o embasamento. Em ambos os casos, é possível afirmar que o embasamento estava próximo da superfície naquele momento (deposição ou extrusão) (e.g., Ketcham, 2005; Ketcham et al., 2018; Ksienzyk et al., 2014). Outros métodos podem ainda ajudar a limitar a temperatura máxima a qual uma camada sedimentar foi submetida, como é o caso da reflectância de vitrinita (e.g., Morais Neto et al., 2006).

A compreensão atual dos mecanismos cinéticos por trás do sistema de TF em apatita é melhor do que os outros sistemas. Por isso, um protocolo de modelagem que é geralmente seguido é que cada amostra seja primeiro modelada apenas com os dados TF de apatita (e.g., Ksienzyk et al., 2014). Usando TF em apatita como um guia geral do comportamento térmico da amostra, é inserido posteriormente os dados de He de apatita, de depois os dados de He em zircão, de modo que possa ser feita uma comparação de todos os resultados do modelo para garantir confiabilidade (Kohn & Gleadow, 2019). Devido às complexidades do método de He, sempre que possível múltiplos termocronômetros devem ser utilizados para fornecerem informações adicionais para que modelos mais confiáveis sejam encontrados, particularmente em rochas antigas e que foram lentamente resfriadas (residiram na ZAP e ZRP por um longo período de tempo) (e.g., Anderson et al., 2017; Flowers & Kelley, 2011; Kohn & Gleadow, 2019). Além disso, como as idades de He frequentemente mostram grande dispersão intra-amostra, um protocolo de reamostragem pode ser também realizado utilizando um fator de escala para

algumas amostras menos precisas, mantendo-se o peso das idades observadas (Gallagher, 2012). Um exemplo de estudo com modelos térmicos contendo TF e He abordando resfriamento e reativações da margem continental passiva da África do Sul pode ser encontrado em Wildman et al. (2016). Outro exemplo multimétodo pode ser encontrado em Ksienzyk et al. (2014), com amostras da Noruega. Por fim, Ketcham et al. (2018) apresentam um estudo de reprodutibilidade dos dados de TF e He entre laboratórios, mostrando as melhores práticas para modelagem quando se trata de mais de um sistema.

4. Processos de separação mineral utilizados

Os métodos de separação de minerais pesados, em especial de apatita e zircão, realizados durante esse trabalho serão detalhados abaixo. Após a concentração dos minerais pesados, todos os outros processos foram realizados no laboratório ChronusCamp Research, em Itapira-SP, pelo analista Dr. Cleber Soares. Os processos, desde a montagem até as medidas dos isótopos no espectrômetro de massa, estão detalhados na seção 3 do manuscrito (capítulo 2) desta dissertação.

Para os métodos de termocronologia de baixa temperatura, é necessário recuperar um grande número de grãos intactos para a escolha do melhor grão para análise. Tanto para He como para TF, os cristais devem ser idealmente uniformes, sem zonamento e inclusões. É possível, no entanto, trabalhar com cristais zonados no caso do TF se houver um bom controle desse zonamento. Especialmente para o caso de He, os cristais escolhidos ainda devem ter idealmente as duas terminações, além de serem o maior possível, visto que a ejeção de partículas α serão mais preponderantes em grãos de menor volume (Farley et al., 1996). Contudo, se não for o caso, existem correções que são realizadas a fim de ajustar as idades obtidas. Outro cuidado que deve ser tomado é não criar um viés na escolha dos grãos. Na escolha de apenas grãos limpos e sem inclusões, pode haver a preferência para uma certa população de grãos. O ideal é que, para que haja representatividade das diferentes populações e reprodutibilidade dos dados, sejam separados grãos de todos os tipos, sem o viés de catação do analista.

A separação dos minerais pesados deste estudo foi realizada em sua totalidade pelo autor, parte na Universidade Estadual de Campinas (britagem e moagem) e parte no Serviço Geológico do Brasil (CPRM) no LAMIN-Escritório do Rio de Janeiro. As amostras foram colocadas em um triturador de mandíbulas e, em seguida, passaram por um moinho de disco, resultando em uma amostra de fração de areia mal selecionada. Uma parte essencial para a melhor concentração de grãos intactos é o peneiramento. As amostras foram peneiradas utilizando peneiras de malhas de 80, 125 e 250 mesh. A peneira de 80 mesh, por ser mais grossa e de metal, foi reutilizada após sua limpeza. Já as peneiras de 125 e de 250 mesh são feitas a partir de uma tela de nylon na respectiva granulometria, e após o seu uso são descartadas para evitar contaminação. A apatita e o zircão concentram-se mais na porção entre as peneiras de 125 e 250 mesh (125-250) e na porção menor que 250 mesh (<250). Estas duas porções foram então passadas em uma mesa de vibração e separação por gravidade chamada *Wilfley*. Nesta mesa, há a separação da porção mais densa das frações já peneiradas, resultando em uma diminuição da fração de amostra em aproximadamente 80%. Essa porção mais densa foi seca em estufa a 40 °C por 4 ± 1 horas. Depois disso, um forte ímã de neodímio foi usado para remover fragmentos de ferro, minerais magnéticos e outros minerais máficos como granada e biotita. Estima-se que o ímã de neodímio seja o equivalente ao separador magnético isodinâmico *Frantz* a 0,5 A. O concentrado resultante, já quase sem nenhuma fração de minerais máficos, foi despejado no líquido pesado bromofórmio (2,89 g/cm³) em uma capela. O material pesado foi

lavado com álcool e seco a 40 °C por 25 ± 10 minutos. Finalmente, o concentrado foi passado em um separador magnético isodinâmico *Frantz* a 1,5 A no Centro de Tecnologia Mineral (CETEM) no Rio de Janeiro. O conteúdo do concentrado final variou em relação à rocha que foi amostrada, mas no geral resultaram em sua maioria em grãos de apatita, zircão e rutilo.

CAPÍTULO 3

Low-temperature thermochronology and brittle reactivations of the Pernambuco Shear Zone, Borborema Province, Brazil

Abstract

The basement of Borborema Province (NE Brazil) was affected by deformation during the Phanerozoic, in response to tectonic pulses as well as magmatic events, leading to uplift and the West Gondwana break-up. These combined events also led to the formation of intracontinental basins, such as Jatobá, Araripe, and Rio do Peixe, with similar depositional context and structural controls. These basins are intrinsically related to major Ediacaran, continental-scale shear zones of the Borborema Province that were reactivated during the Phanerozoic. The timing, duration and driving forces of these reactivations are still an ongoing debate. In this study we use low-temperature thermochronology to constrain the timing of cooling and possible reactivations of the Pernambuco shear zone. We report on fifteen new apatite fission-track (AFT), eight zircon fission-track (ZFT) and twelve apatite (U-Th)/He (AHe) samples from both the Borborema Province crystalline basement and the Jatobá basin, along the E-W structural trend of the Pernambuco shear zone. The results display a concentration of AFT ages in the Jurassic–Cretaceous boundary, with central ages ranging from 80.4 ± 14.3 to 199.5 ± 13.3 Ma and with mean track lengths ranging from 10.82 ± 1.71 to 12.67 ± 1.32 μm. ZFT results yield central ages spanning from 420.6 ± 64.2 to 752.2 ± 53.6 Ma. AHe results show a wide single grain ages variation within samples, and mean ages vary from 38 ± 22 to 103 ± 26 Ma. Inverse thermal modeling of eight basement samples suggests that during the Paleozoic the study area experienced accelerated cooling after the orogenic cycle until the Silurian–Devonian, with cooling rates from 1.5 to 8.0 °C/m.y. In contrast, monotonic cooling has been registered since ca. 250–200 Ma for almost all samples whereas samples closer to the Ibimirim fault, the border fault of the Jatobá basin, experienced a cooling event at ca. 140–115 Ma. Such a cooling event is interpreted as a denudation event associated with syn-rift erosion of preexisting topography, linked to the separation between South America and Africa. In addition to that, inverse thermal modeling of the conglomerate from the border fault of the Jatobá basin revealed maximum burial temperatures of 70–105 °C until ca. 100–85 Ma. Using average paleogeothermal gradients estimates, we can infer that the Jatobá basin experienced a post-rift denudation of approximately 1.4 to 2.8 km of sedimentary pile.

1. Introduction

Passive continental margins have been marked by their apparent tectonic quiescence after their formation by intracontinental rifting and breakup (Lister et al., 1991; Ziegler & Cloetingh, 2004). This view, however, is being challenged by recent studies that shed light on the structural and thermal processes that operate during and after rifting, which impact on the long-term landscape development of not only the margin but also the hinterland, potentially creating a complex scenario of uplift and reactivation (Brune et al., 2014; Huismans & Beaumont, 2014; Paton, 2012; Salomon et al., 2015). Analyzing the surface response to rift and post-rift deformation over different length scales have key implications for models of continental margins that predict regional patterns of denudation influenced by regional base level fall, weathering and erosion, and also increased by long-wavelength epeirogenic/flexural uplift (e.g., Rodríguez Tribaldos et al., 2017; Sacek et al., 2019; Wildman et al., 2016).

In the northeastern portion of Brazil, there is an excellent example of the influence of post-rift processes in the formation of a passive continental margin. The Borborema Province (BP) (**Fig. 1**) has been the natural laboratory of an ever-increasing growing body of studies that assess the influence of both large- and short-wavelength processes that shape the landscape of a rifted continental margin (Klöcking et al., 2020; Morais Neto et al., 2009; Rodríguez Tribaldos et al., 2017; Sacek et al., 2019). It is noteworthy that uplift has been invoked in the BP, especially at the Araripe plateau, due to preservation of post-rift shallow-water marine sediments presently at 700–800 m above sea level, with a total post-rift sedimentation (from Aptian to Cenomanian) of a thickness up to ~770 m (Assine, 2007; Sacek et al., 2019). The thin lithospheric thickness (~60 km; Klöcking et al., 2020) alongside with the complex tectonic inheritance of dextral, crustal-scale shear zones orthogonal to the rifted margin, made the BP susceptible to vertical movements during the Cenozoic that are not always straightforward to comprehend.

The Pernambuco Shear Zone (PESZ) (**Fig. 1**) is one of those continental-scale, dextral shear zones that make up the BP framework in NE Brazil. Together with Patos, Cruzeiro do Nordeste, Congo, and Senador Pompeu (**Fig. 1**. and **Fig**. **2**), these shear zones functioned as important deformation corridors, localizing the strain during the amalgamation of Gondwana at the Ediacaran–Cambrian Brasiliano/Pan African Orogeny (Brito Neves et al., 1999; Caxito et al., 2020; Ganade et al., 2021). After the metamorphism and ductile deformation, the BP was stabilized in the Paleozoic (Ganade et al., 2021; Neves, 2021). During the Mesozoic, the onset of the rifting and magmatism events took place and culminated with the separation between Brazil and West Africa during Early Cretaceous (Heine et al., 2013; Matos, 1992; Matos et al., 2021). The rifting event left a sedimentary fingerprint in the BP in the form of aborted intracontinental basins, which are intrinsically related to the crustal-scale shear zones, such as Jatobá, Tucano, Rio do Peixe, Araripe, Iguatu, Mirandiba and São José do Belmonte basins (**Fig. 1** and **Fig**. **2**). Recent investigations have assessed the importance of post-rift structural reactivation of those basins and the adjacent basement, as well as neotectonic activity, to the development of the South American margin in NE Brazil (Bezerra et al., 2011, 2020; Lima Neto et al., 2013; Vasconcelos et al., 2021).Nonetheless, the timing, thermal behavior and kinematics during the reactivations of the shear zones have been a matter of intense debate (Castro et al., 2008; Ganade et al., 2022; Miranda et al., 2020; Nogueira et al., 2015).

The thermal behavior of the BP as a whole during the Cenozoic is also part of that debate, and the studies addressing the cooling events have shown the complexity of the region, with few of them focusing on reactivation (e.g., Harman et al., 1998; Nóbrega et al., 2005). On the other hand, several of low-temperature thermochronometry studies have suggested a more eventful history during Meso–Cenozoic (Harman et al., 1998; Jelinek et al., 2014, 2020; Morais Neto et al., 2006, 2009) or multiple phases of regional uplift/exhumation and subsidence/burial (Japsen et al., 2012; Turner et al., 2008). Of note, $^{40}Ar/^{39}Ar$ ages of the K-feldspar from mylonites of the shear zones from BP are indistinguishable from K-feldspar ages of country rocks, revealing that if there was any reactivation, it occurred under the ^{40}Ar closure temperature (150–350 °C) (Morais Neto, 2009 and references therein).

Here we present a new apatite (AFT) and zircon (ZFT) fission-track and apatite (U-Th)/He (AHe) dataset of the Pernambuco and Cruzeiro do Nordeste shear zones, as well as the adjacent basement of the Jatobá basin, collected with the main interest in constraining cooling events and potential brittle offsets on basement structures. We use inverse thermal modeling to bracket the stages of cooling and potential exhumation for this region from the Paleozoic to present-day, indicating the likely mechanisms responsible for that. We also compare the thermal

evolution of the Jatobá rift flank and the syn-rift sediments to propose possible intervals of reactivations. Based on those models, we estimate the thickness of the sedimentary pile deposited upon the syn-rift unit of the Jatobá basin, and compare it with the available data for the Recôncavo-Tucano-Jatobá and Araripe basin. Lastly, we address topics on the timing of reactivations of the basement and of the interior and marginal basins of the Borborema Province, as well as on the paleogeographic reconstructions for the Borborema Province. In general, our newly obtained data jointly with previously published data, indicate a prolonged history of landscape development and reactivations. The tectonic inheritance of the Borborema Province played a central role in the Early Cretaceous rifting event that culminated with the West Gondwana breakup and the birth of the South and Equatorial Atlantic ocean.

2. Borborema Province

2.1 Geological setting

The development of the northeastern Brazilian margin during the Early Cretaceous continental extension resulted in three main rift branches (Matos, 1999; Matos et al., 2021): the Sergipe-Alagoas-Gabon, the Recôncavo-Tucano-Jatobá, and the Cariri-Potiguar. Only the Sergipe-Alagoas-Gabon rift system evolved to divergent margins. The other two aborted rift systems culminated in intracontinental basins, including Jatobá, Araripe, Rio do Peixe, and Iguatu (**Fig. 1**). These basins have a backbone in common: they record not only a Paleozoic history but also the Jurassic–Early Cretaceous rifting-related sedimentation, which culminated in the opening of the South Atlantic Ocean (Matos, 1992, 1999). The Borborema Province (BP) served as the basement for that rift system. Generally, Archean nuclei and Paleoproterozoic units, as well as Tonian (Cariris Velhos Orogeny) and Ediacaran rocks (Brasiliano/Pan African Orogeny) form the Precambrian basement of the BP (Brito Neves et al., 2000; Neves et al., 2000a). The basement has a remarkable structural inheritance, characterized by a continental-scale, strike-slip shear zone system, known as the Borborema shear zone system (**Fig. 1**) (Vauchez et al., 1995). Those shear zones had a strong influence on the formation of those intracontinental basins (Matos et al., 2021). The current fabric with major (> 500 km-long) E-W-striking shear zones (Pernambuco and Patos shear zones) connected to subsidiary (Cruzeiro do Nordeste and Congo shear zones; 100 to 200-km-long) NE-trending shear zones (**Fig. 1**) was developed during the Ediacaran–Cambrian West Gonwana assembly, by lateral scape tectonics (Ganade et al., 2021). The Patos and Pernambuco (PESZ) shear zones divide the BP into three main domains: Southern (below PESZ), Transversal (Central) and Northern (above Patos shear zone). Northwest of the Northern Domain, the Senador Pompeu shear zone, in the east, and the Transbrasiliano Lineament, in the west, bound the Ceará Central Domain (**Fig. 1**). The PESZ is divided in two distinct, nonconnected segments: the high-temperature West Pernambuco shear zone (WPESZ) and the narrow East Pernambuco shear zone (EPESZ) (**Fig. 2**) (Neves & Mariano, 1999; Vauchez & Egydio-Silva, 1992). There is a discussion on the correlation between the PESZ and its African counterpart. Moulin et al. (2010) correlated the PESZ with the Sanaga lineament whereas other authors correlated it with the Adamawa shear zone (Caxito et al., 2020 and references therein). For the purpose of this study, we broadly refer to the counterpart as the Central African shear zone (Dorbath et al., 1986).

The study area (**Fig. 2**) comprises the Pernambuco and Cruzeiro do Nordeste shear zones, their Precambrian crystalline basement and the adjacent Jatobá basin (**Fig. 3**). Collected samples are detailed in **Table 1**. Rhyacian granitic mylonites related to the Floresta-Airi Suite composes the Paleoproterozoic units within the WPESZ. Additionally, migmatites of the Belém do São Francisco Complex and meta-sedimentary rocks from the Lagoas das Contendas Complex make

up the Tonian units, related to the Cariris Velhos Orogeny (Brito Neves et al., 2000; Santos et al., 2021). Finally, granitoids and mylonites from Bendó Granitoid, Vila Moderna, Itaporanga and Chorrochó Suites are the other magmatic units that are related to the Brasiliano/Pan African Orogeny (Brito Neves et al., 2000). The Jatobá basin (**Fig. 3**) is deposited over the Pernambuco-Alagoas massif (Brito Neves et al., 1982) and contains Silurian–Devonian continental sedimentary sequences (Tacaratu and Inajá formations) deposited in a nonconformity and occurring mainly on the eastern and southern flexural margin of the basin, which are interpreted as a syneclise phase (Costa et al., 2007). Late Jurassic units, namely Aliança and Sergi formations, are interpreted as the pre-rift stage, whereas Early Cretaceous units (Candeias Formation, Ilhas Group, Salvador and São Sebastião formations) are interpreted as the syn-rift stage of the basin (Costa et al., 2007). Aptian–Cenomanian post-rift sequences make up the stratigraphic scenario of this basin, containing the fluvial-dominated Marizal Fm., the marine sediments of the Santana Group, and the Exu Fm. (Costa et al., 2007; Neumann & Rocha, 2014). In addition to that, the fault border of the Jatobá basin is controlled by the SW-NE Ibimirim fault (**Fig. 2**), that is a result of the reactivation of the major ENE-trending, Cruzeiro do Nordeste shear zone at ca. 127-134 Ma and at ca. 162 Ma, revealed by U-Pb dating in carbonate (Ganade et al., 2022; Miranda et al., 2020).
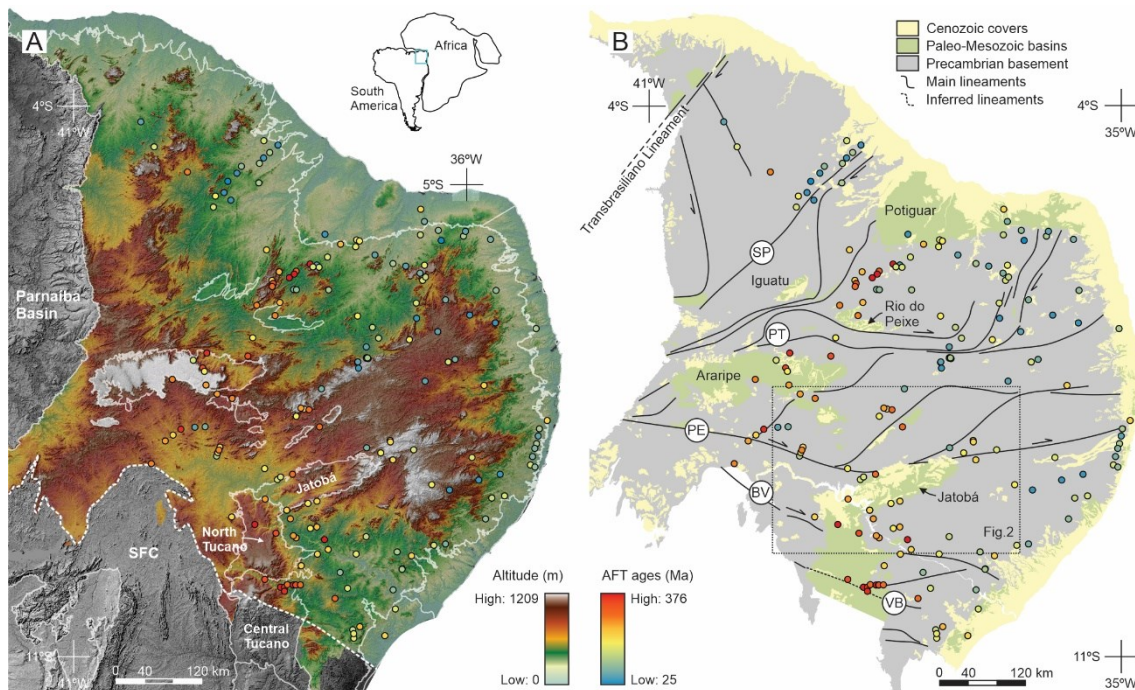
Fig. 1. A) Digital Elevation Model of the Borborema Province with compiled and new apatite fission-track samples. In white are the contours of the basins. SFC: São Francisco Craton. The white dashed line is the inferred contour of the São Francisco Craton based on Heilbron et al., (2017). B) Structural and geologic framework of the Borborema Province, based on Santos et al. (2021) and on airborne gamma-ray spectrometry. Main shear zones are: (SP) Senador Pompeu, (PT) Patos, (PE) Pernambuco, (BV) Boa Vista and (VB) Vaza Barris transfer zone.
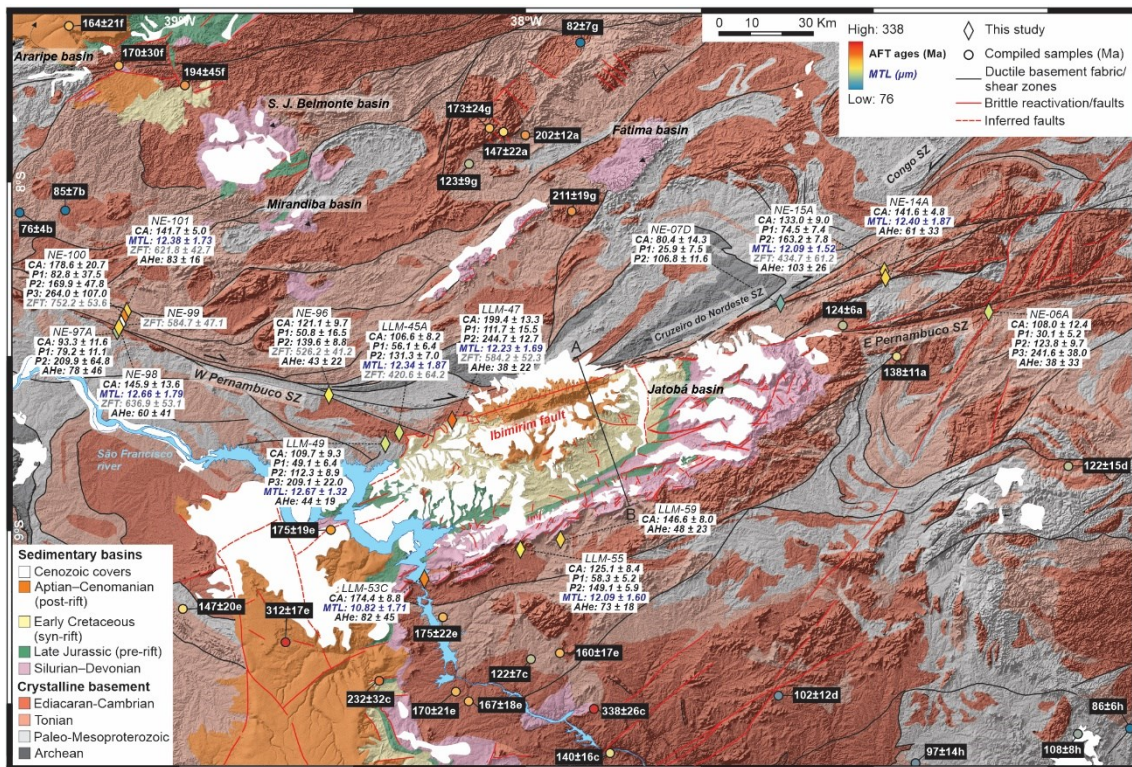
Fig. 2. Digital Elevation Model (ALOS PALSAR) with simplified geological units of the study area, based on Santos et al. (2021) and on airborne gamma-ray spectrometry. CA is the central age and the standard error of the apatite fission-track analyses.P1, P2 and P3 are the different individual populations of each sample (see the text for reference). MTL is the mean track length and the standard deviation in µm. ZFT are the central ages and the standard error of the zircon fission-track analyses in Ma. AHe is the mean age and the standard deviation of the apatite (U-Th)/He results. Letters in the compiled samples are: (a) Galindo & Oliveira (2006), (b) Harman et al., (1998), (c) Japsen et al., (2012), (d) Jelinek et al., (2014), (e) Jelinek et al., (2020), (f) Morais Neto et al., (2006), (g) Morais Neto et al., (2009), (h) Turner et al., (2008). A-B cross-section is presented in the Fig. 3. Details of compiled samples are in the supplementary material.
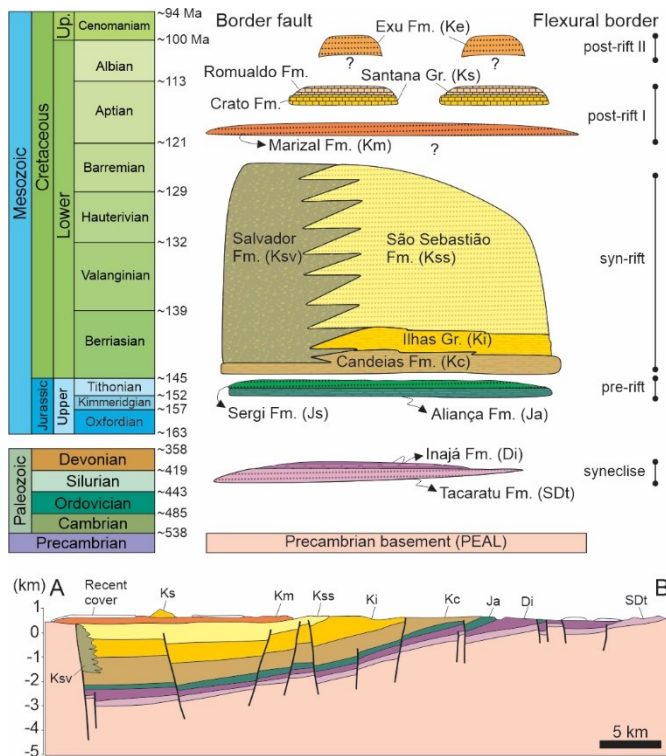
Fig. 3. Stratigraphic column of the Jatobá basin adapted from Costa et al. (2007), Neumann & Rocha (2014) and Rocha & Leite (1999). Below is the cross-section A-B (line presented in the Fig. 2). The acronyms of each unit is specified in parentheses in the column. The predominance of sandstones (dots), shales (dashes), conglomerates (circles) and limestones (bricks) are indicated in the units, as well as the depositional ages (in Ma).

2.2 Cooling history and thermal events

The high-temperature orogenic history of amalgamation of West Gondwana ceased at ca. 610–525 Ma in the Borborema Province (BP) (Cioffi et al., 2021; Ganade et al., 2021). ^{40}Ar/^{39}Ar data permit to assess the temperature history during the end of Neoproterozoic until the end of Paleozoic, as well as thermal events and intrusions that occurred at the BP during the Meso-Cenozoic. A comprehensive ^{40}Ar/^{39}Ar compilation with types of analyzed rocks and materials is presented in **Fig. 4**. The details of the compilation are presented in the supplementary material. ^{40}Ar/^{39}Ar cooling ages range from ca. 575–560 Ma for amphibole (closure temperature estimated at 550–450 °C), ca. 580–450 Ma for biotite (400–300 °C), ca. 550–500 Ma for muscovite (350–250 °C) and ca. 520–390 Ma for K-feldspar (350–150 °C) (Morais Neto, 2009 and references therein). Collectively, the available ^{40}Ar/^{39}Ar data reveal a widespread cooling of the basement rocks after the Brasiliano/Pan African Orogeny, implying that after peak metamorphism (~500–600 °C at ca. 580–525 Ma in the Seridó Belt; Cioffi et al., 2021), the basement rocks cooled to temperatures of ~350–250 °C by the Cambrian (ca. 540–500 Ma) (Morais Neto, 2009 and references therein).

Low-temperature thermochronology is being used in the northeast Brazil by several authors to address the cooling histories and the evolution of the landscape of the Borborema Province and adjacent areas (Harman et al., 1998; Japsen et al., 2012; Jelinek et al., 2014, 2020; Morais Neto et al., 2006, 2009; Turner et al., 2008). Summarizing all those studies, four stages of cooling and potential exhumation emerge: (1) almost all studies suggested accelerated cooling during the Early Cretaceous (ca. 130 to 90 Ma), which is generally related to denudation of the rifted-margin, driven by the continental breakup that culminated with the separation of South America and Africa; (2) a Late Cretaceous–Paleogene (ca. 80–60 Ma) fast cooling event

was reported by Harman et al. (1998) and Japsen et al. (2012). The former authors propose a reactivation of the Pernambuco shear zone during that time and relate that to changes in relative plate motions. The latter authors argue that uplift occurred in NE Brazil at that time and it was caused by lateral resistance to plate motion, since it is synchronous to a decrease in the spreading rate of the Mid-Atlantic Ridge and Andean orogenic cycles; (3) Japsen et al. (2012) and Turner et al. (2008) also proposed an accelerated cooling/uplift event during the Eocene (ca. 48–38 Ma); (4) another cooling event at ca. 20 Ma to present-day is reported by almost all authors using apatite fission-track in the BP.

Furthermore, the BP experienced a protracted history of thermal anomalies and magmatism. The first signs of distension within West Gondwana are related to the opening of the Central Atlantic and the emplacement of the Central Atlantic Magmatic Province (CAMP) at the Triassic-Jurassic boundary (Marzoli et al., 1999, 2018). Magmatic activity in the Parnaíba Basin (west of BP) is also linked to this event, and the Mosquito Formation is thought to represent occurrences of CAMP in the central and western part of the Parnaíba basin (De Min et al., 2003). Another important magmatic events are the Early Cretaceous Rio Ceará-Mirim, Canindé and Riacho do Cordeiro swarms (Pessano et al., 2021 and references therein) and the Sardinha magmatism of Parnaíba basin, dated at ca. 135 to 120 Ma, collectively known as the Equatorial Atlantic Magmatic Province (EQUAMP) (Hollanda et al., 2019). This event is related to mantle plume activity and extension that culminated with the Gondwana breakup and formation of the Equatorial Atlantic Ocean (Hollanda et al., 2019).

In spite of the limited occurrence of the Ipojuca Suite ("Cabo granite") in the Pernambuco-Paraíba basin (ca. 105–97 Ma, Nascimento et al., 2003) and the alkaline Cuó magmatism in the Potiguar basin (ca. 104–93 Ma, Souza et al., 2003) , the only expressive post-rift magmatic events present in the Borborema Province are the Macau and Mecejana units. The former is composed of alkaline/olivine basalts and diabase as well as microgabbros that occur in NE of Borborema Province, spanning from 52 to 7 Ma (Guimarães et al., 2020 and references therein). The latter occur as phonolitic necks in the region of Fortaleza, Ceará, with ca. 35 to 30 Ma (Guimarães et al., 2020; Knesel et al., 2011). Both of them are interpreted as resulting from an outflow of enriched asthenospheric mantle (Guimarães et al., 2020).
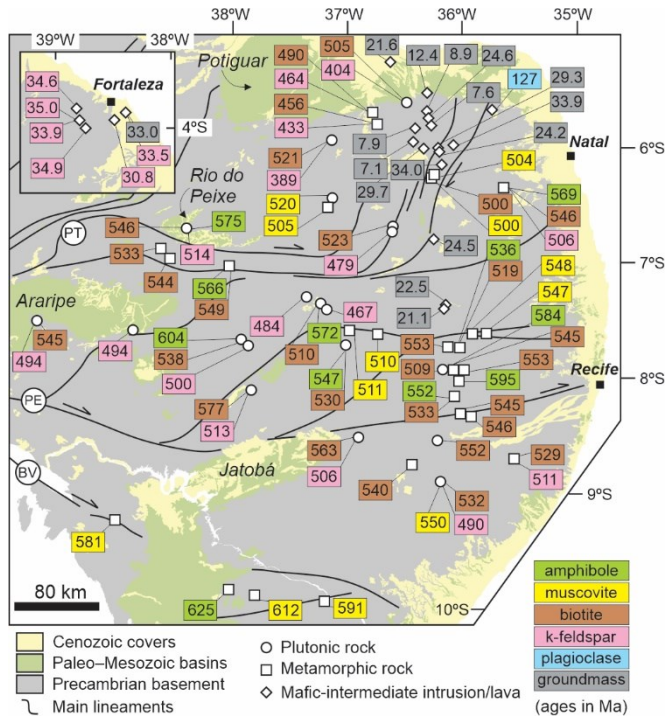
Fig. 4. Simplified structural and geologic framework of the Borborema Province, Northeast Brazil, based on Santos et al. (2021) and on airborne gamma-ray spectrometry, and the $^{40}Ar/^{39}Ar$ compilation with the rock types and analyzed materials. Details and references of the compiled data are presented in the supplementary material. PT: Patos Shear Zone. PE: Pernambuco Shear Zone. BV: Boa Vista Shear Zone.

Table 1. Sample location and lithology details. AFT is apatite fission-track, ZFT is zircon fission-track and AHe is (U-Th)/He in apatite. Details of ages and units are from Santos et al. (2021) and references therein. Hand specimen pictures are presented in the supplementary material.

Sample	Latitude	Longitude	Elevation	Unit	Lithology	Crystallisation/ Depositional ages	Methods
NE-06A	8°22'08.25"S	36°40'21.72"W	668 m	Itaporanga Suite	Ultramylonite	Ediacaran	AFT, AHe
NE-07D	8°20'36.87"S	37°16'15.74"W	589 m	Vila Moderna Suite	Granitic mylonite	Ediacaran	AFT
NE-14A	8°16'09.40"S	36°58'07.27"W	717 m	Vila Moderna Suite	Migmatite	Ediacaran	AFT, AHe
NE-15A	8°15'04.75"S	36°58'20.85"W	706 m	Vila Moderna Suite	Orthogneiss	Ediacaran	AFT, ZFT, AHe
NE-96	8°36'29.08"S	38°34'07.03"W	339 m	Floresta-Airi Suite	Mylonite	Rhyacian	AFT, ZFT, AHe
LLM-45A	8°42'57.20"S	38°22'00.28"W	340 m	Itaporanga Suite	Syenogranite	Ediacaran	AFT, ZFT
LLM-47	8°40'48.05"S	38°12'52.93"W	411 m	Salvador Fm.	Conglomerate	Lower Cretaceous	AFT, ZFT, AHe
LLM-49	8°44'53.61"S	38°24'22.14"W	335 m	Belém do São Francisco Complex	Diatexite	Tonian	AFT, AHe
LLM-53C	9°08'16.27"S	38°17'15.79"W	334 m	Chorrochó Suite	Syenogranite	Ediacaran	AFT, AHe
LLM-55	9°03'06.98"S	38°01'05.18"W	430 m	Chorrochó Suite	Metagranite	Ediacaran	AFT, AHe
LLM-59	9°01'27.17"S	37°54'10.52"W	359 m	Belém do São Francisco Complex	Granite	Tonian	AFT, AHe
NE-97A	8°25'15.94"S	39°10'28.64"W	413 m	Bendó Granitoid	Hydrothermally altered granite	Ediacaran	AFT, AHe
NE-98	8°24'13.08"S	39°09'56.52"W	428 m	Lagoa das Contendas Complex	Quartzite	Tonian	AFT, ZFT, AHe
NE-99	8°23'51.27"S	39°09'27.53"W	442 m	Lagoa das Contendas Complex	Quartzite	Tonian	ZFT
NE-100	8°22'46.39"S	39°09'14.54"W	435 m	Lagoa das Contendas Complex	Quartzite	Tonian	AFT, ZFT

NE-101	8°21'41.85"S	39°08'43.47"W	445 m	Lagoa das Contendas Complex	Quartzite	Tonian	AFT, ZFT, AHe

3. Sampling and analytical procedures

A total of sixteen samples were collected in the region of the Pernambuco shear zone and the Jatobá basin. Fifteen of them are from the crystalline basement of the Borborema Province and one is a conglomerate from the border fault of the Jatobá basin. Their details, location and lithologies are expressed in the **Table 1** and in the next sections. We divided the samples into groups referred to their location: (1) East of Jatobá, (2) North of Jatobá , (3) South of Jatobá and (4) West Pernambuco groups. Samples were analyzed by fission-track (AFT and/or ZFT) and (U-Th)/He (AHe) dating (**Table 1**), depending upon apatite and zircon yield. The details of these methods are presented in this section. In addition to that, appropriate samples were used for inverse modeling and all the details are presented in section "Thermal history inversion".

3.1 Fission-track thermochronology via LA-ICP-MS

Apatite fission-track (AFT) and zircon fission-track (ZFT) thermochronology stems from the spontaneous fission decay of the uranium isotope (^{238}U) and is applied to reconstruct the low-temperature thermal history through the partial annealing zone for a given crystal: ~60–110 °C for apatite (APAZ, Ketcham et al., 1999; Laslett et al., 1987) and ~230–310 °C for zircon (ZPAZ Tagami, 2005). To obtain both apatite and zircon concentrates, methods for heavy minerals separation were employed at the University of Campinas and the Geological Survey of Brazil (Rio de Janeiro), such as crushing, grinding, sieving (125-250-mesh portion), density separation in a vibrating table, magnetic separation, and heavy liquids. The AFT and ZFT analyses were carried out at ChronusCamp Research - Thermochronology Laboratory, LTD in Itapira/Brazil. Apatite grains were picked and mounted in epoxy resin, ground and polished to expose the internal surface of the grains, and the resulting mounts were etched in 5M HNO_3 for 20 s at 20 °C to reveal the fission tracks (Carlson et al., 1999). Zircon grains were mounted in Teflon Polyfluoroalkoxy (PFA), and then were polished and etched for 28 h at 220 °C in a KOH:NaOH (1:1) eutectic mixture to expose the fission tracks .The fission tracks were imaged and counted using a full automated Leica DM6M microscope with a nominal magnification of 1500x (analyst: Cleber Soares). Dpar and confined track lengths (only for AFT) were also measured. The uranium content was obtained by LA-ICP-MS through a New Wave UP213 laser connected to an Agilent 7800 ICPMS. ^{238}U concentration was measured in apatites utilizing the $^{238}U/^{43}Ca$ ratio calibrated against a homogeneous Mud Tank (MT-7) reference apatite (6.9 ± 1% ppm; Soares et al., 2015), and for zircons the $^{238}U/^{96}Zr$ ratios were measured calibrated against the 91500 zircon standard (81.2 ± 1% ppm; Wiedenbeck et al., 1995). Age calculations were performed using the zeta approach for LA-ICP-MS (Donelick et al., 2005; Soares et al., 2014) with values obtained for the age standards Durango apatite (Dur-2) with an $^{40}Ar/^{39}Ar$ age of 31.44 ± 0.18 Ma (McDowell et al., 2005) and Fish Canyon Tuff zircon (FCT) with an $^{40}Ar/^{39}Ar$ age of 28.293 ± 0.004 Ma (in sanidine; Renne et al., 2010). For every twelve unknown laser spots, one spot on the U standard (MT-7 or 91500) and on the age standard (Dur-2 or FCT) were performed for accuracy and precision. Data reduction was carried out in an in-house Excel spreadsheet, and radial plots were calculated using IsoplotR (Vermeesch, 2018). On samples with single-grain ages presenting significant dispersion, it is possible to partially preserve multiple ages. In these cases, discrete statistical populations were calculated and defined as "peaks" using IsoplotR. All values and details of the AFT and ZFT results are presented in the supplementary material.

3.2 Apatite (U-Th)/He

The method is based on the alpha decay products from the radiometric decay chain of ^{238}U, ^{235}U, ^{232}Th, and minor ^{137}Sm, resulting in the accumulation of ^4He in the crystal lattice. The temperature interval of the (U-Th)/He system between total and no accumulation is called "partial retention zone", which is ~85–35 °C for apatite (Farley & Stockli, 2002). The analyses were carried out at ChronusCamp Research - Thermochronology Laboratory, LTD in Itapira/Brazil. Apatite grains were hand-picked according to the quality, shape and the lack of inclusion. After that, grains were placed into small Nb tubes for ^4He extraction. Samples were heated with a 50W diode laser to ~800–1100 °C for 5 to 10 minutes to extract the radiogenic ^4He. The ASI Alphachron He measurement line coupled with Balzers PrismaPlus QME 220 quadrupole mass spectrometer was used. The extraction was carried out at least two times with the aim of reaching the complete mineral degassing. After the ^4He extraction, apatite grains were placed in vials (1.5 ml), spiked with a ^{235}U-^{230}Th-^{145}Nd tracer in HNO_3 and baked in a lab oven at 80 °C for 2 hours. Once minerals were dissolved, they were diluted with 1 to 3 mL of doubly-deionized water, and taken to the Agilent 7800 ICPMS for analysis. Sample solutions, along with normal solutions and blanks, were analyzed for U, Th, and Sm contents. (U-Th)/He dates and all associated data were calculated on a custom spreadsheet using the methods described in Ketcham et al., (2011). Every batch of samples includes standards (29.57 ± 2.66 Ma and 31.72 ± 2.82 Ma obtained for the Durango apatite) of run sporadically throughout the process to monitor procedures and maintain consistency from run to run.

4. Results

4.1 Apatite fission-track

The results of fifteen AFT analyses are summarized in **Table** and **3**. The samples were grouped in relation to the study area: (1) East of Jatobá (NE-06A, NE-07D, NE-14A and NE-15A); (2) North of Jatobá (LLM-45A, LLM-47, LLM-49 and NE-96); (3) South of Jatobá (LLM-53C, LLM-55 and LLM-59); and (4) West Pernambuco (NE-97A, NE-98, NE-100 and NE-101) (**Fig. 2**).

4.1.1 East of Jatobá group (EJG)

The East of Jatobá group comprises the samples located within the East Pernambuco shear zone (NE-06A), in the Cruzeiro do Nordeste shear zone (NE-07D) and in the transitional shear zones between them both (NE-14A and NE-15A) (**Fig. 2**). Sample NE-07D yields the youngest central age of the whole dataset (80.4 ± 14.3 Ma), although care must be taken due to the reduced number of recovered apatite grains (n = 13). Sample NE-06A yields a central age of 108.0 ± 12.4 Ma with wide single-grain age dispersion. Sample NE-14A yields a central age of 141.6 ± 4.8 Ma, with a narrow single-grain age dispersion, and is the only sample of this group that passes the χ^2 test. Sample NE-15A presents a central age of 133.0 ± 9.0 Ma. Only samples NE-14A and NE-15A have sufficient confined tracks to be evaluated with confidence and yield mean track lengths (MTL) of 12.40 ± 1.87 μm (n = 75) and 12.09 ± 1.52 μm (n = 51), respectively. Dpar values of this group range from 2.0 ± 0.1 μm to 2.3 ± 0.3 μm.

4.1.2 North of Jatobá group (NJG)

The samples gathered in the North of Jatobá group are located in the area between the Jatobá basin and the West Pernambuco shear zone, close to the Ibimirim fault, in the border fault of the Jatobá basin (**Fig. 2**). The only sedimentary sample of our dataset is from the syn-rift stage of the Jatobá basin (conglomerate of Salvador Fm.) with estimated deposition at ca. 145–125 Ma (Costa et al., 2007; Horn & Morais, 2016). The sample yields the oldest central age of

the whole dataset, 199.4 ± 13.3 Ma, and a MTL value of 12.23 ± 1.69 μm (n = 44). The other three samples of this group display overlapping ages within uncertainties. Sample LLM-45A yields a central age of 106.6 ± 8.2 Ma, while samples LLM-49 and NE-96 result in a central age of 109.7 ± 9.3 Ma and 121.1 ± 9.7 Ma, respectively. For these three samples, the statistical age population defined as Peak 1 is similar within uncertainty as well, ranging from 49.1 ± 6.4 and 56.1 ± 6.4 (14% to 24% of the analyzed grains). MTL values for samples LLM-45A and LLM-49 are 12.34 ± 1.87 μm and 12.67 ± 1.32 μm, respectively. Dpar values of this group range from 2.1 ± 0.1 μm to 2.6 ± 0.5 μm. None of them passes the χ^2 test.

4.1.3   South of Jatobá group (SJG)

The South of Jatobá group comprises the samples from the crystalline basement to the south of the flexural margin of the Jatobá basin (**Fig. 2**). Sample LLM-53C yields a central age of 174.4 ± 8.8 Ma. The MTL value of this sample is 10.82 ± 1.71 μm (n = 25) but caution must be taken with modeling assumptions due to the reduced number of measured confined tracks. Sample LLM-55 yields a central age of 125.1 ± 8.4, with a narrow single-grain age dispersion and a statistical population (Peak 1) of 58.3 ± 5.2 Ma (18%). The MTL value of this sample is 12.09 ± 1.60 μm (n = 38). Sample LLM-59 yields a central age of 144.2 ± 9.3 Ma and passes the χ^2 test. Dpar values of all samples are quite homogeneous, yielding values of 2.1 ± 0.1 μm.

4.1.4   West of Pernambuco group (WPG)

The four samples of this group are located in the West Pernambuco shear zone, within a 7.5 km-long section perpendicular to the shear zone (**Fig. 2**). This section was carried out to assess possible reactivations and the cooling history of this portion of Pernambuco Shear Zone. The northernmost sample NE-101 yields a central age of 141.7 ± 5.0 Ma, with low dispersion of the single-grain ages. Sample NE-100 displays a central age of 178.6 ± 20.7 Ma with 12% of the grains yielding a statistical population (Peak 1) of 82.8 ± 37.5 Ma. Sample NE-98 presents a central age of 145.9 ± 13.6 Ma. To the south of the Pernambuco Shear Zone, sample NE-97A (hydrothermally altered granite) yields a central age of 93.3 ± 11.6 Ma, which is the youngest age of this section, and passes the χ^2 test along with sample NE-100. The MTL values of the samples NE-101 and NE-98 are 12.38 ± 1.73 μm and 12.66 ± 1.79 μm, respectively. Dpar values of this group show a wide range from 2.1 ± 0.1 μm to 3.0 ± 0.4 μm.

Table 2. AFT results of this study divided by groups. n is the number of analyzed grains. Ns is the total number of counted spontaneous fission tracks. ρ_s is the average surface density of spontaneous fission tracks (in 10^5 tracks/cm^2). ^{238}U is the average concentration of ^{238}U (in ppm) measured by LA-ICP-MS calculated in relation to MT-7 (Soares et al., 2015). P. Age is the pooled age in Ma. C. Age is the central age in Ma. P_1, P_2, and P_3 are the statistical populations derived in the IsoplotR (Vermeesch, 2018) (in Ma), with each subsequent fraction of the sample (in %). All ages are reported with 1 sigma uncertainty. Disp is the percentage of single-grain age dispersion. $P(X^2)$ is the chi-squared probability test that dated single-grains belong to the same statistical population (samples fails the test if values are < 0.05).

Sample	n	Ns	ρ_s (x10^5)	^{238}U (ppm)	P. Age (Ma)	C. Age (Ma)	P_1 (Ma)	P_1 (%)	P_2 (Ma)	P_2 (%)	P_3 (Ma)	P_3 (%)	Disp (%)	$P(X^2)$
NE-06A	39	643	1.18	19.3	104.1 ± 5.0	108.0 ± 12.4	30.1 ± 5.2	18	123.8 ± 9.7	65	241.6 ± 38.0	17	63.7	0.00
NE-07D	13	116	0.99	25.6	69.5 ± 6.7	80.4 ± 14.3	25.9 ± 7.5	18	106.8 ± 11.6	82	X	X	51.7	0.00
NE-14A	39	1567	2.54	32.7	138.2 ± 5.2	141.6 ± 4.8	141.4 ± 4.3	100	X	X	X	X	9.6	0.08
NE-15A	40	946	1.48	21.2	124.8 ± 5.3	133.0 ± 9.0	74.5 ± 7.4	26	163.2 ± 7.8	74	X	X	35.7	0.00
NE-96	40	470	0.75	12.2	112.4 ± 6.1	121.1 ± 9.7	50.8 ± 16.5	14	139.6 ± 8.8	86	X	X	38.2	0.00
LLM-45A	36	722	1.25	22.7	98.9 ± 4.6	106.6 ± 8.2	56.1 ± 6.4	24	131.3 ± 7.0	76	X	X	38.5	0.00
LLM-47	32	662	1.46	13.2	194.7 ± 9.3	199.4 ± 13.3	108.2 ± 15.9	20	228.9 ± 12.3	80	X	X	25.7	0.00
LLM-49	39	856	1.37	24.7	99.5 ± 4.4	109.7 ± 9.3	49.1 ± 6.4	19	112.3 ± 8.9	59	209.1 ± 22.0	22	46.6	0.00
LLM-53C	40	806	1.26	13.5	166.6 ± 7.4	174.4 ± 8.8	174.4 ± 6.9	100	X	X	X	X	18.1	0.02
LLM-55	39	1087	1.74	26.8	116.3 ± 4.8	125.1 ± 8.4	58.3 ± 5.2	18	149.1 ± 5.9	82	X	X	35.5	0.00
LLM-59	39	374	0.60	7.82	137.3 ± 8.0	144.2 ± 9.3	146.6 ± 8.0	100	X	X	X	X	21.0	0.11

NE-97A	30	105	0.22	5.08	81.9 ± 8.3	93.3 ± 11.6	79.2 ± 11.1	84	209.9 ± 64.8	16	X	X	35.1	0.09
NE-98	33	306	0.59	8.17	128.8 ± 8.2	145.9 ± 13.6	145.9 ± 13.6	100	X	X	X	X	55.1	0
NE-100	26	142	0.34	4.05	150.8 ± 13.3	178.6 ± 20.7	82.8 ± 37.5	12	169.9 ± 47.8	57	264.0 ± 107.0	31	60.3	0.06
NE-101	38	1933	3.27	41.8	140.9 ± 5.0	141.6 ± 5.0	142.7 ± 4.1	100	X	X	X	X	12.4	0.02

Table 3. AFT results of the study samples divided by groups. nl is the number of measured confined tracks. Mean track length (MTL) is the average length of the confined tracks in µm and SD is the standard deviation. Dpar is the average etch-pit diameter in µm and SD is the standard deviation.

Sample	nl	MTL (µm)	SD (µm)	Dpar (µm)	SD (µm)
NE-06A	-	-	-	2.0	0.1
NE-07D	-	-	-	2.3	0.3
NE-14A	75	12.40	1.87	2.2	0.1
NE-15A	51	12.09	1.52	2.1	0.1
NE-96	-	-	-	2.1	0.1
LLM-45A	34	12.34	1.87	2.1	0.2
LLM-47	44	12.23	1.69	2.6	0.5
LLM-49	65	12.67	1.32	2.3	0.2
LLM-53C	25	10.82	1.71	2.1	0.1
LLM-55	38	12.09	1.60	2.1	0.1
LLM-59	-	-	-	2.1	0.1
NE-97A	-	-	-	2.3	0.3
NE-98	35	12.66	1.79	3.0	0.4
NE-100	-	-	-	2.6	0.5
NE-101	83	12.38	1.73	2.1	0.1

4.2 Zircon fission-track

A total of eight samples were analyzed by the zircon fission-track (ZFT) method. From the fifteen samples analyzed by the AFT method, seven of them also yielded zircon grains to be analyzed by ZFT. The other one, sample NE-99, is from the section perpendicular to the West Pernambuco shear zone. All the results and details about the samples are summarized in **Table 4** and their locations can be seen in **Fig. 2**. The radial plots are presented in the supplementary material.

All ZFT results are older than the AFT results. Sample NE-15 is an Ediacaran orthogneiss from the Vila Moderna Suite and yielded a central age of 434.7 ± 61.2 Ma. Two samples of the North Jatobá group display ZFT central ages of 420.6 ± 64.2 Ma (LLM-45A) and 526.2 ± 41.2 Ma (NE-96). From the perpendicular section across the West Pernambuco shear zone (WPG), four quartzites from the Tonian Lagoa das Contendas Complex yield ZFT central ages varying from 584.7 ± 47.1 Ma to 752.2 ± 53.6 Ma. The conglomerate of the Salvador Formation (LLM-47), from the Jatobá basin, results in a ZFT central age of 584.2 ± 52.3 Ma. None of the samples passes the χ^2 test, except for the NE-101 and LLM-47.

Table 4. ZFT results of this study. n is the number of analyzed grains. Ns is the total number of counted spontaneous fission tracks. ρ_s is the average surface density of spontaneous fission tracks (in 10^6 tracks/cm^2). ^{238}U is the average concentration of ^{238}U (in ppm) measured by LA-ICP-MS calculated in relation to zircon standard 91500 (Wiedenbeck et al., 1995). P. Age is the pooled age in Ma. C. Age is the central age in Ma. P_1 and P_2 are the statistical populations derived in the IsoplotR (Vermeesch, 2018) (in Ma), with each subsequent fraction of the sample (in %). All ages are reported with 1 sigma uncertainty. Disp is the percentage of single-grain age dispersion. P(X^2) is the chi-squared probability test that dated single-grains belong to the same statistical population (samples fails the test if values are < 0.05).

Sample	n	Ns	ρ_s (×10^6)	^{238}U (ppm)	P. Age (Ma)	C. Age (Ma)	P_1 (Ma)	P_1 (%)	P_2 (Ma)	P_2 (%)	Disp (%)	P(X^2)
NE-15A	12	710	2.50	138.8	433.6 ± 20.2	434.7 ± 61.2	198.7 ± 34.1	25	555.5 ± 46.0	75	41.5	0

NE-96	25	879	2.99	125.3	502.8 ± 21.9	526.2 ± 41.2	334.6 ± 69.2	27	620.8 ± 54.2	73	28.0	0
NE-98	25	1311	2.41	85.30	588.9 ± 23.0	636.9 ± 53.1	638.2 ± 32.4	100	X	X	32.8	0
NE-99	25	809	2.47	108.5	497.3 ± 22.2	584.7 ± 47.1	586.0 ± 32.4	100	X	X	29.0	0
NE-100	25	1278	2.72	79.10	694.6 ± 27.3	752.2 ± 53.6	614.1 ± 54.7	64	1081.0 ± 142.0	36	24.5	0
NE-101	20	632	3.06	115.6	605.9 ± 29.3	621.8 ± 42.7	623.8 ± 38.0	100	X	X	14.0	0.18
LLM-47	13	351	2.70	105.4	570.3 ± 34.3	584.2 ± 52.3	588.5 ± 46.0	100	X	X	15.6	0.11
LLM-45A	9	181	2.01	116.1	390.4 ± 38.0	420.6 ± 64.2	427.1 ± 43.3	100	X	X	34.0	0.01

4.3 Apatite (U-Th)/He

The results and details of the single-grain (U-Th)/He apatite ages are presented in the **Table 5**. They do not show any correlation with altitude. The mean ages from East of Jatobá group samples vary from 38 ± 33 to 103 ± 26 Ma. North of Jatobá group samples range from 38 ± 22 to 44± 19 Ma and display collectively the youngest samples of our dataset. South of Jatobá group samples span from 48 ± 23 to 82 ± 45 Ma whereas the West of Pernambuco group samples vary from 60 ± 41 to 83 ± 16 Ma.

Single-grain analyses of our dataset present age variation exceeding the analytical uncertainty and this feature has already been extensively documented in the literature (Green & Duddy, 2018 and references therein). Some of the factors that can contribute to this variation are assessed herein. The presence of unrecognized U-Th rich inclusions or fluid inclusions and U and Th zonation in apatite grains (Farley, 2002; Lippolt et al., 1994) can influence this variation, but careful hand picking of well-formed, inclusion-free apatite diminishes the influence of the former, and apatite fission-tracks counting on the same samples did not show significant zonation, minimizing the influence of the latter. Another factor is He implantation from U-Th rich minerals (Spiegel et al., 2009). By analyzing the graph of eU *vs.* He content (**Fig. 5a**), it is possible to notice a positive correlation between them, but with some intra-sample outliers, which can be a feature of "parentless" He.

Increase in He retention by radiation damage produced by α-recoil is another feature recognized by several authors that may explain anomalously old AHe ages, and the difference of eU values (used as a proxy for the accumulation of radiation damage and annealing) in single-grain apatites could explain the age variation in a sample (Fitzgerald et al., 2006; Flowers et al., 2009; Gautheron et al., 2009; Shuster et al., 2006). Apatite grain size can also influence the age variation (Farley, 2000). We provide plots of eU vs AHe ages (**Fig. 5b**) and grain size vs AHe ages (**Fig. 5c**). Apparently there is no correlation in both plots, suggesting that these effects may not account for our dataset variability. Conversely, some authors demonstrated that terranes that cooled under relatively slow rates (< 3 °C/m.y.) and/or resided for a long time in the (U-Th)/He partial retention zone (~85–35 °C; Farley & Stockli, 2002) usually present greater variation in He ages than terranes that experienced a more rapid cooling (Fitzgerald et al., 2006). This variation can inverse fission-track ages to be younger than the He ages in some cases (e.g., Flowers & Kelley, 2011), which is not our case for almost all samples (**Fig. 5d**). Therefore, for our dataset the slow cooling rates (discussed in the next sections) and protracted residence in the partial retention zone could have influenced the behavior of He retentivity and the age variation.
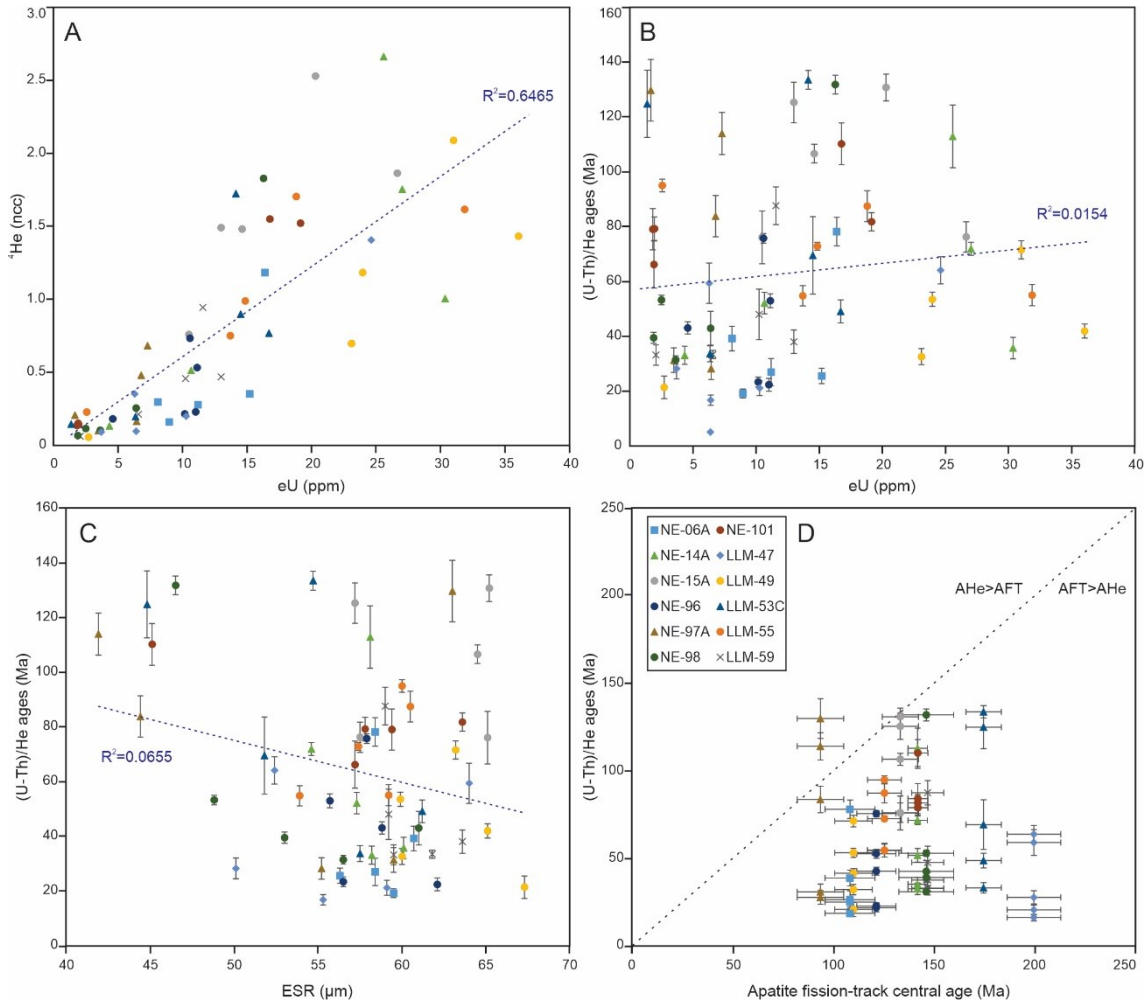
Fig. 5. Diagrams showing the variation of ages, as well as chemical and physical parameters of the apatite (U-Th)/He dataset. A) eU ([U]+0.235*[Th]) *vs.* ⁴He content. B) eU *vs.* corrected (U-Th)/He ages. C) equivalent spherical radius (ESR) *vs.* corrected (U-Th)/He ages. D) AFT central ages *vs.* corrected (U-Th)/He ages.

Table 5. Apatite single-grain (U-Th)/He results of this study. The amount of ⁴He is given in nano-cubic-cm in standard temperature and pressure. eU: the effective uranium content given by eU = [U]+0.235*[Th]. F_T: alpha-ejection correction (according to Farley et al., 1996; Hourigan et al., 2005). ESR: equivalent spherical radius. Complete information about the grains is presented in the supplementary material.

Sample	⁴He (ncc)	±1σ (ncc)	²³⁸U (ppm)	±1σ (ppm)	²³²Th (ppm)	±1σ (ppm)	Th/U	Sm (ppm)	±1σ (ppm)	eU (ppm)	Uncorr. age (Ma)	±1σ (Ma)	F_T	Age$_{corr}$ (Ma)	±1σ (Ma)	ESR (µm)	Mean age ± SD (Ma)
NE-06A-a1	1.184	0.037	13.05	0.13	14.41	0.14	1.10	65.47	1.19	16.40	58.96	3.78	0.754	78.20	5.21	58.4	38 ± 24
NE-06A-a2	0.160	0.006	6.97	0.07	8.60	0.09	1.23	61.64	1.22	8.97	14.53	1.08	0.758	19.17	1.62	59.5	
NE-06A-a3	0.296	0.016	6.43	0.06	7.17	0.07	1.12	45.02	0.86	8.09	29.91	3.26	0.763	39.20	4.47	60.7	
NE-06A-a4	0.352	0.018	13.03	0.13	9.38	0.09	0.72	17.14	0.51	15.21	19.05	1.94	0.745	25.57	2.80	56.3	
NE-06A-a5	0.278	0.025	9.17	0.09	8.74	0.09	0.95	46.93	0.89	11.20	20.36	3.62	0.756	26.93	4.99	58.4	
NE-14A-a1	0.513	0.001	8.48	0.38	9.42	0.94	1.11	81.70	25.88	10.67	39.21	2.79	0.752	52.14	3.91	57.3	61 ± 33
NE-14A-a2	1.006	0.052	26.85	0.27	15.10	0.15	0.56	31.64	0.66	30.36	27.27	2.83	0.763	35.74	3.91	60.1	
NE-14A-a3	2.663	0.131	22.96	0.23	11.33	0.11	0.49	30.64	0.58	25.58	85.25	8.46	0.755	112.91	11.41	58.1	
NE-14A-a4	1.754	0.021	24.97	0.25	8.90	0.09	0.36	15.32	0.48	27.03	53.37	1.61	0.742	71.93	2.37	54.6	
NE-14A-a5	0.132	0.006	3.70	0.00	2.78	0.00	0.75	2.77	0.15	4.35	25.02	2.34	0.756	33.10	3.30	58.2	
NE-15A-a1	2.529	0.041	16.63	0.17	15.84	0.16	0.95	32.43	0.71	20.30	101.72	3.64	0.778	130.75	4.88	65.2	103 ± 26
NE-15A-a2	1.491	0.041	11.50	0.11	6.45	0.06	0.56	19.57	0.46	13.00	93.85	5.38	0.749	125.30	7.38	57.2	
NE-15A-a3	1.481	0.018	12.97	0.13	7.10	0.07	0.55	32.84	0.65	14.61	82.94	2.48	0.778	106.61	3.39	64.5	
NE-15A-a4	0.759	0.047	9.30	0.09	5.14	0.05	0.55	18.94	0.49	10.49	59.36	7.35	0.780	76.10	9.62	65.1	
NE-15A-a5	1.864	0.064	22.50	0.22	17.89	0.18	0.80	40.41	0.90	26.65	57.35	4.01	0.752	76.26	5.53	57.5	
NE-96-1a	0.215	0.007	9.75	0.10	1.84	0.02	0.19	8.62	0.32	10.17	17.48	1.18	0.748	23.37	1.78	56.5	43 ± 22
NE-96-a2	0.533	0.011	10.66	0.11	2.07	0.02	0.19	7.53	0.24	11.14	39.42	1.75	0.744	52.98	2.55	55.7	

NE-96-a3	0.734	0.003	10.18	0.10	1.74	0.02	0.17	13.83	0.41	10.59	56.96	1.18	0.752	75.74	1.77	57.9	
NE-96-a4	0.182	0.004	4.25	0.04	1.49	0.01	0.35	3.32	0.25	4.60	32.56	1.55	0.756	43.07	2.25	58.8	
NE-96-a5	0.230	0.011	10.57	0.11	1.96	0.02	0.19	22.20	0.58	11.02	17.18	1.65	0.768	22.37	2.35	62.1	
LLM-47-a1	1.406	0.051	19.42	0.19	22.43	0.22	1.16	15.12	0.42	24.63	46.85	3.49	0.731	64.09	4.97	52.4	38 ± 22
LLM-47-a2	0.091	0.006	3.32	0.03	1.66	0.02	0.50	1.90	0.13	3.70	20.30	2.58	0.719	28.23	3.79	50.1	
LLM-47-a3	0.097	0.005	5.30	0.05	4.77	0.05	0.90	3.91	0.20	6.41	12.46	1.25	0.744	16.75	1.88	55.3	
LLM-47-a4	0.200	0.012	8.85	0.09	6.20	0.06	0.70	7.78	0.29	10.29	16.05	1.92	0.759	21.15	2.73	59.1	
LLM-47-a5	0.352	0.021	5.38	0.05	3.94	0.04	0.73	3.28	0.18	6.30	45.96	5.52	0.774	59.38	7.33	64.0	
LLM-49-a1	1.184	0.024	22.11	0.22	7.98	0.08	0.36	44.67	0.85	23.97	40.62	1.80	0.759	53.52	2.57	59.9	44 ± 19
LLM-49-a2	0.697	0.028	21.39	0.21	7.38	0.07	0.35	50.81	1.00	23.10	24.84	2.07	0.762	32.60	2.92	60.0	
LLM-49-a3	0.056	0.005	2.40	0.02	1.42	0.01	0.59	17.67	0.09	2.73	16.83	3.07	0.787	21.39	4.10	67.3	
LLM-49-a4	1.433	0.039	32.91	0.33	13.49	0.13	0.41	65.27	1.18	36.04	32.71	1.87	0.780	41.94	2.60	65.1	
LLM-49-a5	2.089	0.041	29.02	0.29	8.56	0.09	0.29	34.70	0.77	31.01	55.38	2.40	0.774	71.55	3.30	63.2	
LLM-53C-a1	0.197	0.008	3.84	0.04	10.84	0.11	2.83	7.67	0.27	6.35	25.32	2.05	0.752	33.67	2.93	57.5	82 ± 45
LLM-53C-a2	1.724	0.020	6.71	0.05	32.01	0.32	4.77	79.65	25.36	14.14	98.54	2.39	0.738	133.52	3.44	54.7	
LLM-53C-a3	0.146	0.007	1.00	0.01	1.62	0.02	1.62	16.48	0.12	1.38	85.38	8.23	0.684	124.82	12.23	44.8	
LLM-53C-a4	0.768	0.031	9.87	0.01	29.47	0.29	2.99	17.85	0.46	16.71	37.57	3.03	0.765	49.11	4.16	61.2	
LLM-53C-a5	0.899	0.090	8.31	0.08	26.73	0.27	3.22	23.00	0.61	14.51	50.56	10.11	0.727	69.55	14.11	51.8	
LLM-55-a1	1.616	0.052	27.25	0.27	19.90	0.20	0.73	18.24	0.49	31.87	41.70	2.77	0.758	55.01	3.85	59.2	73 ± 18
LLM-55-a2	0.751	0.023	13.38	0.13	1.43	0.08	0.11	7.83	0.42	13.71	40.33	2.56	0.736	54.80	3.68	53.9	
LLM-55-a3	1.704	0.051	18.76	0.19	0.25	0.10	0.01	11.45	0.36	18.81	66.73	4.14	0.763	87.46	5.63	60.5	
LLM-55-a4	0.228	0.002	2.19	0.02	1.67	0.02	0.76	13.25	0.10	2.58	72.29	1.60	0.761	94.99	2.30	60.0	
LLM-55-a5	0.989	0.002	12.73	0.13	9.21	0.09	0.72	11.26	0.33	14.87	54.63	0.94	0.750	72.84	1.45	57.4	
LLM-59-a1	0.063	0.003	1.78	0.02	1.29	0.01	0.73	1.05	0.09	2.08	25.16	2.64	0.758	33.19	3.68	59.5	48 ± 23
LLM-59-a2	0.470	0.025	8.31	0.08	20.22	0.20	2.43	58.81	1.16	13.00	29.45	3.14	0.774	38.05	4.26	63.6	
LLM-59-a3	0.213	0.003	3.68	0.07	12.54	0.01	3.41	171.24	34.99	6.59	25.69	0.97	0.769	33.41	1.46	61.8	
LLM-59-a4	0.458	0.043	7.82	0.08	10.40	0.10	1.33	36.06	0.76	10.24	36.59	6.87	0.762	48.02	9.22	59.2	
LLM-59-a5	0.944	0.036	8.00	0.08	15.44	0.15	1.93	44.35	0.95	11.58	66.42	5.06	0.758	87.63	6.88	59.0	
NE-97A-a1	0.102	0.007	1.97	0.02	6.60	0.07	3.36	8.39	0.32	3.50	23.90	3.27	0.763	31.32	4.49	59.5	78 ± 46
NE-97A-a2	0.166	0.011	3.71	0.01	11.77	0.02	3.17	2.22	0.15	6.44	21.03	2.79	0.745	28.23	3.94	55.2	
NE-97A-a3	0.480	0.021	3.70	0.04	13.36	0.13	3.61	10.43	0.30	6.80	57.50	5.05	0.686	83.82	7.56	44.4	
NE-97A-a4	0.682	0.022	6.42	0.06	3.78	0.04	0.59	9.39	0.31	7.30	76.59	5.02	0.672	113.97	7.67	41.9	
NE-97A-a5	0.206	0.009	1.38	0.01	1.24	0.01	0.90	13.01	0.10	1.66	100.65	8.57	0.776	129.70	11.24	63.0	
NE-98-a1	1.828	0.019	10.25	0.10	25.99	0.26	2.53	22.44	3.50	16.28	91.47	2.23	0.694	131.80	3.41	46.5	60 ± 41
NE-98-a2	0.256	0.018	5.87	0.06	2.33	0.02	0.40	6.14	0.28	6.41	32.83	4.57	0.764	42.97	6.18	61.0	
NE-98-a3	0.067	0.002	1.37	0.01	2.23	0.02	1.62	15.98	0.10	1.89	28.82	1.35	0.730	39.48	2.05	53.0	
NE-98-a4	0.103	0.002	3.18	0.03	1.94	0.02	0.61	2.88	0.19	3.63	23.44	0.99	0.746	31.42	1.53	56.5	
NE-98-a5	0.115	0.001	2.22	0.02	1.26	0.01	0.57	3.47	0.19	2.51	37.72	1.09	0.708	53.28	1.74	48.8	
NE-101-a1	0.143	0.003	1.69	0.02	1.15	0.01	0.68	14.62	0.11	1.96	59.66	3.07	0.753	79.23	4.28	57.8	83 ± 16
NE-101-a2	0.136	0.001	1.51	0.09	1.38	0.01	0.91	21.30	0.50	1.83	60.09	5.58	0.760	79.07	7.54	59.4	
NE-101-a3	0.152	0.010	1.50	0.01	1.81	0.04	1.20	30.88	0.75	1.92	49.72	6.30	0.751	66.21	8.59	57.2	
NE-101-a4	1.550	0.050	16.30	0.16	2.05	0.02	0.13	32.65	0.66	16.77	75.83	5.10	0.688	110.22	7.61	45.1	
NE-101-a5	1.522	0.025	18.97	0.19	0.76	0.03	0.04	36.40	0.70	19.15	63.47	2.42	0.776	81.79	3.32	63.6	

5. Thermal history inversion

We performed thermal history inversion on eight basement samples and on a conglomerate of the border fault of the Jatobá basin, and the results are presented in **Fig. 6** and **Fig. 7**, respectively. All inverse modeling simulations were carried out using HeFTy software v. 2.0.0 (Ketcham, 2005). We used the annealing model of Ketcham et al. (2007) for the AFT simulations, and the RDAAM model when the AHe data were included (Flowers et al., 2009). The data input for the AFT are the single-grain age and average Dpar of the grain, as well as the confined track length, the angle with the c-axis and the Dpar for each track. For AHe data, grain size, U and Th content and the uncorrected age were added in the model. For each inverse simulation, 100,000 random thermal histories paths were generated and compared against the input data. At first, we have done simulations only using the AFT data, as that method has kinetic parameters that are more well-established, to see the general behavior of that sample. After

that, we added single-grain AHe dates one by one, and the simulations that returned acceptable time-temperature (t-T) paths were then validated and used for interpretations (e.g., Ketcham et al., 2018). Samples NE-15A, LLM-45A and NE-101 did not return acceptable t-T paths when adding any of the single-grain apatite data, thus only AFT data supported the inverse thermal modeling of those samples.

Another important step is to add geologic constraints to impose restrictions on possible thermal histories. The first t-T box used is the Neoproterozoic–Paleozoic high temperature constrained by both our new ZFT data and the compiled $^{40}Ar/^{39}Ar$ samples. Based on this, it is possible to infer that after the orogenic collapse of the Borborema Province during the Neoproterozoic, it attained temperatures of approximately 300–200 °C at ca. 460–500 Ma. For convenience, we set a t-T box between 160 and 200 °C, and 460 and 500 Ma (**Fig. 6**). The other t-T box can be constrained by the deposition of the Tacaratu Fm. This barren unit is composed of fluvial conglomeratic sandstones and it has been correlated to the Serra Grande Group of the Parnaíba basin and the Cariri Group of the Araripe basin, attributed to the Silurian–Devonian due to palynological studies (Carvalho et al., 2018 and references therein). The contact between the Tacaratu Fm. and the basement is either by faults or a nonconformity, and as this unit occurs in almost all interior basins of the Borborema Province (**Fig. 2**), it is possible to infer that the study area was already near the surface (20 ± 5 °C) during the Silurian–Devonian. Even though inverse modeling using AFT and/or AHe data do not constrain the t-T history before the maximum burial, which in our case is from the Devonian onwards, this part of the history should be included in the models as highlighted by Ketcham et al. (2018). This part can contribute short tracks to the overall track-length distribution, and it can also affect later He-diffusion behavior due to damage accumulation, resulting in better predictions of the actual AFT/AHe part of the history (Ketcham et al., 2018).

After the nonconformity of the Tacaratu Fm., we set a broad t-T box to constrain the possible paths for the maximum subsequent burial and cooling, as well as the present-day constraint (20 ± 5 °C). We certified that this broad box was not limiting the t-T constraint points. For the post-nonconformity period, a maximum heating and cooling rate of 10 °C/m.y. was set to prevent histories that are geologically meaningless for a relatively stable region such as the Borborema Province.
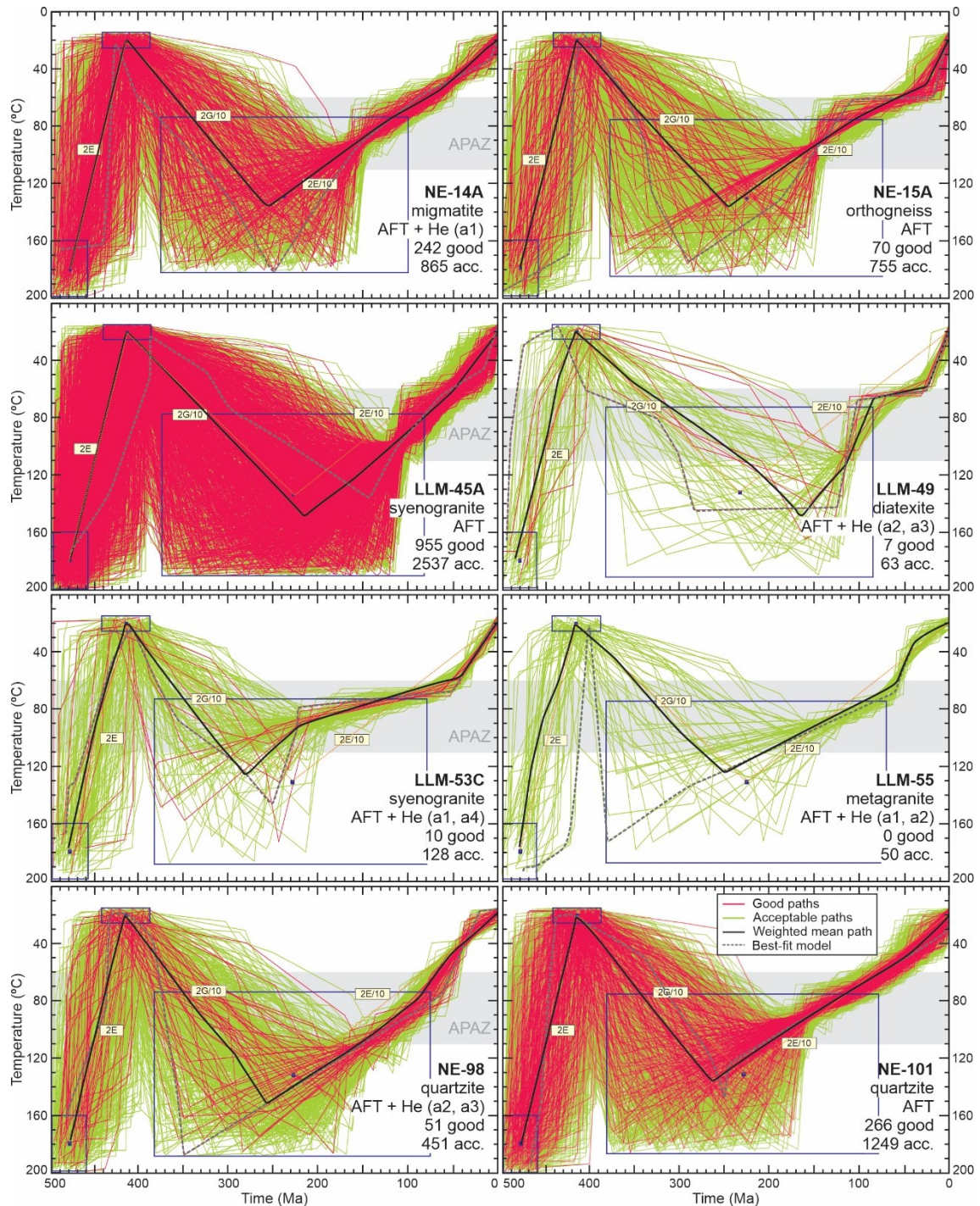
Fig. 6. Time-temperature models based on apatite fission track and (U–Th)/He data. For each sample, the best possible model is shown. When (U–Th)/He data are included, this is specified in parentheses (a#: aliquot numbers referring to Table 5). The blue outline boxes are the t-T constraint s that are explained in the text. The number of good (reddish) and acceptable (green) paths is given. Solid black paths are the weighted mean paths whereas dashed gray paths are the best-fit model. APAZ refers to the apatite partial annealing zone.

The geologic constraints for modeling the conglomerate from the Salvador Fm. (sample LLM-47) are different (**Fig. 7**). The first t-T box is a broad constraint to capture the AFT data of grains with old tracks that suffered partial reset and grains that did not, reflecting the source rocks . Without that constraint the HeFTy software do not return any possible model. The thermal history is only well-resolved from the deposition onwards, that is attributed to the rift

phase of the Jatobá basin, in the Berriasian–Barremian (ca. 145–125 Ma). After that, a broad t-T box was set and burial/cooling was limited to a rate of 10 °C/m.y.
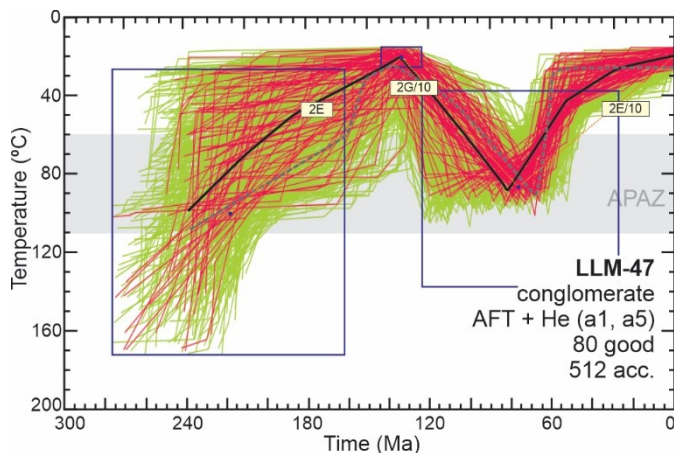
Fig. 7. Time-temperature model for sample LLM-47 (Salvador Fm., Jatobá basin). See Fig. 6 caption for details. Notice the difference in the timescale.

6. Discussion

6.1 Post-orogenic cooling during Paleozoic

The cooling history of the Borborema Province (BP) after the metamorphism peak at the transition from the Ediacaran to Paleozoic has been assessed by several authors using mainly ^{40}Ar/^{39}Ar ages of different minerals (Archanjo et al., 2021; Ávila et al., 2020; Corsini et al., 1998; Morais Neto, 2009; Neves et al., 2000b). Farther NW of the study area, Ávila et al. (2020) using ^{40}Ar/^{39}Ar plateau ages of amphibole and biotite from synkinematic plutons of the region of the Tauá shear zone, in the Ceará Central Domain, calculated cooling rates of 20 to 40 °C/m.y. during the interval of ca. 580 and 550 Ma. Conversely, the Patos shear zone presents slower cooling rates, denoting that the Borborema Province did not cool equally at the end of the Neoproterozoic. Archanjo et al. (2021) also using ^{40}Ar/^{39}Ar ages of biotite and amphibole from migmatites of the Patos shear zone, determined cooling rates of 12 to 17 °C/m.y. assuming a linear decrease after the metamorphic peak at ca. 565 Ma until ca. 535–550 Ma. Other authors found a milder cooling rate for the Patos shear zone in the connection with the Seridó belt. Using U-Pb zircon ages and ^{40}Ar/^{39}Ar ages of amphibole, biotite and muscovite, they defined a homogeneous cooling rate of 3-4 °C/m.y. between 580 and 500 Ma, followed by a rapid cooling suggested by concordant muscovite and biotite ^{40}Ar/^{39}Ar plateau ages around 500 Ma (Corsini et al., 1998).

A regional approach on the cooling of the BP was carried by Morais Neto (2009), who calculated cooling rates with both compiled (Araújo et al., 2005; Sial et al., 2008) and new ^{40}Ar/^{39}Ar samples from different regions of the BP. The author used amphibole-biotite pairs and calculated cooling rates between 4.5 and 9.5 °C/m.y. for the Northern Domain whereas the Transversal Domain showed values of 2.6 to 31.7 °C/m.y. Using the biotite-K-feldspar pair, cooling rates range from 0.4 to 2.9 °C/m.y. in the Northern Domain, 1.0 to 1.2 °C/m.y. in the Transversal Domain and 0.84 to 2 °C/m.y. in the Southern Domain. Lastly, the author applied the muscovite-biotite pair that revealed a cooling rate of 2.5 °C/m.y. for the Southern Domain (PEAL: Pernambuco-Alagoas Massif).

The wide variation of the proposed cooling rates presented above shows that the ^{40}Ar/^{39}Ar method can sometimes be misleading when comparing those rates. One of the reasons is that

the mineral-specific closure temperature for Ar diffusion is dependent mainly on the cooling rate itself, among other variables such as grain size, composition and diffusion coefficients (Dodson, 1973; Schaen et al., 2021). Instead, we have used inverse thermal modeling (**Fig. 6**) in an attempt to infer a viable average cooling rate for the study area. For that, two time-temperature (t-T) constraints determine the results. The first, with higher temperature, is the ZFT constraint, that is also validated by the $^{40}Ar/^{39}Ar$ results published in the literature (160–200 °C and 500–460 Ma, see the section 5 for explanation). The second one is a geologically-constrained t-T box based on the nonconformity of the Tacaratu Fm. deposited directly on the basement of the Borborema Province. Even though the Tacaratu Fm. does not present a precise depositional age, several authors consider that this unit was deposited during the Silurian–Devonian (Carvalho et al., 2018 and references therein). Furthermore, the presence of the nonconformity of the Tacaratu Fm. not only in the Jatobá basin but in the smaller interior basins of Fátima, São José do Belmonte and Mirandiba (Correia Filho et al., 2021; Morais et al., 2021; Santos et al., 2021) reveals that the crystalline basement of the study area (part of Transversal Zone and the Pernambuco-Alagoas massif - PEAL) was near the surface during the Silurian–Devonian. Based on this evidence, we can infer that the basement of the Transversal Zone and the PEAL massif (near the Jatobá basin) experienced cooling until the Silurian–Devonian with average cooling rates of approximately 1.5 to 8.0 °C/m.y. Moreover, in order to expose the Precambrian basement in the Silurian–Devonian, the average cooling rates cannot be less than those obtained by our data. Our estimates are in agreement with one calculated by Morais Neto (2009) using the muscovite-biotite pair (2.5 °C/m.y.) from a sample that lies within the East Pernambuco shear zone, west of the Jatobá basin. However, using the biotite-K-feldspar pair, the same sample and another one close to the Fátima basin yielded cooling rates of 0.85 and 1.02 °C/m.y., respectively, during the Cambrian.

6.2 Basement thermal evolution during Meso–Cenozoic

After the end of the registered cooling by the Silurian–Devonian, the Transversal Zone and part of the PEAL massif underwent heating due to burial in response to the sedimentation of the syneclise phase (Tacaratu and Inajá formations) present in almost all interior basins of NE Brazil. The extent and duration of the heating are beyond the resolution of the AFT method. The overall cooling started in the Pernambuco shear zone region adjacent to the Jatobá basin during the Triassic. Inverse modeling of our dataset shows that samples from the East of Jatobá (EJG), South of Jatobá (SJG), and West Pernambuco (WPG) groups reveal a similar cooling history below 120 °C that started at ca. 250–200 Ma. Most of the modeled samples of those groups present a monotonic cooling that seems undisturbed until ca. 60–40 Ma (**Fig. 8**). In this sense, our data are in agreement with cooling during the Permian–Early Jurassic (ca. 300–180 Ma) constrained for basement samples of the Sertaneja Depression, west of South Tucano basin, and of the Conquista plateau, southwest of the Recôncavo basin (Jelinek et al., 2014). Closer to the study area, Jelinek et al. (2020) presented a AFT dataset north of the Vaza-Barris transfer zone, which divides the North and Central Tucano basins, and some of their samples are located in the **Fig. 2**. Based upon inverse thermal modeling, their AFT dataset also revealed a protracted cooling starting at the Permian–Triassic transition, again corroborating with our basement dataset.

In addition to that, almost all authors invoke, mainly in the region of the basement of Recôncavo-Tucano-Jatobá (RTJ), a cooling event during Early Cretaceous linked to the onset of rifting responsible for the separation between South America and Africa at ca. 130–90 Ma which culminated with the opening of the South and Equatorial Atlantic ocean (Harman et al., 1998;

Japsen et al., 2012; Jelinek et al., 2014; Matos et al., 2021; Morais Neto et al., 2009; Turner et al., 2008). This event is related with the magmatism of the EQUAMP (Hollanda et al., 2019), manifested in the region with the emplacement of the Rio Ceará-Mirim, Canindé and Riacho do Cordeiro swarms, and also an increase of the South American plate velocities (Müller et al., 2019). Our dataset, however, revealed that this cooling event is restricted only in samples that are in the rift flank of the Jatobá basin. Samples from the North of Jatobá group, represented by two inverse thermal models (LLM-49 and LLM-45A; **Fig. 8**), are located near the fault border of the Jatobá basin, called the Ibimirim fault zone. These samples yielded a start of the cooling (< 120 °C) at ca. 140–115 Ma, which is interpreted as a denudation event associated with syn-rift erosion of preexisting topography. Moreover, recently published U-Pb ages of carbonates slickenfibres from the Ibimirim fault damage zone of ca. 134–127 Ma (Ganade et al., 2022; Miranda et al., 2020) (**Fig. 8**) are also a piece of evidence of basement reactivations and vertical movements during the cooling of the northern flank of the Jatobá basin. Similarly, Jelinek et al. (2014) constrained a cooling event during Early Cretaceous (ca. 145–100 Ma) that affected not only the coastal regions, the Conquista and Borborema plateaux, but it was also localized within the Tucano rift flanks, which the authors attributed to the erosion of the rift shoulder.

During the Cenozoic, the BP experienced post-rift cooling/denudation events that potentially caused the uplift of the region (Almeida et al., 2015; Correia Filho et al., 2021; Japsen et al., 2012; Jelinek et al., 2014, 2020; Morais Neto et al., 2009; Sacek et al., 2019; Turner et al., 2008). Nevertheless, the complex architecture of the province and the superimposition of different thermal and tectonic events makes it hard to define the precise timing and possible drivers responsible for such events. To clarify the exhumation pattern, different geodynamic models were proposed to assess the epeirogenic uplift of the BP, with authors often invoking an interplay between them, such as: regional horizontal compression (Japsen et al., 2012; Jardim de Sá et al., 1999; Szatmari et al., 1987), thermal doming/uplift related to an anomalously hot shallow mantle (Klöcking et al., 2020; Ussami et al., 1999), thermomechanical erosion at the base of the lithosphere by an edge-driven convection cell (Klöcking et al., 2020; Knesel et al., 2011; Sacek et al., 2019), flexural isostasy (Bittencourt et al., 1999; Jardim de Sá et al., 1999), and magmatic underplating (Magnavita et al., 1994; Morais Neto et al., 2009; Oliveira & Medeiros, 2012).

However, the precise timing of the cooling events during Late Cretaceous–Cenozoic in the BP and in the basement of the RTJ is an ongoing debate. Some authors invoke cooling/denudation during the Neogene (< 20 Ma), although there is no consensus on the responsible mechanisms (Japsen et al., 2012; Jelinek et al., 2014; Morais Neto et al., 2009). Jelinek et al. (2014) pointed to a cooling event during the Late Cretaceous–Paleogene in the elevated portions of the Borborema plateau, whereas Japsen et al. (2012) reported a denudation from the Campanian to the Eocene that led to the complete removal of the sedimentary cover in the RTJ. Both studies invoked that tectonic uplift could explain such a cooling event, relating that to the Peruvian uplift cycle in the Andes, in the west margin of the South American plate, and to a decline in the spreading rate at the Mid-Atlantic Ridge (Cobbold & Rossello, 2003; Japsen et al., 2012). It is important to notice that the timing of this event roughly overlaps a major motion reorganization of South American, African and Antarctic plates (Harman et al., 1998 and references therein) with related crustal-scale reactivations of shear zones reported in the Pernambuco shear zone of the BP (Harman et al., 1998; Vasconcelos et al., 2019) and also in

southeast Brazil (Cogné et al., 2011). Based on our inverse thermal models (**Fig. 8**), it is possible to infer Cenozoic accelerated cooling at ca. 60–40 Ma (LLM-55) and another one starting at ca. 40–25 Ma until present-day (LLM-53C, LLM-49 and NE-15A). The former overlaps in time and could be related to the end of the Peruvian cycle in the Andes as described by Japsen et al. (2012) and Jelinek et al. (2014). The latter overlaps with, firstly, an increase in the South American plate velocity and the Incaic cycle in the Andes, and then a decrease in plate velocity and the beginning of the Quechuan cycle (**Fig. 8**). However, more AFT and (U-Th)/He data are necessary to better constrain the cooling history of the BP during the Cenozoic and to understand the possible links between uplift and crustal-scale reactivations.
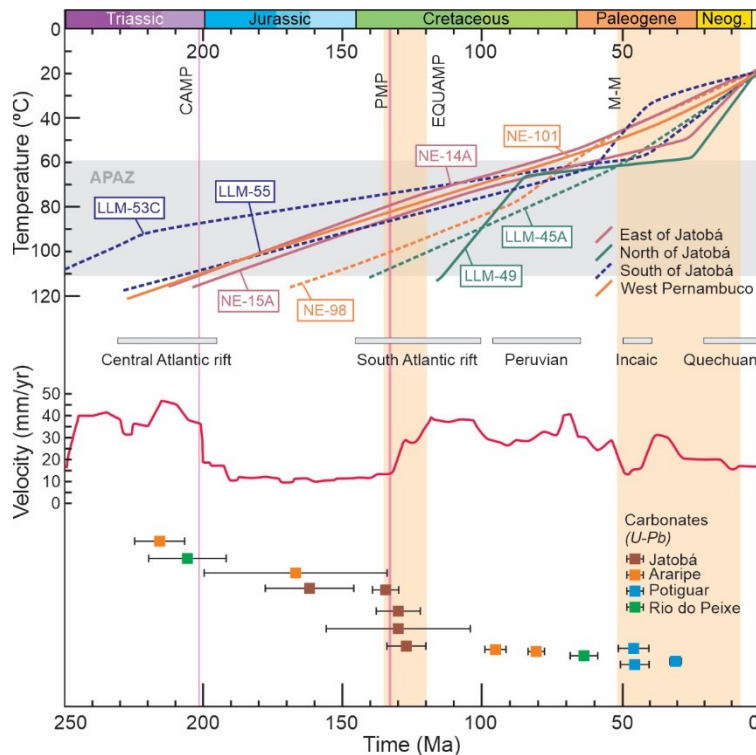
Fig. 8. The weighted mean paths of our dataset based on AFT or AFT + AHe with only the final cooling from 120 °C are in the top. The individual models and constraints are detailed in Fig. 6. Solid curves are models with a greater level of confidence (number of confined tracks > 50), whereas the dashed curves are the models with a lower level of confidence. APAZ is the apatite partial annealing zone. The Central and South Atlantic rift ages (gray bars) are from Olsen (1997) and Matos et al. (2021) respectively. The other three subsequent Andean events are from Cobbold & Rossello (2003) and references therein. Magmatic event ages (vertical lines and bars) are from Davies et al. (2017) for the Central Atlantic magmatic province (CAMP), Rocha et al. (2020) for the Paraná magmatic province (PMP), Hollanda et al. (2019) for the Equatorial Atlantic magmatic province (EQUAMP) and Guimarães et al. (2020) for the Macau-Mecejana magmatism (M-M). The red curve is the South American plate velocity modeled from Müller et al. (2019) relative to a fixed point in the Borborema Province in an absolute reference frame. At the bottom row, carbonate U-Pb ages with uncertainty bars from Cardoso et al. (2023), Celestino et al. (2021), Ganade et al. (2022) and Miranda et al. (2020).

6.3 Timing of basement reactivations and basin inversions

The Borborema Province is being reactivated possibly since its stabilization until present-day (Bezerra et al., 2011; Lima Neto et al., 2013). There is consistent evidence that the complex architecture with crustal-scale shear zones was reactivated during the Early Cretaceous rifting to form the principal interior basins, and that compressional stresses were in operation during Late Cretaceous–Cenozoic, causing basin inversions in the Araripe (Rosa et al., 2023), Rio do Peixe (Nogueira et al., 2015; Pichel et al., 2023; Vasconcelos et al., 2021) and Potiguar basins (Bezerra et al., 2020). The compressional stress field resulting from the Mid-Atlantic Ridge, in

the east, and the Andean orogeny, in the west, has been attributed by those authors as the main driver of the transtensional reactivations of those basins. However, the precise timing of reactivations and basin inversions is still contentious.

In the study area, Vasconcelos et al. (2019) suggested that the Pernambuco shear zone was reactivated in a brittle regime in at least two stages: (1) in the rift phase during Early Cretaceous under an extensional stress regime and (2) in the post-rift stage (Late Cretaceous–Quaternary) under a strike-slip stress regime. Harman et al. (1998) based on AFT data from the Pernambuco shear zone proposed an enhanced denudation during Late Cretaceous (~80–60 Ma), related to a major phase of tectonic reactivation. The authors also indicated that the timing and tectonic style were similar to reactivations that also occurred in the Central African shear zone. The deformation was a result of major changes in relative plate motions between South American, African, and Antarctic plates, during the anomalies chron 34 and chron 31 (~83 to 67 Ma). In this sense, based on our newly obtained data, we compare the AFT inverse thermal histories of the fault border of the Jatobá basin and the conglomerate from Salvador Fm. to constrain the timing of reactivations (**Fig. 9**). Two periods of accelerated cooling could represent periods of major fault activity, the first one is during ca. 130–80 Ma, when the basement was cooling and the sediments were being heated by burial. The other one from ca. 25 Ma, when both basin and basement were being cooled. Nonetheless, AFT and (U-Th)/He method resolution can only constrain a broad interval of enhanced cooling/exhumation. These methods have a better response to large wavelength features, whereas other dating methods can precisely contrain the timing of crustal movements (e.g., Roberts & Holdsworth, 2022).

Recently, the advance of the U-Pb dating method on carbonates (Roberts & Holdsworth, 2022 and references therein) shed light on the age of these reactivations and fluid circulation in the BP. Authors have demonstrated that the shear zones, and the basins themselves, underwent recurrent tectonic activity since the Triassic (**Fig. 8**) in the case of the basement of the Rio do Peixe and Araripe basins, wheareas in the Pernambuco shear zone, near the Jatobá basin, U-Pb carbonate ages are concentrated at ca. 134–127 Ma (Ganade et al., 2022; Miranda et al., 2020). North of the study area, carbonate-filled faults within the Upper Cretaceous limestones of the Jandaíra Fm. of the Potiguar basin yielded U-Pb ages of ca. 45–30 Ma (Cardoso et al., 2023). Collectively, those data revealed that the Pernambuco shear zone was in fact reactivated during our constrained interval, which is also related to the South Atlantic rift (Matos et al., 2021), the mafic magmatism of the EQUAMP (Hollanda et al., 2019) and an increase in the South American plate velocity (Müller et al., 2019) (**Fig. 8**). During the Cenozoic, the reactivation of the Potiguar basin overlaps the Incaic cycle of the Andean orogeny (Cobbold & Rossello, 2003) during an increase in plate velocity, which is in agreement with previous interpretation for that basin inversion (Bezerra et al., 2020). However, more data are necessary to fully understand the link between the basin inversions and the Andean orogenic cycles. Thus, the coupling of low-temperature thermochronology and U-Pb carbonate data to constrain fault movements can be a powerful tool to understand the timing and recurrency of tectonic reactivations and basin inversions.
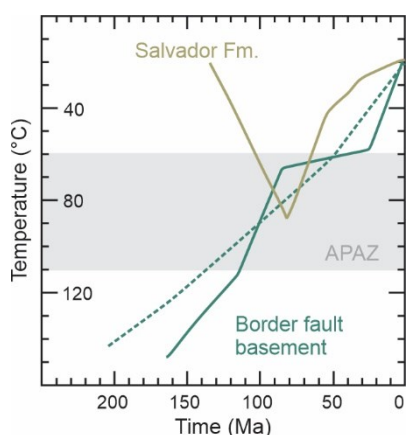
Fig. 9. Weighted mean paths of time-temperature inverse models comparing the sample LLM-47 from the Salvador Fm. of the Jatobá basin. with the adjacent rift flank within the basement (samples LLM-49 - solid - and LLM-45A - dashed). APAZ is the apatite partial annealing zone. See section 5 for modeling details.

6.4 Post-rift denudation in the Jatobá basin

The abovementioned studies based on low-temperature thermochronology of NE Brazil have demonstrated that the region underwent major cooling events during Late Cretaceous and Cenozoic, which possibly led a kilometer-scale removal of material since the breakup along the Atlantic margin (e.g. Harman et al., 1998; Japsen et al., 2012; Jelinek et al., 2014, 2020; Morais Neto et al., 2006, 2009). However, it is hard to accurately calculate the amount of denudation due to variations of paleogeothermal gradients over time. In the Araripe basin, Morais Neto et al. (2006), based on AFT and vitrinite reflectance (VR), suggested that post-rift sediments of the Exu Fm. (Albian–Cenomanian) reached maximum temperatures of ~100 to 80 °C and started to cool at ca. 110 to 40 Ma. A VR analysis from a black shale of the Aptian Barbalha Fm. yielded a value of 0.56% Ro from which the authors calculated a maximum paleotemperature of 93°C, validating the extent of the earlier heating/cooling event. Additionally, the authors pointed to a denudation of at least 1.5 km of sedimentary pile in the Araripe basin. In this sense, analyzing basement samples of the BP, Morais Neto et al. (2009) suggested that the obtained AFT results is a consequence of cooling caused by topographic erosion, demanding total denudation of 1 to 3 km since the Cretaceous breakup.

In the Jatobá basin, there is a scarcity of studies constraining the post-rift denudation, and most of published studies that refer to Recôncavo-Tucano-Jatobá rift (RTJ) are only focused on the Recôncavo and Tucano basins (e.g., Japsen et al., 2012; Jelinek et al., 2014). Invese thermal models of the conglomerate from the Salvador Fm. revealed that this sample underwent partial reset after deposition. We interpret that, at least at the sampled horizon, the syn-rift sediments experienced burial with temperatures ranging from 70 to 105 °C based on inverse thermal modeling with AFT and (U-Th)/He data, with possible paths spanning a wide time variation with maximum paleotemperatures from ca. 120 to 55 Ma (**Fig. 7**). At the Serra Negra peak (~1064 m above sea level), the preserved post-rift sedimentary pile suggests a section of at least ~650 m deposited over the syn-rift sediments, which is almost similar when comparing to the preserved post-rift section in the Araripe basin (Aptian to Cenomanian), with both continental and marine sediments reaching up thicknesses of ~770 m (Assine, 2007; Sacek et al., 2019).Based on that, these two basins must share similarities not only on the sedimentary cover and post-rift remnants, but also in the denudation pattern. Despite the wide timing variation of the maximum burial paleotemperature, it is unlikely that the burial of syn-rift sediments of the Jatobá basin lasted until 55 Ma, since there is evidence that the Pernambuco shear zone and great part of

the BP were under cooling at ca. 80–60 Ma (Harman et al., 1998). It is reasonable, however, that at ca. 100–85 Ma these sediments could have experienced the maximum burial paleotemperature (**Fig. 9**), since the Exu Fm. in the Araripe basin has a deposition estimated during the Cenomanian (~94 Ma; Assine, 2007) and there are also remnants of the Exu Fm. in the Jatobá basin (Neumann & Rocha, 2014). Assuming a paleosurface temperature of 20 °C and an average paleogeothermal gradient of 30–35 °C/km, we can estimate that the burial and posterior denudation of the syn-rift deposits of the Jatobá basin was of 1.4 to 2.8 km. Based on AFT, vitrinite reflectance and sonic data, Japsen et al. (2012) modeled an exhumation of 2.1 to 2.2 km for the Albian and Eocene–Recent episodes for the Tucano and Recôncavo basins, assuming paleosurfaces of 20–25 °C and a paleogeothermal gradient of 40 °C/km (calculated from well data). Furthermore, based on vitrinite reflectance data, Magnavita et al. (1994) calculated an erosion of more than 2 km-thick post-rift pile in the RTJ. Thus, estimates of maximum burial of 1.4 to 2.8 km of the syn-rift sequences of the Jatobá basin is in agreement with previous studies for the RTJ.

6.5 Connection of Jatobá and Araripe basins: burial during post-rift stage

Based on our newly obtained data, we can infer that the basement of the study area in the PEAL massif and part of the Transversal zone, in exception of the Jatobá rift flank, experienced monotonic cooling since ca. 250–200 Ma, with no apparent disturbance during the post-rift burial (Aptian–Cenomanian). However, it was demonstrated by the modeling of the conglomerate of the Salvador Fm. that burial is impressed in the syn-rift sediments of the Jatobá basin. If there was deposition of the post-rift sediments over the basement outside the Jatobá basin, either it was a negligible sedimentary pile, not able to sufficiently increase the temperature during burial to be impressed in the apatite fission-track (AFT) and (U-Th)/He (AHe) thermochronometers in our samples, or it could be the case of a localized deposition only restricted to areas that has already suffered subsidence during the syn-rift stage. Even though there are syn-rift sediments in the small interior basins between Araripe and RTJ, such as Mirandiba and São José do Belmonte (Santos et al., 2021), they lack of a post-rift sedimentary register.

In a comprehensive stratigraphic study of the Aptian post-rift sequence (Marizal Fm.) from the RTJ basins, Freitas et al. (2017) suggested that the creation of accommodation space during the beginning of deposition was largely controlled by mechanical subsidence, requiring recurrent rift activity during the Aptian in the RTJ. The idea of a rifting stage only limited to the Barriasian–Barremian (Costa et al., 2007) can thus be inaccurate. Moreover, only after the maximum flooding interval recorded as the shales of the Amargosa Bed (a temporal marker of the Aptian sequences in the RTJ), accommodation space filled by the Cícero Dantas Member, which is the top member of the Marizal Fm., can be related to thermal subsidence or subsidence cessation with the passive infill of the remnant topography. Based on that, it is possible to infer that at least during the onset of the post-rift stage, deposition was controlled by the reactivations of the rift flanks of the RTJ basins.

In addition to that, on a paleogeographical reconstruction based mainly on stratigraphy and paleocurrents, Freitas et al. (2017) and Varejão et al. (2016) proposed a connection between the Araripe and the RTJ basins, with a major fluvial system running southwards during the Aptian. For that hypothesis to be true, the basement of the Transveral Zone linking both remainder basins would have had to stay as a structural low during the Aptian. In our inverse thermal models of samples from North of Jatobá group, which are in the area that would have been the connection between the Tucano and the Araripe basins (**Fig. 2**), they show a different

cooling pattern than the adjacent samples (**Fig. 8)**, but there is no indication of burial during the Aptian. So, either the cooling during the Aptian was related to high denudation/exhumation rates, with concomitant cooling and deposition of the Aptian sedimentary sequences, or the Transversal Zone became a structural high at that time, diminishing the possibility of a connection between the two basins. There is still the possibility that the AFT and AHe method resolution, as being more sensitive to large wavelength features, did not capture these rapid vertical movements of the basement. Nonetheless, additional AFT and AHe is desirable to produce more thermal models in the region between those basins to better comprehend the paleogeography of the Borborema Province since the Cretaceous.

7. Conclusions

Based on inverse thermal modeling resulted from the input of our newly obtained apatite and zircon fission-track and apatite (U-Th)/He data, we conclude that the basement of the Borborema Province in the Pernambuco shear zone region and the adjacent area of the Jatobá basin experienced accelerated cooling after the orogenic cycle during the Paleozoic until the Silurian-Devonian, with estimated cooling rates from 1.5 to 8.0 °C/m.y. In addition to that, monotonic cooling has been registered since ca. 250–200 Ma for that area. In contrast, samples closer to the Ibimirim fault, the border fault of the Jatobá Basin, experienced accelerated cooling from ca. 140–115 Ma. Such a cooling event is interpreted as denudation event associated with syn-rift erosion of preexisting topography, related to the separation between South America and Africa, and it is restricted to samples close to the rift flank. Secondary cooling events during Cenozoic were also impressed in our samples at ca. 60–40 Ma and from ca. 40–25 Ma until present-day, which can be related to compressional stresses resulted from the Mid-Atlantic Ridge, in the east, and the Andes orogeny, in the west. Lastly, inverse thermal modeling of sediments from the syn-rift sequence of the Jatobá Basin revealed maximum burial temperatures of 70–105 °C until ca.100–85 Ma. Using average paleogeothermal gradients estimates, we can infer that the Jatobá Basin experienced a post-rift denudation of approximately 1.4 to 2.8 km of sedimentary pile.

References

Almeida, Y. B., Julià, J., & Frassetto, A. (2015). Crustal architecture of the Borborema Province, NE Brazil, from receiver function CCP stacks: Implications for Mesozoic stretching and Cenozoic uplift. *Tectonophysics*, *649*, 68–80. https://doi.org/10.1016/j.tecto.2015.03.001

Anderson, A. J., Hodges, K. V., & van Soest, M. C. (2017). Empirical constraints on the effects of radiation damage on helium diffusion in zircon. *Geochimica et Cosmochimica Acta*, *218*, 308–322. https://doi.org/10.1016/j.gca.2017.09.006

Araújo, M. N. C., Vasconcelos, P. M., Alves da Silva, F. C., Jardim de Sá, E. F., & Sá, J. M. (2005). 40Ar/39Ar geochronology of gold mineralization in Brasiliano strike-slip shear zones in the Borborema province, NE Brazil. *Journal of South American Earth Sciences*, *19*(4), 445–460. https://doi.org/10.1016/j.jsames.2005.06.009

Archanjo, C. J., De Hollanda, M. H. B. M., & Viegas, L. G. F. (2021). Late Ediacaran lateral-escape tectonics as recorded by the Patos shear zone (Borborema Province, NE Brazil). *Brazilian Journal of Geology*, *51*(2). https://doi.org/10.1590/2317-4889202120200132

Assine, M. L. (2007). Bacia do Araripe. *Boletim de Geociencias Da Petrobras*, *15*(2), 371–389.

Ault, A. K., Reiners, P. W., Evans, J. P., & Thomson, S. N. (2015). Linking hematite (U-Th)/He dating with the microtextural record of seismicity in the Wasatch fault damage zone, Utah, USA. *Geology*, *43*(9), 771–774. https://doi.org/10.1130/G36897.1

Ávila, C. F., Archanjo, C. J., Hollanda, M. H. B. M., Macêdo Filho, A. A. de, & Lemos-Santos, D. do V. (2020). Shear zone cooling and fabrics of synkinematic plutons evidence timing and rates of orogenic exhumation in the northwest Borborema Province (NE Brazil). *Precambrian Research*, *350*. https://doi.org/10.1016/j.precamres.2020.105940

Bezerra, F. H. R., de Castro, D. L., Maia, R. P., Sousa, M. O. L., Moura-Lima, E. N., Rossetti, D. F., et al. (2020). Postrift stress field inversion in the Potiguar Basin, Brazil – Implications for petroleum systems and evolution of the equatorial margin of South America. *Marine and Petroleum Geology*, *111*, 88–104. https://doi.org/10.1016/j.marpetgeo.2019.08.001

Bezerra, F. H. R., do Nascimento, A. F., Ferreira, J. M., Nogueira, F. C., Fuck, R. A., Neves, B. B. B., & Sousa, M. O. L. (2011). Review of active faults in the Borborema Province, Intraplate South America - Integration of seismological and paleoseismological data. *Tectonophysics*. Elsevier B.V. https://doi.org/10.1016/j.tecto.2011.08.005

Bittencourt, A. V. S. P., Dominguez, J. M. L., & Ussami, N. (1999). Flexure as a Tectonic Control on the Large Scale Geomorphic Characteristics of the Eastern Brazil Coastal Zone. *Journal of Coastal Research*, *15*(2), 505–519.

Brito Neves, B.B., Sial, A. N., Rand, H. M., & Manso, V. V. (1982). The Pernambuco-Alagoas Massif, Northeast Brazil. *Brazilian Journal of Geology*, *12*(1–3), 240–250.

Brito Neves, B.B., Santos, E. J., & Van Schmus, W. R. (2000). Tectonic history of the Borborema Province. *Tectonic Evolution of South America*, *31*, 15.

Brito Neves, B. B., Campos Neto, M. D. C., & Fuck, R. A. (1999). From Rodinia to Western Gondwana: An approach to the Brasiliano-Pan African cycle and orogenic collage. *Episodes*, *22*(3), 155–166. https://doi.org/10.18814/epiiugs/1999/v22i3/002

Brune, S., Heine, C., Pérez-Gussinyé, M., & Sobolev, S. V. (2014). Rift migration explains continental margin asymmetry and crustal hyper-extension. *Nature Communications*, *5*. https://doi.org/10.1038/ncomms5014

Cardoso, L. M. da C., Santos, T. J. S. dos, Romero, L. F., Geraldes, M. C., & Ganade, C. E. (2023). U–Pb ages via LA-ICP-MS of carbonate from brittle structures of Jandaíra formation, Potiguar basin, NE-Brazil. *Journal of South American Earth Sciences*, 104316. https://doi.org/10.1016/j.jsames.2023.104316

Carlson, W. D., Donelick, R. A., & Ketcham, R. A. (1999). Variability of apatite fission-track annealing kinetics; II, Crystallographic orientation effects. *American Mineralogist*, *84*(9), 1224–1234. https://doi.org/10.2138/am-1999-0902

Carvalho, R. R. de, Neumann, V. H., Fambrini, G. L., Assine, M. L., Vieira, M. M., Rocha, D. E. G. A. da, & Ramos, G. M. S. (2018). The basal siliciclastic Silurian-Devonian Tacaratu formation of the Jatobá basin: Analysis of facies, provenance and palaeocurrents. *Journal of South American Earth Sciences*, *88*, 94–106. https://doi.org/10.1016/j.jsames.2018.07.004

Castro, D. L., Bezerra, F. H. R., & Castelo Branco, R. M. G. (2008). Geophysical evidence of crustal-heterogeneity control of fault growth in the Neocomian Iguatu basin, NE Brazil. *Journal of South American Earth Sciences*, *26*(3), 271–285. https://doi.org/10.1016/j.jsames.2008.07.002

Caxito, F. de A., Lira Santos, L. C. M., Ganade, C. E., Bendaoud, A., Fettous, E. H., & Bouyo, M. H. (2020). Toward an integrated model of geological evolution for NE Brazil-NW Africa: The Borborema Province and its connections to the Trans-Saharan (Benino-Nigerian and Tuareg shields) and Central African orogens. *Brazilian Journal of Geology*, *50*(2). https://doi.org/10.1590/2317-4889202020190122

Celestino, M. A. L., Miranda, T. S., Mariano, G., Alencar, M. L., Buckman, J., Roberts, N. M. W., et al. (2021). Structural control and geochronology of Cretaceous carbonate breccia pipes, Crato Formation, Araripe Basin, NE Brazil. *Marine and Petroleum Geology*, *132*. https://doi.org/10.1016/j.marpetgeo.2021.105190

Cioffi, C. R., Meira, V. T., Trindade, R. I. F., Lanari, P., Ganade, C. E., & Gerdes, A. (2021). Long-lived intracontinental deformation associated with high geothermal gradients in the Seridó Belt (Borborema Province, Brazil). *Precambrian Research*, *358*. https://doi.org/10.1016/j.precamres.2021.106141

Cobbold, P. R., & Rossello, E. A. (2003). Aptian to recent compressional deformation, foothills of the Neuquén Basin, Argentina. *Marine and Petroleum Geology*, *20*(5), 429–443. https://doi.org/10.1016/S0264-8172(03)00077-1

Cogné, N., Gallagher, K., & Cobbold, P. R. (2011). Post-rift reactivation of the onshore margin of southeast Brazil: Evidence from apatite (U-Th)/He and fission-track data. *Earth and Planetary Science Letters*, *309*(1–2), 118–130. https://doi.org/10.1016/j.epsl.2011.06.025

Correia Filho, O. J., Barbosa, J. A., Silva Ramos, G. M., Cruz Oliveira, J. T., Lima de Araujo, A. F., Siqueira de Miranda, T., & Alencar, M. L. (2021). Cenozoic uplift of the Fátima Basin, NE Brazil. *Journal of South American Earth Sciences*, *112*. https://doi.org/10.1016/j.jsames.2021.103599

Corsini, M., Figueiredo, L. L., Caby, R., Féraud, G., Ruffet, G., & Vauchez, A. (1998). Thermal history of the Pan-African/Brasiliano Borborema Province of northeast Brazil deduced from 40Ar/39Ar analysis. *Tectonophysics*, *285*(1–2), 103–117. https://doi.org/10.1016/S0040-1951(97)00192-3

Costa, I. P., Bueno, G. V., Milhomem, P. da S., Lima e Silva, H. S. R., & Kosin, M. D. (2007). Sub-bacia de Tucano Norte e Bacia de Jatobá. *Boletim de Geociências de Petrobras*, *15*(2), 445–453.

Davies, J. H. F. L., Marzoli, A., Bertrand, H., Youbi, N., Ernesto, M., & Schaltegger, U. (2017). End-Triassic mass extinction started by intrusive CAMP activity. *Nature Communications*, *8*. https://doi.org/10.1038/ncomms15596

Dodson, M. H. (1973). Closure temperature in cooling geochronological and petrological systems. *Contributions to Mineralogy and Petrology*, *40*(3), 259–274. https://doi.org/10.1007/BF00373790

Donelick, R. A., O'Sullivan, P. B., & Ketcham, R. A. (2005). Apatite fission-track analysis. *Reviews in Mineralogy and Geochemistry*, *58*, 49–94. https://doi.org/10.2138/rmg.2005.58.3

Dorbath, C., Dorbath, L., Fairhead, J. D., & Stuart, G. W. (1986). A Teleseismic Delay Time Study Across the Central African Shear Zone In the Adamawa Region of Cameroon, West Africa. *Geophysical Journal of the Royal Astronomical Society*, *86*(3), 751–766. https://doi.org/10.1111/j.1365-246X.1986.tb00658.x

Farley, K. A. (2000). Helium diffusion from apatite: General behavior as illustrated by Durango fluorapatite. *Journal of Geophysical Research: Solid Earth*, *105*(B2), 2903–2914. https://doi.org/10.1029/1999jb900348

Farley, K. A., & Stockli, D. F. (2002). (U-Th)/He Dating of Phosphates: Apatite, Monazite, and Xenotime. In *Reviews in Mineralogy and Geochemistry* (Vol. 48, pp. 559–577). https://doi.org/10.2138/rmg.2002.48.15

Farley, K. A., Wolf, R. A., & Silver, L. T. (1996). The effects of long alpha-stopping distances on (U-Th)/He ages. *Geochimica et Cosmochimica Acta*, *60*(21), 4223–4229. https://doi.org/10.1016/S0016-7037(96)00193-7

Farley, K. A. (2002). (U-Th)/He dating: Techniques, calibrations, and applications. *Reviews in Mineralogy and Geochemistry*, *47*, 819–844. https://doi.org/10.2138/rmg.2002.47.18

Fernie, N., Glorie, S., Jessell, M. W., & Collins, A. S. (2018). Thermochronological insights into reactivation of a continental shear zone in response to Equatorial Atlantic rifting (northern Ghana). *Scientific Reports*, *8*(1), 1–14. https://doi.org/10.1038/s41598-018-34769-x

Fitzgerald, P. G., Baldwin, S. L., Webb, L. E., & O'Sullivan, P. B. (2006). Interpretation of (U-Th)/He single grain ages from slowly cooled crustal terranes: A case study from the Transantarctic Mountains of southern Victoria Land. *Chemical Geology*, *225*(1–2), 91–120. https://doi.org/10.1016/j.chemgeo.2005.09.001

Fitzgerald, P. G., & Malusà, M. G. (2019). Concept of the Exhumed Partial Annealing (Retention) Zone and Age-Elevation Profiles in Thermochronology. In M.G. Malusà & P. G. Fitzgerald (Eds.), *Fission-Track Thermochronology and its Application to Geology* (pp. 165–189). Springer. https://doi.org/10.1007/978-3-319-89421-8_9

Flowers, R. M., & Kelley, S. A. (2011). Interpreting data dispersion and "inverted" dates in apatite (U-Th)/He and fission-track datasets: An example from the US midcontinent. *Geochimica et Cosmochimica Acta*, *75*(18), 5169–5186. https://doi.org/10.1016/j.gca.2011.06.016

Flowers, R. M., Ketcham, R. A., Shuster, D. L., & Farley, K. A. (2009). Apatite (U-Th)/He thermochronometry using a radiation damage accumulation and annealing model. *Geochimica et Cosmochimica Acta*, *73*(8), 2347–2365. https://doi.org/10.1016/j.gca.2009.01.015

Freitas, B. T., Almeida, R. P., Carrera, S. C., Figueiredo, F. T., Turra, B. B., Varejão, F. G., & Assine, M. L. (2017). Aptian sedimentation in the Recôncavo-Tucano-Jatobá Rift System and its tectonic and paleogeographic significance. *Journal of South American Earth Sciences*, *80*, 460–481. https://doi.org/10.1016/j.jsames.2017.10.001

Galindo, A. C., & Oliveira, M. J. R. (2006). *Distribuição dos sedimentos cenozóicos nas bacias Pernambuco-Paraíba, Potiguar e Ceará, como função da epirogenia cenozóica da Província Borborema.* Projeto CRONOBORO: UFRN-PPGG/PETROBRAS. Unpublished Report. Natal, Brasil, 335 p., 2 vol.

Gallagher, K. (2012). Transdimensional inverse thermal history modeling for quantitative thermochronology. *Journal of Geophysical Research: Solid Earth*, *117*(2). https://doi.org/10.1029/2011JB008825

Gallagher, K., & Ketcham, R. A. (2018). Comment on "Thermal history modelling: HeFTy vs. QTQt" by Vermeesch and Tian, Earth-Science Reviews (2014), 139, 279–290. *Earth-Science Reviews*, *176*(September 2017), 387–394. https://doi.org/10.1016/j.earscirev.2017.11.001

Ganade, C. E., Weinberg, R. F., Caxito, F. A., Lopes, L. B. L., Tesser, L. R., & Costa, I. S. (2021). Decratonization by rifting enables orogenic reworking and transcurrent dispersal of old terranes in NE Brazil. *Scientific Reports*, *11*(1), 1–13. https://doi.org/10.1038/s41598-021-84703-x

Ganade, C. E., Cioffi, C. R., Machado, J. P., Miranda, T., Lopes, L. B., Weinberg, R. F., et al. (2022). Recurrent tectonic activity in northeastern Brazil during Pangea breakup: Constraints from U-Pb carbonate dating. *Geology*, *50*(8), 969–974. https://doi.org/10.1130/G50032.1

Gautheron, C., Tassan-Got, L., Barbarand, J., & Pagel, M. (2009). Effect of alpha-damage annealing on apatite (U-Th)/He thermochronology. *Chemical Geology*, *266*(3–4), 157–170. https://doi.org/10.1016/j.chemgeo.2009.06.001

Gleadow, A. J. W., Belton, D. X., Kohn, B. P., & Brown, R. W. (2002). Fission Track Dating of Phosphate Minerals and the Thermochronology of Apatite. In *Reviews in Mineralogy and Geochemistry* (Vol. 48, pp. 579–630). https://doi.org/10.2138/rmg.2002.48.16

Green, P., & Duddy, I. (2018). Apatite (U-Th-Sm)/He thermochronology on the wrong side of the tracks. *Chemical Geology*, *488*, 21–33. https://doi.org/10.1016/j.chemgeo.2018.04.028

Grün, R., Tani, A., Gurbanov, A., Koshchug, D., Williams, I., & Braun, J. (1999). A new method for the estimation of cooling and denudation rates using paramagnetic centers in quartz: A case study on the Eldzhurtinskiy Granite, Caucasus. *Journal of Geophysical Research*, *104*(B8), 17531–17549. https://doi.org/10.1055/b-0035-111722

Guenthner, W. R., Reiners, P. W., Ketcham, R. A., Nasdala, L., & Giester, G. (2013). Helium diffusion in natural zircon: radiation damage, anisotropy, and the interpretation of zircon (U-TH)/He thermochronology. *American Journal of Science*, *313*(3), 145–198. https://doi.org/10.2475/03.2013.01

Guimarães, A. R., Fitton, J. G., Kirstein, L. A., & Barfod, D. N. (2020). Contemporaneous intraplate magmatism on conjugate South Atlantic margins: A hotspot conundrum. *Earth and Planetary Science Letters*, *536*, 116147. https://doi.org/10.1016/j.epsl.2020.116147

Harman, R., Gallagher, K., Brown, R., Raza, A., & Bizzi, L. (1998). Accelerated denudation and tectonic/geomorphic reactivation of the cratons of northeastern Brazil during the Late Cretaceous. *Journal of Geophysical Research: Solid Earth*, *103*(B11), 27091–27105. https://doi.org/10.1029/98JB02524

Hasebe, N., Barbarand, J., Jarvis, K., Carter, A., & Hurford, A. J. (2004). Apatite fission-track chronometry using laser ablation ICP-MS. *Chemical Geology*, *207*(3–4), 135–145. https://doi.org/10.1016/j.chemgeo.2004.01.007

Heilbron, M., Cordani, U. G., & Alkmim, F. F. (2017). The São Francisco Craton and Its Margins. In M. Heilbron, U. G. Cordani, & F. F. Alkmim (Eds.), *São Francisco Craton, Eastern Brazil: Tectonic Genealogy of a Miniature Continent* (pp. 3–13). Springer International Publishing. https://doi.org/10.1007/978-3-319-01715-0_1

Heine, C., Zoethout, J., & Müller, R. D. (2013). Kinematics of the South Atlantic rift. *Solid Earth*, *4*(2), 215–253. https://doi.org/10.5194/se-4-215-2013

Heineke, C., Hetzel, R., Nilius, N.-P., Zwingmann, H., Todd, A., Mulch, A., et al. (2019). Detachment faulting in a bivergent core complex constrained by fault gouge dating and low-temperature thermochronology. *Journal of Structural Geology*, *127*(January), 103865. https://doi.org/10.1016/j.jsg.2019.103865

Herman, F., Rhodes, E. J., Braun, J., & Heiniger, L. (2010). Uniform erosion rates and relief amplitude during glacial cycles in the Southern Alps of New Zealand, as revealed from OSL-thermochronology. *Earth and Planetary Science Letters*, *297*(1–2), 183–189. https://doi.org/10.1016/j.epsl.2010.06.019

Hollanda, M. H. B. M., Archanjo, C. J., Macedo-Filho, A. A., Fossen, H., Ernst, R. E., Castro, D. L., et al. (2019). Equatorial Atlantic Magmatic Province (EQUAMP). In R. K. Srivastava, R. E. Ernst, & P. Peng (Eds.), *Dyke Swarms of the World: A Modern Perspective* (pp. 87–110). Singapore: Springer Singapore. https://doi.org/10.1007/978-981-13-1666-1

Horn, B. L. D., & Morais, D. M. F. (2016). First occurrence of the Salvador Formation in the Jatobá Basin (Pernambuco, Northeast Brazil): Facies characterization and depositional systems. *Journal of South American Earth Sciences*, *72*, 25–37. https://doi.org/10.1016/j.jsames.2016.07.007

Hourigan, J. K., Reiners, P. W., & Brandon, M. T. (2005). U-Th zonation-dependent alpha-ejection in (U-Th)/He chronometry. *Geochimica et Cosmochimica Acta*, *69*(13), 3349–3365. https://doi.org/10.1016/j.gca.2005.01.024

Huismans, R. S., & Beaumont, C. (2014). Rifted continental margins: The case for depth-dependent extension. *Earth and Planetary Science Letters*, *407*, 148–162. https://doi.org/10.1016/j.epsl.2014.09.032

Japsen, P., Bonow, J. M., Green, P. F., Cobbold, P. R., Chiossi, D., Lilletveit, R., et al. (2012). Episodic burial and exhumation in NE Brazil after opening of the South Atlantic. *Bulletin of the Geological Society of America*, *124*(5–6), 800–816. https://doi.org/10.1130/B30515.1

Jardim de Sá, E. F., Matos, R. M. D., Morais Neto, J. M., Saadi, A., & Pessoa Neto, O. C. (1999). Epirogenia cenozóica na Província Borborema: Síntese e discussão sobre os modelos da deformação associados. In *VII Simpósio Nacional de Estudos Tectônicos, Boletim de Resumos Expandidos* (pp. 160–162). Retrieved from https://www.researchgate.net/publication/264424415

Jelinek, A. R., Chemale, F., van der Beek, P. A., Guadagnin, F., Cupertino, J. A., & Viana, A. (2014). Denudation history and landscape evolution of the northern East-Brazilian continental margin from apatite fission-track thermochronology. *Journal of South American Earth Sciences*, *54*, 158–181. https://doi.org/10.1016/j.jsames.2014.06.001

Jelinek, A. R., Corrêa-Gomes, L. C., & Bicca, M. M. (2020). Evolução termotectônica fanerozoica da margem continental na área do Rifte Recôncavo-Tucano-Jatobá. *Pesquisas Em Geociências*, *47*(1). https://doi.org/10.22456/1807-9806.101330

Ketcham, R. A. (2005). Forward and Inverse Modeling of Low-Temperature Thermochronometry Data. *Reviews in Mineralogy and Geochemistry*, *58*(1), 275–314. https://doi.org/10.2138/rmg.2005.58.11

Ketcham, R. A. (2019). Fission-Track Annealing: From Geologic Observations to Thermal History Modeling. In *Fission-Track Thermochronology and its Application to Geology, Springer Textbooks in Earth Sciences, Geography and Environment* (pp. 49–75). Springer International Publishing. https://doi.org/10.1007/978-3-319-89421-8_3

Ketcham, R. A, Donelick, R. A., & Carlson, W. D. (1999). *Variability of apatite fission-track annealing kinetics: III. Extrapolation to geological time scales*. *American Mineralogist* (Vol. 84).

Ketcham, R. A., Carter, A., Donelick, R. A., Barbarand, J., & Hurford, A. J. (2007). Improved modeling of fission-track annealing in apatite. *American Mineralogist*, *92*(5–6), 799–810. https://doi.org/10.2138/am.2007.2281

Ketcham, R. A., Gautheron, C., & Tassan-Got, L. (2011). Accounting for long alpha-particle stopping distances in (U-Th-Sm)/He geochronology: Refinement of the baseline case. *Geochimica et Cosmochimica Acta*, *75*(24), 7779–7791. https://doi.org/10.1016/j.gca.2011.10.011

Ketcham, R. A., van der Beek, P., Barbarand, J., Bernet, M., & Gautheron, C. (2018). Reproducibility of Thermal History Reconstruction From Apatite Fission-Track and (U-Th)/He Data. *Geochemistry, Geophysics, Geosystems*, *19*(8), 2411–2436. https://doi.org/10.1029/2018GC007555

King, G. E., Herman, F., & Guralnik, B. (2016). Northward migration of the eastern Himalayan syntaxis revealed by OSL thermochronometry. *Science*, *353*(6301), 800–804. https://doi.org/10.1126/science.aaf2637

Klöcking, M., Hoggard, M. J., Rodríguez Tribaldos, V., Richards, F. D., Guimarães, A. R., Maclennan, J., & White, N. J. (2020). A tale of two domes: Neogene to recent volcanism

and dynamic uplift of northeast Brazil and southwest Africa. *Earth and Planetary Science Letters*, *547*. https://doi.org/10.1016/j.epsl.2020.116464

Knesel, K. M., Souza, Z. S., Vasconcelos, P. M., Cohen, B. E., & Silveira, F. V. (2011). Young volcanism in the Borborema Province, NE Brazil, shows no evidence for a trace of the Fernando de Noronha plume on the continent. *Earth and Planetary Science Letters*, *302*(1–2), 38–50. https://doi.org/10.1016/j.epsl.2010.11.036

Kohn, B., & Gleadow, A. (2019). Application of Low-Temperature Thermochronology to Craton Evolution. In *Fission-Track Thermochronology and its Application to Geology* (pp. 373–393). https://doi.org/10.1007/978-3-319-89421-8_21

Kohn, B., Chung, L., & Gleadow, A. (2019). Fission-Track Analysis: Field Collection, Sample Preparation and Data Acquisition. In *Fission-Track Thermochronology and its Application to Geology* (pp. 25–48). https://doi.org/10.1007/978-3-319-89421-8_2

Ksienzyk, A. K., Dunkl, I., Jacobs, J., Fossen, H., & Kohlmann, F. (2014). From orogen to passive margin: Constraints from fission track and (U-Th)/he analyses on mesozoic uplift and fault reactivation in SW Norway. *Geological Society Special Publication*, *390*(1), 679–702. https://doi.org/10.1144/SP390.27

Laslett, G. M., Green, P. F., Duddy, I. R., & Gleadow, A. J. W. (1987). *Thermal Annealing of Fission Tracks in Apatite 2. A Quantitative Analysis*. *Chemical Geology (Isotope Geoscience Section)* (Vol. 65).

Lima Neto, H. C., Ferreira, J. M., Bezerra, F. H. R., Assumpção, M. S., do Nascimento, A. F., Sousa, M. O. L., & Menezes, E. A. S. (2013). Upper crustal earthquake swarms in São Caetano: Reactivation of the Pernambuco shear zone and trending branches in intraplate Brazil. *Tectonophysics*, *608*, 804–811. https://doi.org/10.1016/j.tecto.2013.08.001

Lippolt, H. J., Leitz, M., Wernicke, R. S., & Hagedorn, B. (1994). *(Uranium + thorium)/helium dating of apatite: experience with samples from different geochemical environments*. *Chemical Geology (Isotope Geoscience Section)* (Vol. 112).

Lister, G. S., Etheridge, M. A., & Symonds, P. A. (1991). Detachment models for the formation of passive continental margins. *Tectonics*, *10*(5), 1038–1064. https://doi.org/10.1029/90TC01007

Magnavita, L. P., Davison, I., & Kusznir, N. J. (1994). Rifting, erosion, and uplift history of the Recbncavo-Tucano-JatobJ Rift, northeast Brazil. *Tectonics*, *13*(2), 367–388.

Maino, M., Casini, L., Ceriani, A., Decarlis, A., Di Giulio, A., Seno, S., et al. (2015). Dating shallow thrusts with zircon (U-Th)/he thermochronometry-the shear heating connection. *Geology*, *43*(6), 495–498. https://doi.org/10.1130/G36492.1

Malusà, M.G., & Fitzgerald, P. G. (2019). *Fission-Track Thermochronology and its Application to Geology*. (Marco G. Malusà & P. G. Fitzgerald, Eds.). Springer International Publishing. https://doi.org/10.1007/978-3-319-89421-8

Marzoli, A., Renne, P. R., Piccirillo, E. M., Ernesto, M., Bellieni, G., & Min, A. De. (1999). Extensive 200-Million-Year-Old Continental Flood Basalts of the Central Atlantic Magmatic Province. *Science*, *284*(5414), 616–618. https://doi.org/10.1126/science.284.5414.616

Marzoli, A., Callegaro, S., Dal Corso, J., Davies, J. H. F. L., Chiaradia, M., Youbi, N., et al. (2018). The Central Atlantic Magmatic Province (CAMP): A Review. In L. Tanner (Ed.), *The Late Triassic World* (Vol. 46, pp. 91–125). Springer. https://doi.org/10.1007/978-3-319-68009-5_4

Matos, R. M. D. (1992). The Northeast Brazilian Rift System. *Tectonics*, *11*(4), 766–791. https://doi.org/10.1029/91TC03092

Matos, R. M. D. (1999). History of the northeast Brazilian rift system: kinematic implications for the break-up between Brazil and West Africa. *Geological Society, London, Special Publications*, *153*(1), 55–73. https://doi.org/10.1144/GSL.SP.1999.153.01.04

Matos, R. M. D., Krueger, A., Norton, I., & Casey, K. (2021). The fundamental role of the Borborema and Benin–Nigeria provinces of NE Brazil and NW Africa during the development of the South Atlantic Cretaceous Rift system. *Marine and Petroleum Geology*, *127*(September 2020), 104872. https://doi.org/10.1016/j.marpetgeo.2020.104872

McDowell, F. W., McIntosh, W. C., & Farley, K. A. (2005). A precise 40Ar-39Ar reference age for the Durango apatite (U-Th)/He and fission-track dating standard. *Chemical Geology*, *214*(3–4), 249–263. https://doi.org/10.1016/j.chemgeo.2004.10.002

De Min, A., Piccirillo, E. M., Marzoli, A., Bellieni, G., Renne, P. R., Ernesto, M., & Marques, L. S. (2003). The Central Atlantic Magmatic Province (CAMP) in Brazil: Petrology, geochemistry, 40Ar/39Ar ages, paleomagnetism and geodynamic implications. In *Geophysical Monograph Series* (Vol. 136, pp. 91–128). https://doi.org/10.1029/136GM06

Miranda, T. S., Neves, S. P., Celestino, M. A. L., & Roberts, N. M. W. (2020). Structural evolution of the Cruzeiro do Nordeste shear zone (NE Brazil): Brasiliano-Pan-African- ductile-to-brittle transition and Cretaceous brittle reactivation. *Journal of Structural Geology*, *141*(March). https://doi.org/10.1016/j.jsg.2020.104203

Morais, D., Oliveira, R., Lages, G., & Galvão, M. (2021). The geometry, sedimentary filling and depth estimate of the Mirandiba Basin, Pernambuco, Brazil: new insights about the depositional regional gap of rift phases in the interior basins. *Journal of the Geological Survey of Brazil*, *4*(1), 1–21. https://doi.org/10.29396/jgsb.2021.v4.n1.1

Morais Neto, J. M. (2009). *Thermochronology, landscape evolution and denudational history of the eastern Borborema Province, northeastern Brazil*. Doctoral thesis. The University of Queensland.

Morais Neto, J. M., Hegarty, K., & Karner, G. D. (2006). Abordagem preliminar sobre paleotemperatura e evolução do relevo da Bacia do Araripe, Nordeste do Brasil, a partir da análise de traços de fissão em apatita. *Boletim de Geociencias Da Petrobras*, *14*(1), 113–119.

Morais Neto, J. M., Hegarty, K. A., Karner, G. D., & Alkmim, F. F. (2009). Timing and mechanisms for the generation and modification of the anomalous topography of the Borborema Province, northeastern Brazil. *Marine and Petroleum Geology*, *26*(7), 1070–1086. https://doi.org/10.1016/j.marpetgeo.2008.07.002

Moulin, M., Aslanian, D., & Unternehr, P. (2010, January 1). A new starting point for the South and Equatorial Atlantic Ocean. *Earth-Science Reviews*. Elsevier B.V. https://doi.org/10.1016/j.earscirev.2009.08.001

Müller, R. D., Zahirovic, S., Williams, S. E., Cannon, J., Seton, M., Bower, D. J., et al. (2019). A Global Plate Model Including Lithospheric Deformation Along Major Rifts and Orogens Since the Triassic. *Tectonics*, *38*(6), 1884–1907. https://doi.org/10.1029/2018TC005462

Murakami, M., & Tagami, T. (2004). Dating pseudotachylyte of the Nojima fault using the zircon fission-track method. *Geophysical Research Letters*, *31*(12). https://doi.org/10.1029/2004GL020211

Murakami, M., Košler, J., Takagi, H., & Tagami, T. (2006). Dating pseudotachylyte of the Asuke Shear Zone using zircon fission-track and U-Pb methods. *Tectonophysics*, *424*(1–2), 99–107. https://doi.org/10.1016/j.tecto.2006.06.006

Nascimento, M. A. L., Vasconcelos, P. M., Souza, Z. S., Jardim De Sá, E. F., Carmo, I. O., & Thiede, D. (2003). 40Ar/39Ar Geochronology of the Cabo Magmatic Province, Pernambuco Basin, NE Brazil. In *Short Papers - IV South American Symposium on Isotope Geology* (pp. 624–627).

Neumann, V. H., & Rocha, D. E. G. A. (2014). Stratigraphy of the Post-Rift Sequences of the Jatobá Basin, Northeastern Brazil. In R. Rocha, J. Pais, J. Kullberg, & S. Finney (Eds.), *STRATI 2013* (pp. 553–557). Springer Geology. https://doi.org/10.1007/978-3-319-04364-7_106

Neves, S. P., Mariano, G., Guimarães, I. P., da Silva Filho, A. F., & Melo, S. C. (2000a). Intralithospheric differentiation and crustal growth: Evidence from the Borborema province, northeastern Brazil. *Geology*, *28*(6), 519–522. https://doi.org/10.1130/0091-7613(2000)028<0519:IDACGE>2.3.CO;2

Neves, S. P., Vauchez, A., & Feraud, G. (2000b). Tectono-thermal evolution, magma emplacement, and shear zone development in the Caruaru area (Borborema Province, NE Brazil). *Precambrian research*, *99*(1-2), 1-32. https://doi.org/10.1016/S0301-9268(99)00026-1

Neves, S. P., & Mariano, G. (1999). Assessing the tectonic significance of a large-scale transcurrent shear zone system: the Pernambuco lineament, northeastern Brazil. *Journal of Structural Geology*, *21*(10), 1369–1383. https://doi.org/10.1016/S0191-8141(99)00097-8

Neves, S.P. (2021). Comparative geological evolution of the Borborema Province and São Francisco Craton (eastern Brazil): Decratonization and crustal reworking during West Gondwana assembly and implications for paleogeographic reconstructions. *Precambrian Research*, *355*, 106119. https://doi.org/10.1016/j.precamres.2021.106119

Nóbrega, M. A., Sá, J. M., Bezerra, F. H. R., Hadler Neto, J. C., Iunes, P. J., Guedes, S., et al. (2005). The use of apatite fission track thermochronology to constrain fault movements and sedimentary basin evolution in northeastern Brazil. *Radiation Measurements*, *39*(6), 627–633. https://doi.org/10.1016/j.radmeas.2004.12.006

Nogueira, F. C. C., Marques, F. O., Bezerra, F. H. R., de Castro, D. L., & Fuck, R. A. (2015). Cretaceous intracontinental rifting and post-rift inversion in NE Brazil: Insights from the Rio do Peixe Basin. *Tectonophysics*, *644*, 92–107. https://doi.org/10.1016/j.tecto.2014.12.016

Oliveira, R. G., & Medeiros, W. E. (2012). Evidences of buried loads in the base of the crust of Borborema Plateau (NE Brazil) from Bouguer admittance estimates. *Journal of South American Earth Sciences*, *37*, 60–76. https://doi.org/10.1016/j.jsames.2012.02.004

Olsen, P. E. (1997). Stratigraphic Record Of The Early Mesozoic Breakup Of Pangea In The Laurasia-Gondwana Rift System. *Annu. Rev. Earth Planet. Sci*, *25*, 337–401. Retrieved from www.annualreviews.org

Paton, D. (2012). Post-Rift Deformation of the North East and South Atlantic Margins: Are "Passive Margins" Really Passive? In *Tectonics of Sedimentary Basins: Recent Advances* (pp. 249–269). John Wiley and Sons. https://doi.org/10.1002/9781444347166.ch12

Pessano, P. C., Ganade, C. E., Tupinambá, M., & Teixeira, W. (2021). Updated map of the mafic dike swarms of Brazil based on airborne geophysical data. *Journal of South American Earth Sciences*, *107*. https://doi.org/10.1016/j.jsames.2020.103076

Pichel, L. M., Antunes, A. F., Fossen, H., Rapozo, B. F., Finch, E., & Córdoba, V. C. (2023). The interplay between basement fabric, rifting, syn-rift folding, and inversion in the Rio do Peixe Basin, NE Brazil. *Basin Research*, *35*(1), 61–85. https://doi.org/10.1111/bre.12704

Reiners, P. W. (2005). Zircon (U-TH)/He thermochronometry. In *Reviews in Mineralogy and Geochemistry, 58*, 151–179. https://doi.org/10.2138/rmg.2005.58.6

Reiners, P. W., Ehlers, T. A., & Zeitler, P. K. (2005). Past, present, and future of thermochronology. *Reviews in Mineralogy and Geochemistry*, *58*, 1–18. https://doi.org/10.2138/rmg.2005.58.1

Renne, P. R., Mundil, R., Balco, G., Min, K., & Ludwig, K. R. (2010). Joint determination of 40K decay constants and 40Ar*/40K for the Fish Canyon sanidine standard, and improved accuracy for 40Ar/39Ar geochronology. *Geochimica et Cosmochimica Acta*, *74*(18), 5349–5367. https://doi.org/10.1016/j.gca.2010.06.017

Roberts, N. M. W., & Holdsworth, R. E. (2022). Timescales of faulting through calcite geochronology: A review. *Journal of Structural Geology*, *158*. https://doi.org/10.1016/j.jsg.2022.104578

Rocha, B. C., Janasi, V. A., Polo, L. A., Rocha, B. C., Davies, J. H. F. L., Schaltegger, U., et al. (2020). Rapid eruption of silicic magmas from the Paraná magmatic province (Brazil) did not trigger the Valanginian event. *Geology*, *48*(12), 1174–1178. https://doi.org/10.1130/G47766.1

Rocha, D. E. G. A., & Leite, J. F. (1999). *Estudo hidrogeológico da Bacia do Jatobá–PE: Geologia*. Serviço Geológico do Brasil (CPRM) Série Hidrogeologia, Estudos e Projetos 2, 20 p.

Rodríguez Tribaldos, V., White, N. J., Roberts, G. G., & Hoggard, M. J. (2017). Spatial and temporal uplift history of South America from calibrated drainage analysis. *Geochemistry, Geophysics, Geosystems*, *18*(6), 2321–2353. https://doi.org/10.1002/2017GC006909

Rosa, M. C., Morales, N., & Assine, M. L. (2023). Transtensional tectonics during the Gondwana breakup in northeastern Brazil: Early Cretaceous paleostress inversion in the Araripe Basin. *Tectonophysics*, *846*. https://doi.org/10.1016/j.tecto.2022.229666

Sacek, V., de Morais Neto, J. M., Vasconcelos, P. M., & de Oliveira Carmo, I. (2019). Numerical Modeling of Weathering, Erosion, Sedimentation, and Uplift in a Triple Junction Divergent Margin. *Geochemistry, Geophysics, Geosystems*, *20*(5), 2334–2354. https://doi.org/10.1029/2018GC008124

Salomon, E., Koehn, D., Passchier, C., Hackspacher, P. C., & Glasmacher, U. A. (2015). Contrasting stress fields on correlating margins of the South Atlantic. *Gondwana Research*, *28*(3), 1152–1167. https://doi.org/10.1016/j.gr.2014.09.006

Santos, F. G., Pinéo, T. R. G., Medeiros, V. C. de, Santana, J. dos S., Morais, D. M. F. de, Vale, J. A. R. do, & Wanderley, A. A. (2021). *Mapa Geológico da Província Borborema. Projeto Geologia e Potencial Mineral da Província Borborema. Escala 1:1.000.000*.

Schaen, A. J., Jicha, B. R., Hodges, K. V., Vermeesch, P., Stelten, M. E., Mercer, C. M., et al. (2021). Interpreting and reporting 40Ar/39Ar geochronologic data. *Bulletin of the Geological Society of America*, *133*(3–4), 461–487. https://doi.org/10.1130/B35560.1

Schildgen, T. F., & van der Beek, P. A. (2019). The Application of Low-Temperature Thermochronology to the Geomorphology of Orogenic Systems. In *Fission-Track Thermochronology and its Application to Geology* (pp. 335–350). https://doi.org/10.1007/978-3-319-89421-8_19

Schneider, D. A., & Issler, D. R. (2019). Application of Low-Temperature Thermochronology to Hydrocarbon Exploration. In *Fission-Track Thermochronology and its Application to Geology* (pp. 315–333). https://doi.org/10.1007/978-3-319-89421-8_18

Shuster, D. L., Flowers, R. M., & Farley, K. A. (2006). The influence of natural radiation damage on helium diffusion kinetics in apatite. *Earth and Planetary Science Letters*, *249*(3–4), 148–161. https://doi.org/10.1016/j.epsl.2006.07.028

Sial, A. N., Vasconcelos, P. M., Ferreira, V. P., Pessoa, R. R., Brasilino, R. G., & Morais Neto, J. M. (2008). Geochronological and mineralogical constraints on depth of emplacement and ascencion rates of epidote-bearing magmas from northeastern Brazil. *Lithos*, *105*(3–4), 225–238. https://doi.org/10.1016/j.lithos.2008.04.002

Soares, C. J., Guedes, S., Hadler, J. C., Mertz-Kraus, R., Zack, T., & Iunes, P. J. (2014). Novel calibration for LA-ICP-MS-based fission-track thermochronology. *Physics and Chemistry of Minerals*, *41*(1), 65–73. https://doi.org/10.1007/s00269-013-0624-2

Soares, C. J., Mertz-Kraus, R., Guedes, S., Stockli, D. F., & Zack, T. (2015). Characterisation of Apatites as Potential Uranium Reference Materials for Fission-track Dating by LA-ICP-MS. *Geostandards and Geoanalytical Research*, *39*(3), 305–313. https://doi.org/10.1111/j.1751-908X.2014.00301.x

Souza, Z. S., Vasconcelos, P. M., Nascimento, M. A. L., Silveira, F. V., Paiva, H. S., Dias, L. G. S., et al. (2003). 40Ar/39Ar Geochronology of Mesozoic and Cenozoic Magmatism in NE Brazil. In *Short Papers - IV South American Symposium on Isotope Geology* (pp. 691–694).

Spiegel, C., Kohn, B., Belton, D., Berner, Z., & Gleadow, A. (2009). Apatite (U-Th-Sm)/He thermochronology of rapidly cooled samples: The effect of He implantation. *Earth and Planetary Science Letters*, *285*(1–2), 105–114. https://doi.org/10.1016/j.epsl.2009.05.045

Stockli, D. F. (2005). Application of Low-Temperature Thermochronometry to Extensional Tectonic Settings. *Reviews in Mineralogy & Geochemistry*, *58*, 411–448. https://doi.org/10.2138/rmg.2005.58.16

Stockli, D. F., Farley, K. A., & Dumitru, T. A. (2000). Calibration of the apatite (U-Th)/He thermochronometer on an exhumed fault block, White Mountains, California. *Geology*, *28*(11), 983. https://doi.org/10.1130/0091-7613(2000)28<983:COTAHT>2.0.CO;2

Szatmari, P., Françolin, J. B., Zanotto, O., & Wolff, S. (1987). Evolução Tectônica da Margem Equatorial Brasileira. *Brazilian Journal of Geology*, *17*(2), 180–188.

Tagami, T. (2005). Zircon fission-track thermochronology and applications to fault studies. *Reviews in Mineralogy and Geochemistry*, *58*, 95–122. https://doi.org/10.2138/rmg.2005.58.4

Tagami, T. (2012). Thermochronological investigation of fault zones. *Tectonophysics*, *538–540*, 67–85. https://doi.org/10.1016/j.tecto.2012.01.032

Tagami, T. (2019). Application of Fission-Track Thermochronology to Understand Fault Zones. In *Fission-Track Thermochronology and its Application to Geology* (pp. 221–233). https://doi.org/10.1007/978-3-319-89421-8_12

Tagami, T., & O'Sullivan, P. B. (2005). Fundamentals of fission-track thermochronology. *Reviews in Mineralogy and Geochemistry*, *58*(1992), 19–47. https://doi.org/10.2138/rmg.2005.58.2

Tsukamoto, S., Tagami, T., & Zwingmann, H. (2020). Direct dating of fault movement. In David Tanner & Christian Brandes (Eds.), *Understanding Faults* (1st ed., Vol. 2, pp. 257–282). Elsevier Inc. https://doi.org/10.1016/B978-0-12-815985-9.00007-2

Turner, J. P., Green, P. F., Holford, S. P., & Lawrence, S. R. (2008). Thermal history of the Rio Muni (West Africa)-NE Brazil margins during continental breakup. *Earth and Planetary Science Letters*, *270*(3–4), 354–367. https://doi.org/10.1016/j.epsl.2008.04.002

Ussami, N., Molina, E. C., & Medeiros, W. E. (1999). Novos vínculos sobre a evolução térmica da margem continental leste do Brasil. In *Simpósio Nacional de Estudos Tectônicos* (pp. 20–23). SBG - Núcleo Bahia/Sergipe, ABGP.

Varejão, F. G., Warren, L. V., Perinotto, J. A. de J., Neumann, V. H., Freitas, B. T., Almeida, R. P. de, & Assine, M. L. (2016). Upper Aptian mixed carbonate-siliciclastic sequences from Tucano Basin, Northeastern Brazil: Implications for paleogeographic reconstructions following Gondwana break-up. *Cretaceous Research*, *67*, 44–58. https://doi.org/10.1016/j.cretres.2016.06.014

Vasconcelos, D. L., Bezerra, F. H. R., Medeiros, W. E., de Castro, D. L., Clausen, O. R., Vital, H., & Oliveira, R. G. (2019). Basement fabric controls rift nucleation and postrift basin inversion in the continental margin of NE Brazil. *Tectonophysics*, *751*, 23–40. https://doi.org/10.1016/j.tecto.2018.12.019

Vasconcelos, D. L., Marques, F. O., Nogueira, F. C. C., Perez, Y. A. R., Bezerra, F. H. R., Stohler, R. C., & Souza, J. A. B. (2021). Tectonic inversion assessed by integration of geological and geophysical data: The intracontinental Rio do Peixe Basin, NE Brazil. *Basin Research*, *33*(1), 705–728. https://doi.org/10.1111/bre.12491

Vauchez, A., & Egydio-Silva, M. (1992). Termination of a continental-scale strike-slip fault in partially melted crust: The West Pernambuco shear zone, northeast Brazil. *Geology*, *20*(11), 1007. https://doi.org/10.1130/0091-7613(1992)020<1007:TOACSS>2.3.CO;2

Vauchez, A., Neves, S., Caby, R., Corsini, M., Egydio-Silva, M., Arthaud, M., & Amaro, V. (1995). The Borborema shear zone system, NE Brazil. *Journal of South American Earth Sciences*, *8*(3–4), 247–266. https://doi.org/10.1016/0895-9811(95)00012-5

Vermeesch, P. (2018). IsoplotR: A free and open toolbox for geochronology. *Geoscience Frontiers*, *9*(5), 1479–1493. https://doi.org/10.1016/j.gsf.2018.04.001

Vermeesch, P., & Tian, Y. (2014). Thermal history modelling: HeFTy vs. QTQt. *Earth-Science Reviews*, *139*, 279–290. https://doi.org/10.1016/j.earscirev.2014.09.010

Vermeesch, P., & Tian, Y. (2018). Reply to Comment on "Thermal history modelling: HeFTy vs. QTQt" by K. Gallagher and R.A. Ketcham. *Earth-Science Reviews*, *176*(November 2017), 395–396. https://doi.org/10.1016/j.earscirev.2017.11.015

Wiedenbeck, M., Allé, P., Corfu, F., Griffin, W. L., Meier, M., Oberli, F., et al. (1995). Three Natural Zircon Standards for U-Th-Pb, Lu-Hf, Trace Element and REE Analyses. *Geostandards Newsletter*, *19*(1), 1–23.

Wildman, M., Brown, R., Beucher, R., Persano, C., Stuart, F., Gallagher, K., et al. (2016). The chronology and tectonic style of landscape evolution along the elevated Atlantic continental margin of South Africa resolved by joint apatite fission track and (U-Th-Sm)/He thermochronology. *Tectonics*, *35*(3), 511–545. https://doi.org/10.1002/2015TC004042

Wildman, M., Cogné, N., & Beucher, R. (2019). Fission-Track Thermochronology Applied to the Evolution of Passive Continental Margins. In *Fission-Track Thermochronology and its Application to Geology* (pp. 351–371). https://doi.org/10.1007/978-3-319-89421-8_20

Wölfler, A., Kurz, W., Danišík, M., & Rabitsch, R. (2010). Dating of fault zone activity by apatite fission track and apatite (U-Th)/He thermochronometry: A case study from the Lavanttal fault system (Eastern Alps). *Terra Nova*, *22*(4), 274–282. https://doi.org/10.1111/j.1365-3121.2010.00943.x

Yamada, K., Hanamuro, T., Tagami, T., Shimada, K., Takagi, H., Yamada, R., & Umeda, K. (2012). The first (U-Th)/He thermochronology of pseudotachylyte from the Median Tectonic Line, southwest Japan. *Journal of Asian Earth Sciences*, *45*, 17–23. https://doi.org/10.1016/j.jseaes.2011.08.009

Zeitler, P. K., Herczeg, A. L., McDougall, I., & Honda, M. (1987). U-Th-He dating of apatite: A potential thermochronometer. *Geochimica et Cosmochimica Acta*, *51*(10), 2865–2868. https://doi.org/10.1016/0016-7037(87)90164-5

Ziegler, P. A., & Cloetingh, S. (2004). Dynamic processes controlling evolution of rifted basins. *Earth-Science Reviews*, *64*(1–2), 1–50. https://doi.org/10.1016/S0012-8252(03)00041-2

Supplementary material

Analyzed samples

NE-06A - Ultramylonite
Itaporanga Suite

NE-07D - Granitic mylonite
Vila Moderna Suite

NE-14A - Migmatite
Vila Moderna Suite

NE-15A - Orthogneiss
Vila Moderna Suite

NE-96 - Mylonite
Floresta-Airi Suite

LLM-49 - Diatexite
Belém do São Francisco Complex

LLM-45A - Syenogranite
Itaporanga Suite

LLM-47 - Conglomerate
Salvador Formation
Jatobá Basin
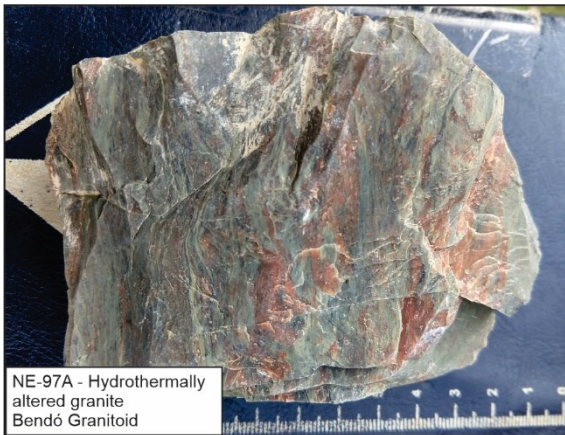
NE-97A - Hydrothermally altered granite Bendó Granitoid
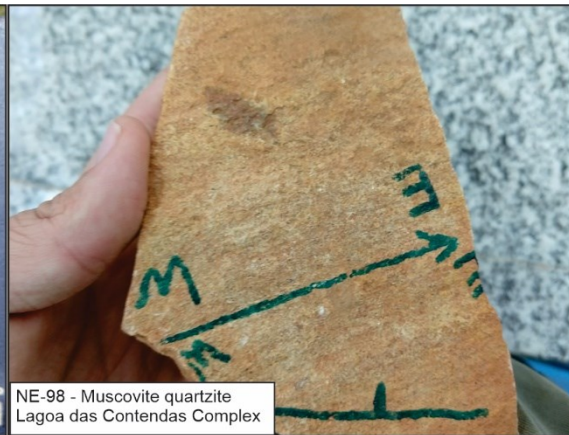
NE-98 - Muscovite quartzite Lagoa das Contendas Complex

NE-99 - Muscovite quartzite Lagoa das Contendas Complex

NE-100 - Muscovite quartzite Lagoa das Contendas Complex

NE-101 - Muscovite quartzite Lagoa das Contendas Complex

LLM-53C - Syenogranite Chorrochó Suite

LLM-55 - Metagranite Chorrochó Suite

LLM-59 - Granite Belém do São Francisco Complex

Apatite fission-track radial plots and mean track length

Single-grain apatite fission-track ages and Dpar values. All diagrams were generated in the IsoplotR (Vermeesch, 2018).

References

Vermeesch, P. (2018). IsoplotR: A free and open toolbox for geochronology. *Geoscience Frontiers*, *9*(5), 1479–1493. https://doi.org/10.1016/j.gsf.2018.04.001

East of Jatobá Basin
Apatite fission-track (Dpar)

North of Jatobá Basin
Apatite fission-track (Dpar)

LLM-45A (n=36)
Central age = 106.6 ± 8.2 (1σ)
Dispersion = 38.5%
P(X²) = 0

Peak 1: 56.1 ± 6.4 (24%)
Peak 2: 131.3 ± 7.0 (76%)

LLM-45A (n=34)
MTL = 12.34 µm
σ = 1.87 µm

LLM-47 (n=32)
Central age = 199.4 ± 13.3 (1σ)
Dispersion = 25.7%
P(X²) = 0

Peak 1: 111.7± 15.5 (22%)
Peak 2: 244.7 ± 12.7 (78%)

LLM-47 (n=44)
MTL = 12.23 µm
σ = 1.69 µm

LLM-49 (n=39)
Central age = 109.7 ± 9.3 (1σ)
Dispersion = 46.6%
P(X²) = 0

Peak 1: 49.1 ± 6.4 (19%)
Peak 2: 112.3 ± 8.9 (59%)
Peak 3: 209.1 ± 22.0 (22%)

LLM-49 (n=65)
MTL = 12.67 µm
σ = 1.32 µm

NE-96 (n=40)
Central age = 121.1 ± 9.7 (1σ)
Dispersion = 38.2%
P(X²) = 0

Peak 1: 50.8 ± 16.5 (14%)
Peak 2: 139.6 ± 8.8 (86%)

South of Jatobá Basin
Apatite fission-track (Dpar)

LLM-55 (n=39)
Central age = 125.1 ± 8.4 (1σ)
Dispersion = 35.5%
P(X²) = 0

Peak 1: 58.3 ± 5.2 (18%)
Peak 2: 149.1 ± 5.9 (82%)

LLM-55 (n=38)
MTL = 12.09 μm
σ = 1.60 μm

LLM-53C (n=40)
Central age = 174.4 ± 8.8 (1σ)
Dispersion = 18.1%
P(X²) = 0.02

Peak 1: 174.4 ± 6.9 (100%)

LLM-53C (n=25)
MTL = 10.82 μm
σ = 1.71 μm

LLM-59 (n=39)
Central age = 144.2 ± 9.3 (1σ)
Dispersion = 21.0%
P(X²) = 0.11

Peak 1: 146.6 ± 8.0 (100%)

West of Pernambuco shear zone
Apatite fission-track (Dpar)
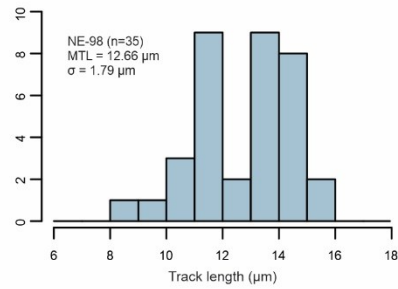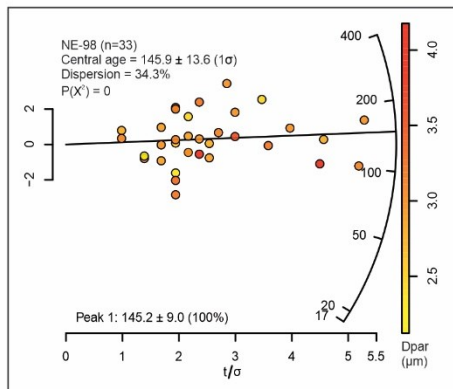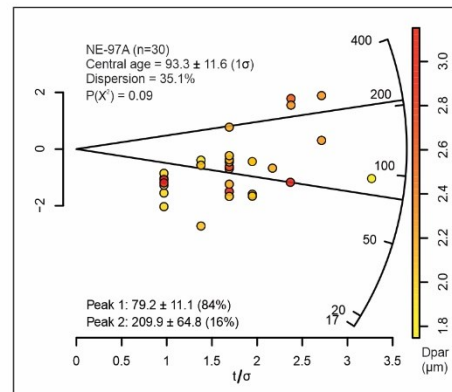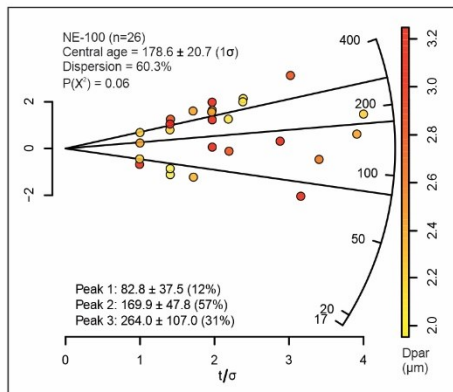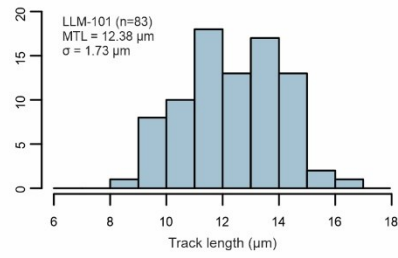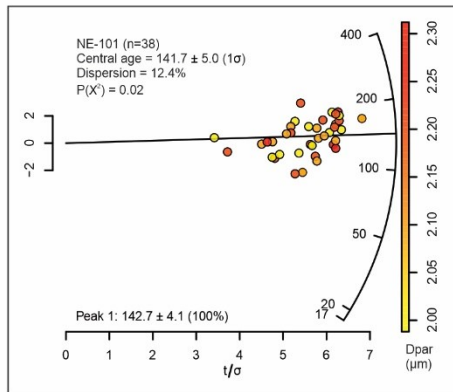
Apatite fission-track results

n: Grains.

Ns: Counted tracks.

ρ(s): Track density in the sample.

U-UNK: ^{238}U content in the sample.

P(X^2) is the chi-squared probability test that dated single-grains belong to the same statistical population (samples fails the test if values are < 0.05).

Area: Counted area.

The zeta value (ζ) of the standard Durango apatite (Dur-2) used was a mean of all analytic sessions: 1.810 x 10^3.

The track density [ρ(STD)] of the standard Durango apatite (Dur-2) used was a mean of all analytic sessions: 1.51 x 10^5.

The ^{238}U content used for the Durango apatite (Dur-2) to determine the zeta value was 8.62 ± 1.5% ppm.

The matrix-matched reference material used to calculate the ^{238}U content of unknown samples and Dur-2 was the Mud Tank standard (MT-7) (6.9 ± 1% ppm; Soares et al., 2015).

References

Soares, C. J., Mertz-Kraus, R., Guedes, S., Stockli, D. F., & Zack, T. (2015). Characterisation of apatites as potential uranium reference materials for fission-track dating by LA-ICP-MS. *Geostandards and Geoanalytical Research*, *39(3),* 305-313.

Sample	n	Ns	ρ (s) ×10^6	^{238}U-UNK (ppm)	Pooled Age Ma	Central Age Ma	P1 Ma	Fraction (P1) %	P2 Ma	Fraction (P2) %	P3 Ma	Fraction (P3) %	P(X^2)	Dispersion %
NE-07D	13	116	0.99	25.67	69.5±6.7	80.4±14.3	25.9±7.5	18	106.8±11.6	82	X	X	0.00	51.7
LLM-49	39	856	1.37	24.76	99.5±4.4	109.7±9.3	49.1±6.4	19	112.3±8.9	59	209.1±22.0	22	0.00	46.6
LLM-55	39	1087	1.74	26.87	116.3±4.8	125.1±8.4	58.3±5.2	18	149.1±5.9	82	X	X	0.00	35.5
NE-06A	39	643	1.18	19.39	104.1±5.0	108.0±12.4	30.1±5.2	18	123.8±9.7	65	241.6±38.0	17	0.00	63.7
NE-15A	40	946	1.48	21.23	124.8±5.3	133.0±9.0	74.5±7.4	26	163.2±7.8	74	X	X	0.00	35.7
NE-96	40	470	0.75	12.27	112.4±6.1	121.1±9.7	50.8±16.5	14.0	139.6±8.8	86	X	X	0.00	38.2
LLM-53C	40	806	1.26	13.51	166.6±7.4	174.4±8.8	174.4±6.9	100	X	X	X	X	0.02	18.1
NE-14A	39	1567	2.54	32.74	138.2±5.2	141.6±4.8	141.4±4.3	100	X	X	X	X	0.08	9.6
NE-101	38	1933	3.27	41.85	140.9±5.0	141.6±5.0	142.7±4.1	100	X	X	X	X	0.02	12.4
LLM-59	39	374	0.60	7.82	137.3±8.0	144.2±9.3	146.6±8.0	100	X	X	X	X	0.11	21.0
NE-97A	30	105	0.22	5.08	81.9±8.3	93.3±11.6	79.2±11.1	84	209.9±64.8	16	X	X	0.09	35.1
NE-98	33	306	0.59	8.17	128.8±8.2	145.9±13.6	145.9±13.6	100	X	X	X	X	0.00	55.1
NE-100	26	142	0.34	4.05	150.8±13.3	178.6±20.7	82.8±37.5	12	169.9±47.8	57	264.0±107.0	31	0.06	60.3
LLM-47	32	662	1.46	13.29	194.7±9.3	199.4±13.3	108.2±15.9	20	228.9±12.3	80	X	X	0.00	25.7
LLM-45A	36	722	1.25	22.76	98.9±4.6	106.6±8.2	56.1±6.4	24	131.3±7.0	76	X	X	0.00	38.5

	Ns	Area (cm²)	ρs	U (ppm)	±1σ (ppm)	Age (Ma)	±1σ (Ma)	Dpar (um)
NE-07D	14	9.00E-06	1.56E+06	15.22	0.23	182.4	52.2	2.9
	9	9.00E-06	1.00E+06	19.17	0.29	93.7	32.7	2.6
	13	9.00E-06	1.44E+06	22.97	0.34	112.8	33.3	2.0
	5	9.00E-06	5.56E+05	48.01	0.72	20.9	9.6	2.0
	5	9.00E-06	5.56E+05	10.40	0.16	95.9	44.0	2.1
	8	9.00E-06	8.89E+05	20.41	0.31	78.4	28.8	3.0
	8	9.00E-06	8.89E+05	23.56	0.35	67.9	25.0	2.2
	2	9.00E-06	2.22E+05	10.50	0.16	38.2	27.3	2.1
	5	9.00E-06	5.56E+05	5.753	0.09	172.5	79.1	2.2
	11	9.00E-06	1.22E+06	83.00	1.24	26.6	8.5	2.1
	11	9.00E-06	1.22E+06	36.68	0.55	60.0	19.1	2.0
	18	9.00E-06	2.00E+06	24.37	0.37	146.9	37.7	2.1
	7	9.00E-06	7.78E+05	13.62	0.20	102.6	40.2	2.6
	Ns	Area (cm²)	ρs	U (ppm)	±1σ (ppm)	Age (Ma)	±1σ (Ma)	Dpar (um)
LLM-49	35	1.60E-05	2.19E+06	106.3	1.60	37.1	7.3	2.1
	21	1.60E-05	1.31E+06	21.00	0.32	112.1	27.0	2.0
	26	1.60E-05	1.63E+06	65.08	0.98	45.0	10.0	2.3
	15	1.60E-05	9.38E+05	50.36	0.76	33.6	9.3	2.2
	17	1.60E-05	1.06E+06	34.09	0.51	56.2	14.8	2.2
	12	1.60E-05	7.50E+05	14.86	0.22	90.7	27.8	2.1
	30	1.60E-05	1.88E+06	25.06	0.38	134.0	28.0	2.1

Ns	Area (cm²)	ρs	U (ppm)	±1σ (ppm)	Age (Ma)	±1σ (Ma)	Dpar (um)
16	1.60E-05	1.00E+06	36.65	0.55	49.2	13.3	2.2
17	1.60E-05	1.06E+06	8.925	0.13	212.0	55.8	2.0
6	1.60E-05	3.75E+05	6.672	0.10	100.9	42.5	2.3
19	1.60E-05	1.19E+06	16.98	0.25	125.4	31.5	2.2
11	1.60E-05	6.88E+05	8.146	0.12	151.0	48.1	2.5
4	1.60E-05	2.50E+05	6.406	0.10	70.3	35.8	2.1
6	1.60E-05	3.75E+05	6.250	0.09	107.7	45.3	2.2
25	1.60E-05	1.56E+06	17.25	0.26	161.9	36.3	2.1
21	1.60E-05	1.31E+06	36.19	0.54	65.3	15.7	2.3
17	1.60E-05	1.06E+06	23.55	0.35	81.1	21.3	2.2
37	1.60E-05	2.31E+06	48.11	0.72	86.4	16.7	2.2
16	1.60E-05	1.00E+06	12.32	0.18	145.2	39.2	2.3
46	1.60E-05	2.88E+06	24.70	0.37	207.3	37.2	2.1
13	1.60E-05	8.13E+05	17.18	0.26	85.0	25.1	2.4
21	1.60E-05	1.31E+06	36.97	0.55	63.9	15.4	2.8
12	1.60E-05	7.50E+05	16.82	0.25	80.2	24.6	2.7
21	1.60E-05	1.31E+06	17.85	0.27	131.7	31.7	2.2
25	1.60E-05	1.56E+06	31.34	0.47	89.6	20.1	2.2
32	1.60E-05	2.00E+06	12.19	0.18	290.3	59.2	2.1
23	1.60E-05	1.44E+06	16.01	0.24	160.5	37.2	2.3
28	1.60E-05	1.75E+06	21.78	0.33	143.8	30.9	2.1
26	1.60E-05	1.63E+06	14.25	0.21	203.2	44.9	2.8
13	1.60E-05	8.13E+05	20.19	0.30	72.4	21.4	3.0
20	1.60E-05	1.25E+06	27.26	0.41	82.5	20.3	2.6
48	1.60E-05	3.00E+06	25.34	0.38	210.8	37.2	2.6
38	1.60E-05	2.38E+06	33.63	0.50	126.6	24.3	2.1
19	1.60E-05	1.19E+06	18.66	0.28	114.2	28.7	2.3
26	1.60E-05	1.63E+06	22.83	0.34	127.6	28.2	2.2
19	1.60E-05	1.19E+06	15.03	0.23	141.4	35.5	2.2
20	1.60E-05	1.25E+06	11.64	0.17	191.5	47.1	2.5
30	1.60E-05	1.88E+06	27.53	0.41	122.1	25.5	2.1
25	1.60E-05	1.56E+06	10.21	0.15	271.1	60.9	2.1

	Ns	Area (cm²)	ρs	U (ppm)	±1σ (ppm)	Age (Ma)	±1σ (Ma)	Dpar (um)
LLM-55	30	1.60E-05	1.88E+06	27.69	0.42	121.4	25.4	2.1
	37	1.60E-05	2.31E+06	53.71	0.81	77.5	15.0	2.0
	13	1.60E-05	8.13E+05	9.315	0.14	156.0	46.1	2.1
	28	1.60E-05	1.75E+06	22.01	0.33	142.4	30.6	2.0
	27	1.60E-05	1.69E+06	25.41	0.38	119.1	25.9	2.1
	36	1.60E-05	2.25E+06	26.89	0.40	149.7	29.2	2.2
	42	1.60E-05	2.63E+06	21.21	0.32	220.2	40.7	2.0
	29	1.60E-05	1.81E+06	18.28	0.27	177.0	37.5	1.9
	29	1.60E-05	1.81E+06	21.59	0.32	150.2	31.8	2.0
	30	1.60E-05	1.88E+06	28.88	0.43	116.5	24.4	2.1
	27	1.60E-05	1.69E+06	56.59	0.85	53.8	11.7	2.0
	38	1.60E-05	2.38E+06	98.32	1.47	43.6	8.3	2.1
	20	1.60E-05	1.25E+06	13.65	0.20	163.6	40.2	2.1
	22	1.60E-05	1.38E+06	16.06	0.24	153.1	36.2	2.0
	20	1.60E-05	1.25E+06	25.06	0.38	89.7	22.0	2.1
	21	1.60E-05	1.31E+06	14.57	0.22	161.0	38.8	2.2
	37	1.60E-05	2.31E+06	30.32	0.45	136.6	26.4	2.1
	26	1.60E-05	1.63E+06	22.85	0.34	127.5	28.2	2.2
	29	1.60E-05	1.81E+06	21.69	0.33	149.5	31.7	2.2
	15	1.60E-05	9.38E+05	16.59	0.25	101.5	28.2	2.0
	28	1.60E-05	1.75E+06	54.73	0.82	57.6	12.4	1.8
	26	1.60E-05	1.63E+06	16.86	0.25	172.2	38.1	2.0
	15	1.60E-05	9.38E+05	23.08	0.35	73.1	20.3	2.1
	16	1.60E-05	1.00E+06	14.09	0.21	127.2	34.4	1.9
	23	1.60E-05	1.44E+06	20.20	0.30	127.6	29.6	2.0
	19	1.60E-05	1.19E+06	31.81	0.48	67.2	16.9	2.1
	20	1.60E-05	1.25E+06	19.28	0.29	116.3	28.6	2.1
	41	1.60E-05	2.56E+06	40.97	0.61	112.2	20.9	2.0
	33	1.60E-05	2.06E+06	20.33	0.30	181.1	36.5	2.0
	29	1.60E-05	1.81E+06	23.76	0.36	136.6	28.9	2.1
	47	1.60E-05	2.94E+06	26.31	0.39	199.0	35.4	2.0
	26	1.60E-05	1.63E+06	20.46	0.31	142.2	31.4	2.0
	35	1.60E-05	2.19E+06	17.70	0.27	219.9	43.4	2.1
	14	1.60E-05	8.75E+05	7.232	0.11	215.4	61.6	2.2
	38	1.60E-05	2.38E+06	31.64	0.47	134.5	25.8	2.3
	9	1.60E-05	5.63E+05	31.53	0.47	32.2	11.2	2.1
	35	1.60E-05	2.19E+06	21.32	0.32	183.1	36.1	2.1
	37	1.60E-05	2.31E+06	22.80	0.34	181.0	35.0	2.2
	40	1.60E-05	2.50E+06	33.32	0.50	134.4	25.3	2.3

	Ns	Area (cm²)	ρs	U (ppm)	±1σ (ppm)	Age (Ma)	±1σ (Ma)	Dpar (um)
NE-06A	33	1.60E-05	2.06E+06	18.45	0.28	199.2	40.2	2.1
	5	1.60E-05	3.13E+05	7.971	0.12	70.6	32.4	1.8
	8	1.60E-05	5.00E+05	4.425	0.07	201.4	74.1	2.0
	17	1.60E-05	1.06E+06	13.73	0.21	138.6	36.5	2.1
	10	1.60E-05	6.25E+05	16.83	0.25	66.9	22.2	2.0
	73	1.60E-05	4.56E+06	59.89	0.90	136.4	21.2	2.2
	8	1.60E-05	5.00E+05	4.539	0.07	196.4	72.3	2.1
	21	1.60E-05	1.31E+06	14.27	0.21	164.3	39.6	2.2

	Ns	Area (cm²)	ρs	U (ppm)	±1σ (ppm)	Age (Ma)	±1σ (Ma)	Dpar (um)
	6	1.60E-05	3.75E+05	27.78	0.42	24.4	10.3	1.9
	2	1.60E-05	1.25E+05	6.661	0.10	33.9	24.2	1.8
	7	1.60E-05	4.38E+05	59.35	0.89	13.3	5.2	1.7
	27	9.00E-06	3.00E+06	13.95	0.21	378.0	82.3	1.9
	30	1.60E-05	1.88E+06	39.11	0.59	86.2	18.0	1.8
	8	9.00E-06	8.89E+05	3.449	0.05	450.4	165.7	2.1
	11	1.60E-05	6.88E+05	32.03	0.48	38.7	12.3	2.1
	4	1.60E-05	2.50E+05	6.946	0.10	64.8	33.1	2.0
	17	1.60E-05	1.06E+06	25.00	0.37	76.5	20.1	1.9
	8	9.00E-06	8.89E+05	13.03	0.20	122.3	45.0	2.0
	19	1.60E-05	1.19E+06	13.69	0.21	155.1	38.9	2.0
	26	9.00E-06	2.89E+06	36.55	0.55	141.5	31.3	2.1
	22	1.60E-05	1.38E+06	13.30	0.20	184.4	43.6	2.2
	25	9.00E-06	2.78E+06	28.39	0.43	174.7	39.2	2.0
	7	1.60E-05	4.38E+05	7.803	0.12	100.7	39.4	1.7
	13	1.60E-05	8.13E+05	11.76	0.18	123.9	36.6	1.8
	4	1.60E-05	2.50E+05	5.317	0.08	84.5	43.1	1.8
	10	1.60E-05	6.25E+05	10.74	0.16	104.5	34.7	2.0
	9	1.60E-05	5.63E+05	7.350	0.11	137.0	47.8	2.1
	6	9.00E-06	6.67E+05	24.42	0.37	49.2	20.7	2.0
	10	9.00E-06	1.11E+06	14.63	0.22	136.0	45.2	1.9
	4	1.60E-05	2.50E+05	8.384	0.13	53.7	27.4	2.2
	40	1.60E-05	2.50E+06	31.98	0.48	140.0	26.3	2.1
	50	1.60E-05	3.13E+06	23.87	0.36	232.7	40.6	2.2
	11	1.60E-05	6.88E+05	42.67	0.64	29.1	9.3	1.9
	7	1.60E-05	4.38E+05	25.88	0.39	30.5	11.9	1.9
	18	1.60E-05	1.13E+06	8.790	0.13	227.6	58.4	2.0
	4	9.00E-06	4.44E+05	4.409	0.07	179.9	91.8	1.7
	19	1.60E-05	1.19E+06	21.81	0.33	97.8	24.6	1.8
	40	1.60E-05	2.50E+06	41.98	0.63	106.9	20.1	1.7
	4	9.00E-06	4.44E+05	5.069	0.08	156.8	80.0	2.1
	Ns	Area (cm²)	ρs	U (ppm)	±1σ (ppm)	Age (Ma)	±1σ (Ma)	Dpar (um)
NE-15A	38	1.60E-05	2.38E+06	24.52	0.37	173.0	33.1	2.1
	46	1.60E-05	2.88E+06	62.62	0.94	82.6	14.8	2.1
	20	1.60E-05	1.25E+06	14.24	0.21	157.0	38.6	1.9
	39	1.60E-05	2.44E+06	30.51	0.46	143.0	27.2	2.0
	28	1.60E-05	1.75E+06	19.37	0.29	161.5	34.7	2.1
	10	1.60E-05	6.25E+05	6.571	0.10	169.9	56.5	2.0
	19	1.60E-05	1.19E+06	37.32	0.56	57.3	14.4	2.1
	22	1.60E-05	1.38E+06	20.64	0.31	119.4	28.2	2.0
	27	1.60E-05	1.69E+06	43.45	0.65	69.9	15.2	2.1
	40	1.60E-05	2.50E+06	24.57	0.37	181.6	34.2	2.3
	28	1.60E-05	1.75E+06	21.11	0.32	148.3	31.9	2.1
	19	1.60E-05	1.19E+06	10.41	0.16	203.2	51.0	2.2
	17	1.60E-05	1.06E+06	10.78	0.16	176.0	46.3	2.1
	23	1.60E-05	1.44E+06	16.20	0.24	158.6	36.8	2.1
	42	1.60E-05	2.63E+06	22.61	0.34	206.8	38.2	2.2
	27	1.60E-05	1.69E+06	24.27	0.36	124.6	27.1	2.2
	29	1.60E-05	1.81E+06	32.35	0.49	100.6	21.3	2.1
	25	1.60E-05	1.56E+06	20.72	0.31	135.0	30.3	2.3
	19	1.60E-05	1.19E+06	6.575	0.10	318.9	80.1	2.6
	29	1.60E-05	1.81E+06	18.88	0.28	171.4	36.3	2.1
	16	1.60E-05	1.00E+06	14.83	0.22	120.9	32.6	2.1
	19	1.60E-05	1.19E+06	24.80	0.37	86.1	21.6	2.0
	19	1.60E-05	1.19E+06	13.66	0.20	155.4	39.0	2.1
	16	1.60E-05	1.00E+06	18.90	0.28	95.1	25.7	2.0
	33	1.60E-05	2.06E+06	13.52	0.20	270.5	54.6	1.9
	22	1.60E-05	1.38E+06	20.15	0.30	122.3	28.9	2.0
	15	1.60E-05	9.38E+05	12.97	0.19	129.6	36.0	1.9
	27	1.60E-05	1.69E+06	22.61	0.34	133.7	29.1	2.1
	44	1.60E-05	2.75E+06	26.21	0.39	187.2	34.1	2.0
	17	1.60E-05	1.06E+06	11.56	0.17	164.3	43.2	2.0
	11	1.60E-05	6.88E+05	16.47	0.25	75.1	23.9	2.0
	24	1.60E-05	1.50E+06	9.460	0.14	280.8	64.1	2.1
	23	1.60E-05	1.44E+06	62.91	0.94	41.2	9.6	1.9
	25	1.60E-05	1.56E+06	20.76	0.31	134.8	30.3	2.2
	19	1.60E-05	1.19E+06	12.07	0.18	175.7	44.1	2.1
	21	1.60E-05	1.31E+06	15.16	0.23	154.8	37.3	2.0
	16	1.60E-05	1.00E+06	21.48	0.32	83.7	22.6	2.0
	10	1.60E-05	6.25E+05	17.70	0.27	63.6	21.1	2.2
	10	1.60E-05	6.25E+05	15.10	0.23	74.5	24.8	2.1
	12	1.60E-05	7.50E+05	11.12	0.17	121.0	37.0	2.1
	Ns	Area (cm²)	ρs	U (ppm)	±1σ (ppm)	Age (Ma)	±1σ (Ma)	Dpar (um)
NE-96	13	1.60E-05	8.13E+05	18.42	0.28	79.3	23.4	2.2
	9	9.00E-06	1.00E+06	50.33	0.75	35.9	12.5	2.1
	18	1.60E-05	1.13E+06	14.19	0.21	141.9	36.4	2.1
	23	1.60E-05	1.44E+06	7.857	0.12	322.9	75.0	1.9
	12	1.60E-05	7.50E+05	3.789	0.06	348.7	106.8	2.0
	5	1.60E-05	3.13E+05	14.79	0.22	38.1	17.5	2.1
	11	1.60E-05	6.88E+05	10.11	0.15	122.0	38.8	2.1
	7	1.60E-05	4.38E+05	3.821	0.06	204.0	79.8	1.9

Ns	Area (cm²)	ρs	U (ppm)	±1σ (ppm)	Age (Ma)	±1σ (Ma)	Dpar (um)
9	1.60E-05	5.63E+05	7.079	0.11	142.2	49.6	2.0
6	1.60E-05	3.75E+05	4.200	0.06	159.6	67.2	2.1
15	1.60E-05	9.38E+05	15.98	0.24	105.3	29.2	2.1
20	1.60E-05	1.25E+06	20.10	0.30	111.6	27.4	2.0
13	1.60E-05	8.13E+05	9.786	0.15	148.6	43.9	2.2
5	1.60E-05	3.13E+05	4.262	0.06	131.4	60.3	2.1
4	1.60E-05	2.50E+05	15.34	0.23	29.4	15.0	2.0
4	1.60E-05	2.50E+05	4.541	0.07	98.9	50.5	2.2
9	1.60E-05	5.63E+05	5.874	0.09	171.0	59.6	2.0
10	1.60E-05	6.25E+05	4.767	0.07	233.0	77.4	2.1
3	1.60E-05	1.88E+05	6.089	0.09	55.5	32.5	2.0
15	1.60E-05	9.38E+05	19.54	0.29	86.3	23.9	1.9
14	1.60E-05	8.75E+05	23.98	0.36	65.7	18.8	2.0
11	1.60E-05	6.88E+05	6.842	0.10	179.3	57.1	2.1
17	1.60E-05	1.06E+06	12.89	0.19	147.5	38.8	2.0
10	1.60E-05	6.25E+05	13.06	0.20	86.1	28.6	2.3
22	1.60E-05	1.38E+06	23.05	0.35	107.1	25.3	2.0
30	1.60E-05	1.88E+06	23.74	0.36	141.4	29.6	2.1
9	1.60E-05	5.63E+05	10.12	0.15	99.9	34.8	2.0
16	1.60E-05	1.00E+06	16.01	0.24	112.1	30.3	1.9
11	1.60E-05	6.88E+05	7.834	0.12	156.9	49.9	2.1
13	1.60E-05	8.13E+05	11.55	0.17	126.1	37.3	2.2
27	1.60E-05	1.69E+06	19.83	0.30	152.2	33.1	2.0
8	1.60E-05	5.00E+05	9.767	0.15	92.0	33.9	2.1
10	1.60E-05	6.25E+05	3.449	0.05	319.9	106.3	1.9
7	1.60E-05	4.38E+05	18.36	0.28	43.0	16.8	2.0
6	1.60E-05	3.75E+05	4.823	0.07	139.2	58.6	2.0
8	1.60E-05	5.00E+05	8.172	0.12	109.8	40.4	1.9
5	1.60E-05	3.13E+05	3.998	0.06	139.9	64.2	2.5
7	1.60E-05	4.38E+05	7.837	0.12	100.3	39.2	2.1
10	1.60E-05	6.25E+05	11.18	0.17	100.4	33.3	1.9
18	1.60E-05	1.13E+06	13.37	0.20	150.5	38.6	2.1

	Ns	Area (cm²)	ρs	U (ppm)	±1σ (ppm)	Age (Ma)	±1σ (Ma)	Dpar (um)
LLM-53C	5	1.60E-05	3.13E+05	2.266	0.03	244.9	112.4	2.0
	12	1.60E-05	7.50E+05	5.010	0.08	265.4	81.3	2.1
	10	1.60E-05	6.25E+05	10.29	0.15	109.0	36.2	2.0
	9	1.60E-05	5.63E+05	7.605	0.11	132.5	46.2	1.9
	10	1.60E-05	6.25E+05	5.469	0.08	203.6	67.6	2.1
	12	1.60E-05	7.50E+05	5.859	0.09	227.6	69.7	2.2
	17	1.60E-05	1.06E+06	7.897	0.12	239.0	62.9	2.0
	28	1.60E-05	1.75E+06	22.22	0.33	141.0	30.3	2.1
	13	1.60E-05	8.13E+05	8.726	0.13	166.4	49.2	2.0
	8	1.60E-05	5.00E+05	6.812	0.10	131.5	48.4	2.2
	20	1.60E-05	1.25E+06	6.418	0.10	343.2	84.4	2.0
	9	1.60E-05	5.63E+05	3.988	0.06	250.4	87.3	2.3
	19	1.60E-05	1.19E+06	10.56	0.16	200.3	50.3	2.1
	13	1.60E-05	8.13E+05	8.801	0.13	165.0	48.7	2.2
	11	1.60E-05	6.88E+05	8.424	0.13	146.0	46.5	2.1
	23	1.60E-05	1.44E+06	13.94	0.21	184.0	42.7	2.1
	20	1.60E-05	1.25E+06	19.73	0.30	113.7	27.9	2.4
	26	1.60E-05	1.63E+06	22.01	0.33	132.3	29.2	2.2
	10	1.60E-05	6.25E+05	8.494	0.13	131.8	43.8	2.1
	29	1.60E-05	1.81E+06	13.65	0.20	235.9	50.0	2.2
	8	1.60E-05	5.00E+05	3.980	0.06	223.5	82.2	2.1
	34	1.60E-05	2.13E+06	24.80	0.37	153.2	30.6	1.9
	22	1.60E-05	1.38E+06	11.97	0.18	204.7	48.4	2.1
	13	1.60E-05	8.13E+05	5.981	0.09	241.3	71.3	2.1
	22	1.60E-05	1.38E+06	17.34	0.26	142.0	33.5	2.2
	81	1.60E-05	5.06E+06	58.02	0.87	156.0	23.5	2.0
	9	1.60E-05	5.63E+05	7.300	0.11	138.0	48.1	1.9
	45	1.60E-05	2.81E+06	18.16	0.27	274.3	49.6	2.1
	38	1.60E-05	2.38E+06	38.99	0.58	109.3	20.9	2.0
	13	1.60E-05	8.13E+05	10.19	0.15	142.7	42.2	2.1
	34	1.60E-05	2.13E+06	21.71	0.33	174.8	34.9	2.2
	16	1.60E-05	1.00E+06	9.875	0.15	180.7	48.8	2.0
	34	1.60E-05	2.13E+06	12.89	0.19	291.6	58.2	2.2
	23	1.60E-05	1.44E+06	22.00	0.33	117.2	27.2	2.0
	15	1.60E-05	9.38E+05	7.657	0.11	217.9	60.5	2.1
	12	1.60E-05	7.50E+05	5.979	0.09	223.1	68.3	2.1
	28	1.60E-05	1.75E+06	22.28	0.33	140.6	30.2	2.3
	33	1.60E-05	2.06E+06	21.94	0.33	168.0	33.9	2.1
	5	1.60E-05	3.13E+05	7.621	0.11	73.8	33.8	2.0
	17	1.60E-05	1.06E+06	13.46	0.20	141.3	37.2	2.0

	Ns	Area (cm²)	ρs	U (ppm)	±1σ (ppm)	Age (Ma)	±1σ (Ma)	Dpar (um)
NE-14A	34	1.60E-05	2.13E+06	37.05	0.56	103.0	20.5	2.3
	73	1.60E-05	4.56E+06	46.02	0.69	177.0	27.5	2.1
	44	1.60E-05	2.75E+06	25.99	0.39	188.7	34.3	1.9
	42	1.60E-05	2.63E+06	42.21	0.63	111.6	20.6	2.1
	56	1.60E-05	3.50E+06	43.74	0.66	143.2	24.1	2.2
	16	1.60E-05	1.00E+06	8.076	0.12	220.3	59.5	2.2
	49	1.60E-05	3.06E+06	40.09	0.60	136.8	24.0	2.1

	Ns	Area (cm²)	ρs	U (ppm)	±1σ (ppm)	Age (Ma)	±1σ (Ma)	Dpar (um)
	36	1.60E-05	2.25E+06	22.07	0.33	181.9	35.5	2.1
	29	1.60E-05	1.81E+06	22.34	0.34	145.2	30.8	1.9
	70	1.60E-05	4.38E+06	66.66	1.00	117.7	18.5	2.1
	59	1.60E-05	3.69E+06	47.63	0.71	138.6	22.9	2.2
	45	1.60E-05	2.81E+06	41.32	0.62	122.1	22.0	2.0
	30	1.60E-05	1.88E+06	18.09	0.27	185.0	38.7	2.3
	49	1.60E-05	3.06E+06	55.35	0.83	99.4	17.4	2.2
	37	1.60E-05	2.31E+06	26.65	0.40	155.2	30.0	2.0
	53	1.60E-05	3.31E+06	34.86	0.52	169.8	29.0	2.1
	19	1.60E-05	1.19E+06	13.58	0.20	156.3	39.3	2.1
	27	9.00E-06	3.00E+06	18.01	0.27	294.6	64.2	2.3
	38	1.60E-05	2.38E+06	38.69	0.58	110.2	21.1	2.1
	36	1.60E-05	2.25E+06	34.57	0.52	116.8	22.8	2.1
	23	1.60E-05	1.44E+06	18.57	0.28	138.6	32.2	2.3
	52	1.60E-05	3.25E+06	51.81	0.78	112.5	19.4	2.3
	30	1.60E-05	1.88E+06	23.80	0.36	141.1	29.5	2.2
	38	1.60E-05	2.38E+06	26.63	0.40	159.4	30.6	2.4
	49	1.60E-05	3.06E+06	44.11	0.66	124.5	21.8	2.2
	20	1.60E-05	1.25E+06	17.27	0.26	129.7	31.9	2.6
	47	1.60E-05	2.94E+06	40.80	0.61	129.0	23.0	2.2
	37	1.60E-05	2.31E+06	27.98	0.42	147.9	28.6	2.1
	16	1.60E-05	1.00E+06	18.84	0.28	95.4	25.8	2.2
	51	1.60E-05	3.19E+06	32.54	0.49	174.9	30.3	2.4
	33	1.60E-05	2.06E+06	36.32	0.54	102.0	20.6	2.3
	39	1.60E-05	2.44E+06	27.92	0.42	156.1	29.6	2.1
	26	1.60E-05	1.63E+06	21.62	0.32	134.6	29.8	2.0
	39	1.60E-05	2.44E+06	30.85	0.46	141.4	26.9	2.1
	45	1.60E-05	2.81E+06	36.87	0.55	136.6	24.7	2.0
	51	1.60E-05	3.19E+06	30.39	0.46	187.1	32.4	2.1
	45	1.60E-05	2.81E+06	35.26	0.53	142.8	25.8	2.1
	30	1.60E-05	1.88E+06	21.00	0.32	159.6	33.4	2.0
	54	1.60E-05	3.38E+06	51.25	0.77	118.1	20.1	2.3
	Ns	**Area (cm²)**	**ρs**	**U (ppm)**	**±1σ (ppm)**	**Age (Ma)**	**±1σ (Ma)**	**Dpar (um)**
NE-101	45	1.60E-05	2.81E+06	57.18	0.86	88.4	16.0	2.1
	95	1.60E-05	5.94E+06	62.76	0.94	169.0	24.4	2.1
	41	1.60E-05	2.56E+06	26.04	0.39	175.7	32.8	2.0
	68	1.60E-05	4.25E+06	46.73	0.70	162.5	25.8	2.1
	39	1.60E-05	2.44E+06	26.56	0.40	164.0	31.1	2.1
	63	1.60E-05	3.94E+06	47.72	0.72	147.6	23.9	2.0
	71	1.60E-05	4.44E+06	46.86	0.70	169.2	26.5	2.2
	54	1.60E-05	3.38E+06	43.62	0.65	138.5	23.6	2.1
	65	1.60E-05	4.06E+06	38.63	0.58	187.6	30.1	2.0
	14	9.00E-06	1.56E+06	19.46	0.29	143.1	40.9	2.0
	49	1.60E-05	3.06E+06	43.09	0.65	127.4	22.4	2.2
	66	1.60E-05	4.13E+06	57.64	0.86	128.2	20.5	2.3
	32	1.60E-05	2.00E+06	34.86	0.52	103.0	21.0	2.2
	70	1.60E-05	4.38E+06	41.67	0.63	187.3	29.4	2.3
	41	1.60E-05	2.56E+06	54.07	0.81	85.2	15.9	2.2
	71	1.60E-05	4.44E+06	44.09	0.66	179.6	28.1	2.0
	58	1.60E-05	3.63E+06	37.72	0.57	171.6	28.5	2.2
	68	1.60E-05	4.25E+06	61.96	0.93	123.0	19.5	2.3
	39	1.60E-05	2.44E+06	29.06	0.44	150.0	28.5	2.2
	73	1.60E-05	4.56E+06	53.41	0.80	152.8	23.7	2.0
	59	1.60E-05	3.69E+06	46.65	0.70	141.5	23.4	2.1
	67	1.60E-05	4.19E+06	47.62	0.71	157.2	25.0	2.2
	68	1.60E-05	4.25E+06	41.40	0.62	183.2	29.0	2.2
	50	1.60E-05	3.13E+06	44.52	0.67	125.8	21.9	2.0
	31	1.60E-05	1.94E+06	26.04	0.39	133.3	27.5	2.1
	31	1.60E-05	1.94E+06	33.41	0.50	104.1	21.5	2.0
	43	9.00E-06	4.78E+06	75.42	1.13	113.7	20.9	2.0
	27	1.60E-05	1.69E+06	23.78	0.36	127.2	27.7	2.1
	68	1.60E-05	4.25E+06	56.62	0.85	134.4	21.3	2.1
	44	1.60E-05	2.75E+06	21.99	0.33	222.5	40.5	2.2
	48	1.60E-05	3.00E+06	33.44	0.50	160.3	28.3	2.0
	34	1.60E-05	2.13E+06	34.71	0.52	109.9	21.9	2.0
	53	1.60E-05	3.31E+06	37.71	0.57	157.1	26.9	2.1
	52	1.60E-05	3.25E+06	52.97	0.79	110.1	19.0	2.2
	29	1.60E-05	1.81E+06	24.58	0.37	132.1	28.0	2.3
	17	9.00E-06	1.89E+06	30.93	0.46	109.6	28.8	2.2
	53	1.60E-05	3.31E+06	57.22	0.86	103.9	17.8	2.1
	37	1.60E-05	2.31E+06	27.99	0.42	147.9	28.6	2.1
	Ns	**Area (cm²)**	**ρs**	**U (ppm)**	**±1σ (ppm)**	**Age (Ma)**	**±1σ (Ma)**	**Dpar (um)**
LLM-59	7	1.60E-05	4.38E+05	5.735	0.09	136.6	53.5	1.9
	10	1.60E-05	6.25E+05	5.655	0.08	197.0	65.5	2.1
	7	1.60E-05	4.38E+05	4.339	0.07	179.9	70.4	2.0
	8	1.60E-05	5.00E+05	6.723	0.10	133.2	49.0	2.2
	8	1.60E-05	5.00E+05	5.882	0.09	152.1	56.0	2.0
	16	1.60E-05	1.00E+06	6.098	0.09	290.2	78.3	2.1
	9	1.60E-05	5.63E+05	10.00	0.15	101.0	35.2	1.9
	7	1.60E-05	4.38E+05	4.391	0.07	177.9	69.6	2.1
	21	1.60E-05	1.31E+06	9.467	0.14	246.2	59.3	2.1

Ns	Area (cm²)	ρs	U (ppm)	±1σ (ppm)	Age (Ma)	±1σ (Ma)	Dpar (um)
6	1.60E-05	3.75E+05	7.925	0.12	85.1	35.8	2.0
15	1.60E-05	9.38E+05	16.85	0.25	99.9	27.7	2.1
13	1.60E-05	8.13E+05	8.438	0.13	172.0	50.8	2.0
11	1.60E-05	6.88E+05	9.866	0.15	124.9	39.8	2.1
11	1.60E-05	6.88E+05	6.303	0.09	194.5	61.9	2.0
7	1.60E-05	4.38E+05	7.583	0.11	103.6	40.6	2.1
8	1.60E-05	5.00E+05	9.981	0.15	90.0	33.1	2.0
7	1.60E-05	4.38E+05	5.816	0.09	134.7	52.7	2.1
11	1.60E-05	6.88E+05	5.964	0.09	205.3	65.4	2.1
16	1.60E-05	1.00E+06	8.381	0.13	212.4	57.4	2.2
9	1.60E-05	5.63E+05	11.94	0.18	84.7	29.5	2.0
5	1.60E-05	3.13E+05	4.097	0.06	136.6	62.7	2.1
14	1.60E-05	8.75E+05	10.98	0.16	142.6	40.8	2.1
13	1.60E-05	8.13E+05	4.307	0.06	332.7	98.3	2.0
5	1.60E-05	3.13E+05	5.901	0.09	95.1	43.6	2.2
9	1.60E-05	5.63E+05	5.013	0.08	200.0	69.7	2.1
9	1.60E-05	5.63E+05	8.294	0.12	121.6	42.4	2.0
6	1.60E-05	3.75E+05	6.130	0.09	109.8	46.2	2.0
8	1.60E-05	5.00E+05	7.306	0.11	122.7	45.2	2.1
9	1.60E-05	5.63E+05	9.890	0.15	102.1	35.6	2.1
7	1.60E-05	4.38E+05	5.703	0.09	137.4	53.8	2.0
8	1.60E-05	5.00E+05	8.717	0.13	103.0	37.9	2.1
11	1.60E-05	6.88E+05	20.02	0.30	61.9	19.7	2.0
10	1.60E-05	6.25E+05	8.003	0.12	139.8	46.5	2.1
7	1.60E-05	4.38E+05	5.100	0.08	153.4	60.1	2.3
5	1.60E-05	3.13E+05	4.383	0.07	127.8	58.6	2.1
5	1.60E-05	3.13E+05	5.578	0.08	100.6	46.2	2.0
10	1.60E-05	6.25E+05	8.835	0.13	126.8	42.1	2.1
10	1.60E-05	6.25E+05	5.061	0.08	219.7	73.0	2.1
16	1.60E-05	1.00E+06	14.21	0.21	126.1	34.1	2.2

	Ns	Area (cm²)	ρs	U (ppm)	±1σ (ppm)	Age (Ma)	±1σ (Ma)	Dpar (um)
NE-97A	4	1.60E-05	2.50E+05	4.360	0.07	103.0	52.5	2.1
	4	1.60E-05	2.50E+05	7.874	0.12	57.2	29.2	2.0
	3	9.00E-06	3.33E+05	6.928	0.10	86.5	50.7	2.1
	3	1.60E-05	1.88E+05	6.269	0.09	53.9	31.6	2.9
	3	1.60E-05	1.88E+05	3.739	0.06	90.1	52.9	2.8
	6	1.60E-05	3.75E+05	2.443	0.04	272.0	114.5	2.6
	8	1.60E-05	5.00E+05	6.162	0.09	145.2	53.4	2.3
	1	1.60E-05	6.25E+04	4.051	0.06	27.9	28.0	2.0
	6	1.60E-05	3.75E+05	2.699	0.04	246.7	103.8	2.3
	3	1.60E-05	1.88E+05	3.383	0.05	99.5	58.4	2.1
	4	1.60E-05	2.50E+05	8.150	0.12	55.3	28.2	2.1
	8	1.60E-05	5.00E+05	3.435	0.05	258.2	95.0	2.3
	3	1.60E-05	1.88E+05	6.933	0.10	48.8	28.6	2.1
	1	1.60E-05	6.25E+04	2.432	0.04	46.4	46.6	2.2
	12	1.60E-05	7.50E+05	14.22	0.21	94.8	29.0	1.8
	1	1.60E-05	6.25E+04	2.012	0.03	56.0	56.3	2.0
	1	1.60E-05	6.25E+04	3.072	0.05	36.7	36.9	2.0
	6	1.60E-05	3.75E+05	8.469	0.13	79.7	33.5	3.1
	1	1.60E-05	6.25E+04	2.517	0.04	44.8	45.0	2.9
	5	1.60E-05	3.13E+05	5.869	0.09	95.7	43.9	2.2
	3	1.60E-05	1.88E+05	1.638	0.02	203.9	119.5	2.2
	2	1.60E-05	1.25E+05	2.568	0.04	87.5	62.5	2.1
	3	1.60E-05	1.88E+05	3.237	0.05	104.0	61.0	2.2
	1	9.00E-06	1.11E+05	11.71	0.18	17.2	17.2	2.0
	3	1.60E-05	1.88E+05	5.381	0.08	62.8	36.8	2.2
	2	1.60E-05	1.25E+05	12.04	0.18	18.8	13.4	2.1
	3	1.60E-05	1.88E+05	2.972	0.04	113.2	66.4	2.1
	2	1.60E-05	1.25E+05	2.281	0.03	98.4	70.3	1.9
	2	1.60E-05	1.25E+05	2.591	0.04	86.7	62.0	2.1
	1	1.60E-05	6.25E+04	2.827	0.04	39.9	40.1	2.9

	Ns	Area (cm²)	ρs	U (ppm)	±1σ (ppm)	Age (Ma)	±1σ (Ma)	Dpar (um)
NE-98	5	1.60E-05	3.13E+05	5.346	0.08	105.0	48.1	3.0
	4	9.00E-06	4.44E+05	2.130	0.03	367.0	187.3	3.3
	6	1.60E-05	3.75E+05	6.641	0.10	101.4	42.7	4.1
	10	1.60E-05	6.25E+05	7.409	0.11	150.9	50.1	3.5
	19	1.60E-05	1.19E+06	12.88	0.19	164.8	41.4	3.0
	6	1.60E-05	3.75E+05	1.900	0.03	347.7	146.3	3.2
	38	1.60E-05	2.38E+06	41.64	0.62	102.4	19.6	3.1
	2	1.60E-05	1.25E+05	3.064	0.05	73.4	52.4	3.1
	14	1.60E-05	8.75E+05	5.775	0.09	268.6	76.8	2.5
	4	1.60E-05	2.50E+05	8.058	0.12	55.9	28.5	2.4
	2	1.60E-05	1.25E+05	2.777	0.04	81.0	57.8	2.2
	8	1.60E-05	5.00E+05	5.337	0.08	167.4	61.6	3.1
	9	1.60E-05	5.63E+05	2.275	0.03	432.7	150.8	3.0
	5	1.60E-05	3.13E+05	2.094	0.03	264.6	121.3	2.5
	3	1.60E-05	1.88E+05	2.667	0.04	126.0	73.9	3.0
	4	1.60E-05	2.50E+05	1.258	0.02	350.0	178.6	3.1
	5	9.00E-06	5.56E+05	6.215	0.09	159.8	73.3	2.9
	1	1.60E-05	6.25E+04	0.399	0.01	277.6	279.0	2.8
	4	1.60E-05	2.50E+05	10.00	0.15	45.1	23.0	3.3

	Ns	Area (cm²)	ρs	U (ppm)	±1σ (ppm)	Age (Ma)	±1σ (Ma)	Dpar (um)
	10	1.60E-05	6.25E+05	4.676	0.07	237.5	78.9	3.0
	7	1.60E-05	4.38E+05	5.955	0.09	131.6	51.5	2.8
	1	1.60E-05	6.25E+04	0.631	0.01	176.8	177.7	3.1
	6	1.60E-05	3.75E+05	4.615	0.07	145.4	61.2	3.0
	4	1.60E-05	2.50E+05	3.388	0.05	132.2	67.5	2.6
	7	1.60E-05	4.38E+05	8.203	0.12	95.8	37.5	2.9
	4	1.60E-05	2.50E+05	15.12	0.23	29.9	15.2	3.2
	40	1.60E-05	2.50E+06	26.56	0.40	168.1	31.6	3.0
	27	1.60E-05	1.69E+06	21.83	0.33	138.4	30.1	2.8
	4	1.60E-05	2.50E+05	3.074	0.05	145.5	74.3	3.1
	3	1.60E-05	1.88E+05	4.532	0.07	74.5	43.7	2.9
	26	1.60E-05	1.63E+06	28.65	0.43	101.8	22.5	4.1
	15	1.60E-05	9.38E+05	13.11	0.20	128.1	35.6	3.2
	3	1.60E-05	1.88E+05	1.485	0.02	224.6	131.7	2.9
	Ns	**Area (cm²)**	**ρs**	**U (ppm)**	**±1σ (ppm)**	**Age (Ma)**	**±1σ (Ma)**	**Dpar (um)**
NE-100	6	1.60E-05	3.75E+05	2.169	0.03	305.6	128.6	2.1
	2	1.60E-05	1.25E+05	3.175	0.05	70.9	50.6	2.0
	6	1.60E-05	3.75E+05	2.097	0.03	315.9	132.9	2.1
	3	1.60E-05	1.88E+05	5.212	0.08	64.8	38.0	2.3
	2	1.60E-05	1.25E+05	0.964	0.01	230.5	164.7	2.2
	1	1.60E-05	6.25E+04	0.653	0.01	171.1	172.0	2.4
	4	1.60E-05	2.50E+05	1.751	0.03	253.3	129.3	3.1
	9	1.60E-05	5.63E+05	6.898	0.10	145.9	50.9	3.0
	2	1.60E-05	1.25E+05	0.723	0.01	305.6	218.4	2.8
	4	1.60E-05	2.50E+05	3.343	0.05	134.0	68.4	3.0
	2	1.60E-05	1.25E+05	3.824	0.06	58.9	42.1	2.0
	2	1.60E-05	1.25E+05	0.798	0.01	277.3	198.1	3.2
	5	1.60E-05	3.13E+05	2.376	0.04	233.8	107.2	2.1
	4	1.60E-05	2.50E+05	1.519	0.02	291.3	148.6	2.3
	5	1.60E-05	3.13E+05	4.505	0.07	124.4	57.0	2.8
	1	1.60E-05	6.25E+04	1.681	0.03	66.9	67.3	3.0
	4	1.60E-05	2.50E+05	1.224	0.02	359.5	183.4	3.1
	19	1.60E-05	1.19E+06	11.20	0.17	189.2	47.5	2.2
	13	1.60E-05	8.13E+05	12.69	0.19	114.9	33.9	2.6
	3	1.60E-05	1.88E+05	0.980	0.01	337.3	197.8	2.4
	11	1.60E-05	6.88E+05	18.10	0.27	68.4	21.8	3.2
	18	1.60E-05	1.13E+06	13.19	0.20	152.6	39.2	2.4
	10	1.60E-05	6.25E+05	2.980	0.04	368.9	122.6	2.8
	4	1.60E-05	2.50E+05	1.492	0.02	296.3	151.2	2.4
	1	1.60E-05	6.25E+04	1.328	0.02	84.6	85.1	2.2
	1	1.60E-05	6.25E+04	0.430	0.01	258.1	259.4	2.2
	Ns	**Area (cm²)**	**ρs**	**U (ppm)**	**±1σ (ppm)**	**Age (Ma)**	**±1σ (Ma)**	**Dpar (um)**
LLM-47	13	1.60E-05	8.13E+05	4.574	0.07	313.8	92.7	2.0
	19	1.60E-05	1.19E+06	5.844	0.09	357.7	89.8	3.1
	10	1.60E-05	6.25E+05	14.35	0.22	78.3	26.0	2.2
	51	9.00E-06	5.67E+06	42.97	0.64	234.4	40.6	2.0
	16	1.60E-05	1.00E+06	12.27	0.18	145.9	39.4	2.9
	26	1.60E-05	1.63E+06	10.18	0.15	282.5	62.4	2.8
	11	1.60E-05	6.88E+05	3.542	0.05	342.1	108.9	2.1
	20	9.00E-06	2.22E+06	32.94	0.49	121.0	29.7	2.5
	14	1.60E-05	8.75E+05	18.92	0.28	83.2	23.8	2.3
	7	1.60E-05	4.38E+05	3.441	0.05	226.1	88.5	2.2
	20	9.00E-06	2.22E+06	16.96	0.25	232.9	57.2	2.2
	16	1.60E-05	1.00E+06	6.015	0.09	294.1	79.4	2.6
	58	1.60E-05	3.63E+06	29.11	0.44	221.5	36.8	2.1
	26	1.60E-05	1.63E+06	11.67	0.18	247.2	54.6	2.0
	46	1.60E-05	2.88E+06	22.68	0.34	225.4	40.4	4.1
	42	1.60E-05	2.63E+06	14.82	0.22	312.9	57.9	2.2
	37	1.60E-05	2.31E+06	18.48	0.28	222.6	43.1	2.8
	31	1.60E-05	1.94E+06	16.27	0.24	212.0	43.8	2.5
	4	1.60E-05	2.50E+05	2.936	0.04	152.3	77.7	2.2
	7	1.60E-05	4.38E+05	3.965	0.06	196.7	77.0	3.1
	52	1.60E-05	3.25E+06	30.84	0.46	187.9	32.4	3.3
	6	1.60E-05	3.75E+05	3.099	0.05	215.4	90.6	2.4
	20	1.60E-05	1.25E+06	10.78	0.16	206.5	50.7	3.0
	19	1.60E-05	1.19E+06	22.14	0.33	96.3	24.2	3.1
	5	1.60E-05	3.13E+05	2.610	0.04	213.2	97.8	2.9
	8	1.60E-05	5.00E+05	5.502	0.08	162.4	59.8	2.3
	16	9.00E-06	1.78E+06	13.55	0.20	233.2	63.0	2.2
	12	1.60E-05	7.50E+05	9.197	0.14	145.9	44.7	2.1
	25	1.60E-05	1.56E+06	14.69	0.22	189.7	42.6	2.1
	18	1.60E-05	1.13E+06	15.26	0.23	132.1	33.9	3.1
	5	1.60E-05	3.13E+05	2.256	0.03	246.0	112.8	2.9
	2	1.60E-05	1.25E+05	3.534	0.05	63.7	45.5	2.2
	Ns	**Area (cm²)**	**ρs**	**U (ppm)**	**±1σ (ppm)**	**Age (Ma)**	**±1σ (Ma)**	**Dpar (um)**
LLM-45A	44	1.60E-05	2.75E+06	87.59	1.31	56.6	10.3	2.0
	13	1.60E-05	8.13E+05	16.84	0.25	86.7	25.6	2.1
	14	1.60E-05	8.75E+05	24.13	0.36	65.3	18.7	2.1
	9	1.60E-05	5.63E+05	6.345	0.10	158.5	55.3	2.0
	21	1.60E-05	1.31E+06	21.74	0.33	108.4	26.1	2.0
	17	1.60E-05	1.06E+06	16.42	0.25	116.1	30.5	2.2

16	1.60E-05	1.00E+06	26.67	0.40	67.5	18.2	2.1
16	1.60E-05	1.00E+06	14.78	0.22	121.3	32.7	2.8
30	1.60E-05	1.88E+06	29.09	0.44	115.6	24.2	2.3
27	1.60E-05	1.69E+06	28.21	0.42	107.4	23.4	2.5
16	1.60E-05	1.00E+06	47.10	0.71	38.3	10.3	1.9
19	1.60E-05	1.19E+06	22.46	0.34	95.0	23.8	2.1
22	1.60E-05	1.38E+06	7.614	0.11	318.8	75.4	2.0
37	1.60E-05	2.31E+06	35.21	0.53	117.8	22.8	2.0
14	1.60E-05	8.75E+05	16.99	0.25	92.5	26.5	1.9
15	1.60E-05	9.38E+05	24.83	0.37	68.0	18.9	2.1
22	1.60E-05	1.38E+06	15.45	0.23	159.1	37.6	2.2
13	1.60E-05	8.13E+05	13.17	0.20	110.7	32.7	2.0
10	1.60E-05	6.25E+05	7.052	0.11	158.4	52.6	2.1
24	1.60E-05	1.50E+06	19.15	0.29	140.2	32.0	2.2
11	1.60E-05	6.88E+05	35.10	0.53	35.4	11.3	2.3
11	1.60E-05	6.88E+05	10.55	0.16	116.9	37.2	2.1
17	1.60E-05	1.06E+06	11.21	0.17	169.3	44.5	2.2
22	1.60E-05	1.38E+06	32.24	0.48	76.7	18.1	2.0
21	1.60E-05	1.31E+06	15.57	0.23	150.8	36.3	2.2
26	1.60E-05	1.63E+06	27.14	0.41	107.5	23.8	2.1
18	1.60E-05	1.13E+06	11.71	0.18	171.5	44.1	2.1
28	1.60E-05	1.75E+06	17.16	0.26	182.0	39.1	2.0
43	1.60E-05	2.69E+06	25.28	0.38	189.6	34.8	2.3
11	1.60E-05	6.88E+05	28.87	0.43	43.0	13.7	2.0
29	1.60E-05	1.81E+06	27.00	0.41	120.4	25.5	2.0
17	1.60E-05	1.06E+06	16.71	0.25	114.1	30.0	2.2
15	1.60E-05	9.38E+05	10.34	0.16	162.0	45.0	2.1
11	1.60E-05	6.88E+05	24.78	0.37	50.0	15.9	2.1
16	1.60E-05	1.00E+06	18.17	0.27	98.8	26.7	2.2
27	1.60E-05	1.69E+06	26.69	0.40	113.5	24.7	2.1

Apatite confined fission-track lengths

nl:Number of counted confined fission-tracks.
MTL: Mean track length and standard deviation.
Angle: angle between the confined fission-track and the c-axis of the grain.
Dpar: etch-pit diameter near the confined fission-track.

	NE-14A			NE-15A			LLM-45A			LLM-47			LLM-49	
nl	MTL (µm)	SD (µm)	nl	MTL (µm)	SD (µm)	nl	MTL (µm)	SD (µm)	nl	MTL (µm)	SD (µm)	nl	MTL (µm)	SD (µm)
75	12.40	1.87	51	12.09	1.52	34	12.34	1.87	44	12.23	1.69	65	12.67	1.32
Length (µm)	Angle (°)	Dpar (µm)	Length (µm)	Angle (°)	Dpar (µm)	Length (µm)	Angle (°)	Dpar (µm)	Length (µm)	Angle (°)	Dpar (µm)	Length (µm)	Angle (°)	Dpar (µm)
11.59	78.24	2.37	12.83	46.59	2.22	11.86	68.51	2.01	9.84	46.96	2.86	13.51	22.52	2.23
8.12	50.31	2.37	9.11	51.18	2.15	7.44	10.76	2.01	12.36	79.34	2.86	13.77	55.86	2.23
14.61	3.76	2.37	10.66	68.51	2.15	13.53	75.65	2.12	14.11	53.63	2.89	12.25	56.58	2.36
9.67	74.77	2.42	12.3	46.01	2.15	9.55	56.57	2.12	14.34	76.58	2.89	13.95	79.85	2.36
13.34	48.28	2.42	10.04	17.16	2.09	6.71	61.36	3.2	12.89	25.52	2.89	13.79	39.9	2.36
11.88	89.51	2.42	11.13	74.81	2.37	13.23	66.31	2.49	10.79	49.97	2.81	13.82	62.54	2.36
15.45	54.12	2.18	13.43	49.31	2.37	11.19	75.95	2.91	13.34	53.56	3.18	13.32	63.45	2.16
13.55	56.47	2.18	11.59	73.98	2.37	14.23	66.53	2.76	12.47	37.04	2.99	13.88	60.25	2.16
12.83	76.84	2.09	13.76	55.86	2.21	11.46	58.85	2.76	9.08	87.29	2.99	14.3	78.07	2.43
10.13	70.27	2.23	11.06	66.46	2.21	12.89	74.93	2.76	13.36	57.95	3.36	11.63	47.58	2.43
11.75	47.21	2.23	12.15	80.04	2.21	13.55	83.76	2.76	12.66	26.83	3.36	14.79	59.81	2.46
12.63	74.81	2.23	11.31	34.54	2.38	12.41	51.21	2.39	9.06	85.86	3.36	9.49	55.68	2.46
12.12	89.3	2.14	10.66	75.27	1.92	11.39	77.98	2.39	12.72	55.16	3.36	13.45	24.37	2.46
11.65	53.97	2.14	11.81	46.12	1.92	14.29	50.37	2.38	13.12	54.26	3.36	12.81	83.73	2.46
13.15	18.79	2.14	10.59	71.66	2.06	13.13	85.08	2.24	13.67	63.79	3.04	10.62	28.95	2.46
11.63	71.37	2.05	12.54	56.13	2.06	12.41	59.61	2.24	12.08	26.68	3.04	12.17	43.35	2.46
12.52	79.26	2.37	12.91	33.38	2.27	13.77	85.01	2.24	11.53	13.29	3.36	11.16	60.26	2.46
8.65	68.09	2.37	14.41	56.75	2.27	12.39	40.45	2.31	13.54	51.67	3.36	13.12	47.12	2.48
10.05	70.36	2.37	12.06	69.65	2.27	12.23	32.51	2.16	11.92	25.14	3.36	11.86	57.53	2.48
13.22	31.68	2.37	12.71	37.57	2.27	13.61	81.56	2.16	14.94	64.54	3.09	10.88	82.96	2.67
12.13	74.98	2.37	11.69	15.91	2.27	12.44	82.01	2.41	10.54	31.38	3.09	13.51	68.34	2.67
12.86	36.25	2.63	10.13	80.72	2.27	12.18	77.97	2.41	14.97	24.94	3.39	12.1	75.22	2.67
12.01	81.89	2.63	15.27	47.01	2.12	13.38	59.77	2.24	11.48	88.47	3.39	12.81	70.81	2.65
14.28	45.91	2.63	10.71	58.23	2.12	10.71	75.48	2.09	11.42	60.28	3.39	14.86	59.48	2.65
13.54	53.89	2.63	10.81	84.13	2.12	14.96	53.69	2.59	12.16	37.59	3.39	12.31	79.98	2.51
13.99	35.09	2.63	12.67	63.03	2.12	14.04	48.29	2.59	11.77	63.82	3.39	12.77	41.26	2.51
13.2	77.47	2.63	12.92	33.92	2.61	10.39	38.98	1.83	11.91	59.41	2.82	12.03	63.29	2.83
15.11	75.5	1.85	10.31	49.57	2.61	12.51	41.92	1.83	11.13	71.14	2.82	12.43	74.82	2.83
15.12	26.82	2.24	14.57	65.39	2.33	12.81	42.57	2.23	9.22	30.72	2.75	12.52	44.08	2.83
11.56	36.24	2.24	8.32	50.63	2.47	14.04	6.38	2.37	14.89	54.99	2.75	11.66	59.65	2.54
13.54	64.54	2.22	14.71	73.69	2.47	12.6	85.54	2.31	10.25	25.47	2.75	12.49	51.22	2.41
14.63	54.17	2.22	12.15	33.79	2.47	15.42	26.11	2.28	14.01	34.19	2.75	13.11	24.5	2.41
13.17	14.81	2.22	12.89	33.31	2.62	10.53	65.42	2.28	11.62	65.76	2.75	15.75	55.61	2.46
13.43	54.48	2.22	13.63	82.12	2.62	12.31	19.75	2.28	14.35	25.01	3.32	12.57	44.64	2.86
11.84	40.35	2.22	11.32	35.57	2.35				11.62	2.53	2.85	13.33	70.41	2.82
15.01	63.91	2.52	10.71	65.16	2.35				9.74	51.93	2.85	14.17	84.51	2.82
15.01	27.63	2.52	12.99	86.17	2.46				12.54	26.71	3.21	10.15	68.66	2.77
13.02	68.12	2.52	13.95	35.59	2.46				14.67	65.96	2.71	11.54	39.77	2.77
13.25	23.91	2.52	12.16	51.11	2.46				9.03	46.2	3.08	11.63	76.88	2.77
12.38	31.46	2.28	14.31	57.74	2.34				11.06	83.67	3.08	10.02	78.11	2.43
9.81	49.68	2.28	10.81	28.31	2.34				12.59	46.96	3.08	12.22	65.09	2.43
9.91	41.94	2.28	11.27	71.36	2.34				14.49	77.96	3.08	14.01	33.28	2.43
11.18	86.99	2.28	12.28	50.04	2.34				12.24	81.46	3.08	15.31	41.69	2.38
15.39	56.75	2.28	11.71	61.66	2.34				12.44	52.98	3.08	12.45	47.21	2.38
10.79	60.27	2.28	13.32	81.57	2.12							10.78	52.55	2.62
11.45	89.43	2.52	13.13	15.49	2.12							13.73	40.03	2.62
8.97	67.33	2.52	10.25	68.37	2.12							13.24	62.64	2.62
13.04	57.58	2.11	14.57	57.8	1.94							11.78	45.79	2.62
12.42	37.25	2.11	10.73	73.62	2.02							13.09	80.57	2.62
12.86	76.07	2.11	12.31	86.51	2.02							11.61	66.57	2.62
7.75	59.36	2.11	12.97	27.97	2.02							14.47	56.65	2.07
14.29	76.02	2.11										13.17	81.76	2.41
14.68	82.11	2.11										10.75	85.3	2.41
13.47	73.56	2.11										12.21	56.27	2.41
13.22	78.83	2.19										12.7	45.3	2.57
11.86	34.91	2.12										13.17	13.91	2.38
13.17	64.65	2.12										13.55	44.99	2.38
14.38	58.98	2.12										12.47	84.81	2.41
9.71	87.23	2.12										12.92	70.01	2.48
12.74	72.21	2.09										9.55	46.74	2.48
14.53	67.56	2.46										13.06	38.65	2.48
13.62	47.67	2.46										12.35	80.68	2.48
12.92	59.45	2.46										13.58	45.43	2.73
15.01	78.25	2.11										13.67	27.31	2.73
10.75	10.99	2.24										11.75	78.04	2.73

11.11	51.57	2.24
9.86	73.64	2.21
12.57	79.06	2.21
12.31	57.52	2.35
10.26	43.16	2.35
7.45	58.74	2.25
13.24	78.58	2.25
11.12	61.14	2.43
12.77	26.38	2.43
13.61	54.28	2.26

LLM-53C			LLM-55			NE-98			NE-101		
nl	MTL (µm)	SD (µm)	nl	MTL (µm)	SD (µm)	nl	MTL (µm)	SD (µm)	nl	MTL (µm)	SD (µm)
25	10.82	1.71	38	12.09	1.60	35	12.66	1.79	83	12.38	1.73
Length (µm)	Angle (°)	Dpar (µm)	Length (µm)	Angle (°)	Dpar (µm)	Length (µm)	Angle (°)	Dpar (µm)	Length (µm)	Angle (°)	Dpar (µm)
12.71	77.66	2.38	9.89	62.13	1.77	11.03	25.44	3.34	13.26	68.12	2.03
10.26	54.17	2.38	13.13	79.37	1.77	14.98	49.02	3.31	10.03	47.91	1.94
11.92	58.84	2.38	13.84	81.23	2.03	11.53	49.38	3.31	11.22	27.1	2.08
10.79	79.71	2.38	13.78	31.98	1.89	11.64	31.58	3.31	14.78	56.24	2.08
12.43	19.54	2.52	10.79	39.87	1.89	11.12	87.29	3.06	14.03	56.09	2.08
10.28	68	2.02	13.09	71.58	2.41	11.07	71.68	3.06	12.91	18.03	2.08
9.91	57.74	2.02	10.74	64.39	2.12	11.18	71.02	3.06	12.65	41.14	2.11
10.81	36.65	2.02	13.09	72.11	2.04	10.42	72.81	3.06	13.41	58.06	2.13
7.84	78.04	2.11	12.79	48.77	2.04	12.65	13.75	3.06	10.59	33.96	2.23
7.68	34.34	2.11	10.39	78.51	2.04	10.91	71.43	3.75	15	64.45	2.19
11.68	70.83	2.11	11.42	66.92	2.04	11.07	71.83	3.58	14.28	44.73	2.19
14.18	48.37	2.21	14.44	55.57	2.11	14.67	61.46	3.12	11.97	75.27	2.19
11.97	33.51	2.21	13.61	16.67	2.11	13.23	64.29	3.81	12.83	45.79	2.19
12.86	77.83	2.21	12.19	72.57	2.11	13.16	40.01	3.42	10.15	60.82	2.19
14.03	36.81	2.18	10.27	74.74	2.11	9.41	70.86	3.42	12.01	89.28	2.19
9.32	89.34	2.18	12.18	41.41	2.44	15.83	22.36	3.32	9.97	44.27	2.19
9.22	82.91	2.18	10.97	8.63	2.44	8.23	54.89	3.03	15.97	60.06	2.23
9.19	26.39	2.18	11.98	2.18	2.44	12.33	81.67	3.31	9.67	81.75	2.23
9.34	73.98	2.18	14.41	81.23	2.01	10.87	65.81	3.31	13.51	37.14	2.11
9.86	63.53	2.06	11.09	63.32	2.01	11.04	83.16	3.31	13.83	34.58	2.11
11.14	69.79	2.06	15.19	76.3	2.31	13.99	61.46	3.31	10.38	74.48	2.01
10.07	83.29	2.11	9.05	67.33	2.31	15.59	26.59	3.31	12.44	26	2.01
12.5	28.54	2.23	10.71	35.55	2.39	11.7	18.55	3.33	11.39	37.09	2.01
10.27	75.28	2.03	12.71	83.91	1.98	14.18	79.46	3.33	12.79	73.46	2.01
10.28	64.92	2.21	9.55	76.74	1.98	14.12	59.04	3.23	11.52	77.11	2.01
			12.13	25.71	1.98	14.09	87.2	3.23	15.07	17.97	2.04
			10.09	55.46	1.98	13.11	29.33	3.23	12.72	25.42	2.04
			14.37	58.06	2.17	13.65	45.29	3.71	14.23	89.86	1.99
			13.47	64.48	2.15	14.03	56.59	3.77	13.92	3.4	1.99
			10.56	63.48	2.15	14.42	77.23	3.25	13.59	77.78	1.99
			13.75	47.65	2.15	13.21	67.74	3.72	12.81	77.62	2.05
			12.57	40.04	2.41	13.15	64.52	3.72	11.62	78.69	2.05
			13.31	88.36	2.41	13.51	85.26	3.66	12.98	65.33	2.05
			11.92	47.34	2.41	13.25	3.82	3.66	13.87	46.11	2.38
			10.8	84.77	2.19	14.81	75.47	4.38	10.87	16.05	2.38
			9.59	79.45	2.19				14.32	55.32	2.38
			12.63	26.99	2.19				9.38	17.61	2.38
			13.06	63.97	2.19				12.85	62.49	2.15
									9.48	20.48	2.15
									12.42	37.06	2.15
									10.35	72.07	2.15
									11.54	71.08	2.15
									14.46	63.99	2.15
									11.52	72	2.15
									13.73	51.51	2.04
									8.14	54.01	2.04
									14.21	77.85	2.06
									14.76	71.07	2.06
									12.81	22.62	2.06
									14.25	13.68	2.06
									9.37	79.93	2.12
									14.16	30.36	2.12
									13.12	31.83	2.12
									11.85	50.86	2.12
									11.21	21.93	2.12
									10.88	89.07	2.01
									10.34	70.98	2.01
									11.7	24.81	2.14
									13.67	61.3	2.14
									13.82	69.71	2.14
									11.19	14.39	2.26
									13.43	65.92	2.26
									13.34	45.85	1.97

10.97	23.66	1.97
10.4	69.58	1.97
13.38	28.61	1.97
16.13	46.32	1.97
11.78	73.26	1.97
11.64	59.97	2.16
9.91	63.79	2.14
9.5	81.35	2.18
11.28	18.99	1.97
12.57	73.54	1.97
11.82	47.19	1.97
11.97	77.29	1.97
14.31	79.57	2.55
11.56	23.63	2.55
13.49	65.36	2.55
15	48.6	2.55
9.61	76.21	2.13
11.05	79.98	2.13
13.06	54.11	2.13
13.44	84.59	2.19

Zircon fission-track radial plots

Single-grain zircon fission-track ages and U content (in ppm). All diagrams were generated in the IsoplotR (Vermeesch, 2018).

References

Vermeesch, P. (2018). IsoplotR: A free and open toolbox for geochronology. *Geoscience Frontiers*, *9*(5), 1479–1493. https://doi.org/10.1016/j.gsf.2018.04.001
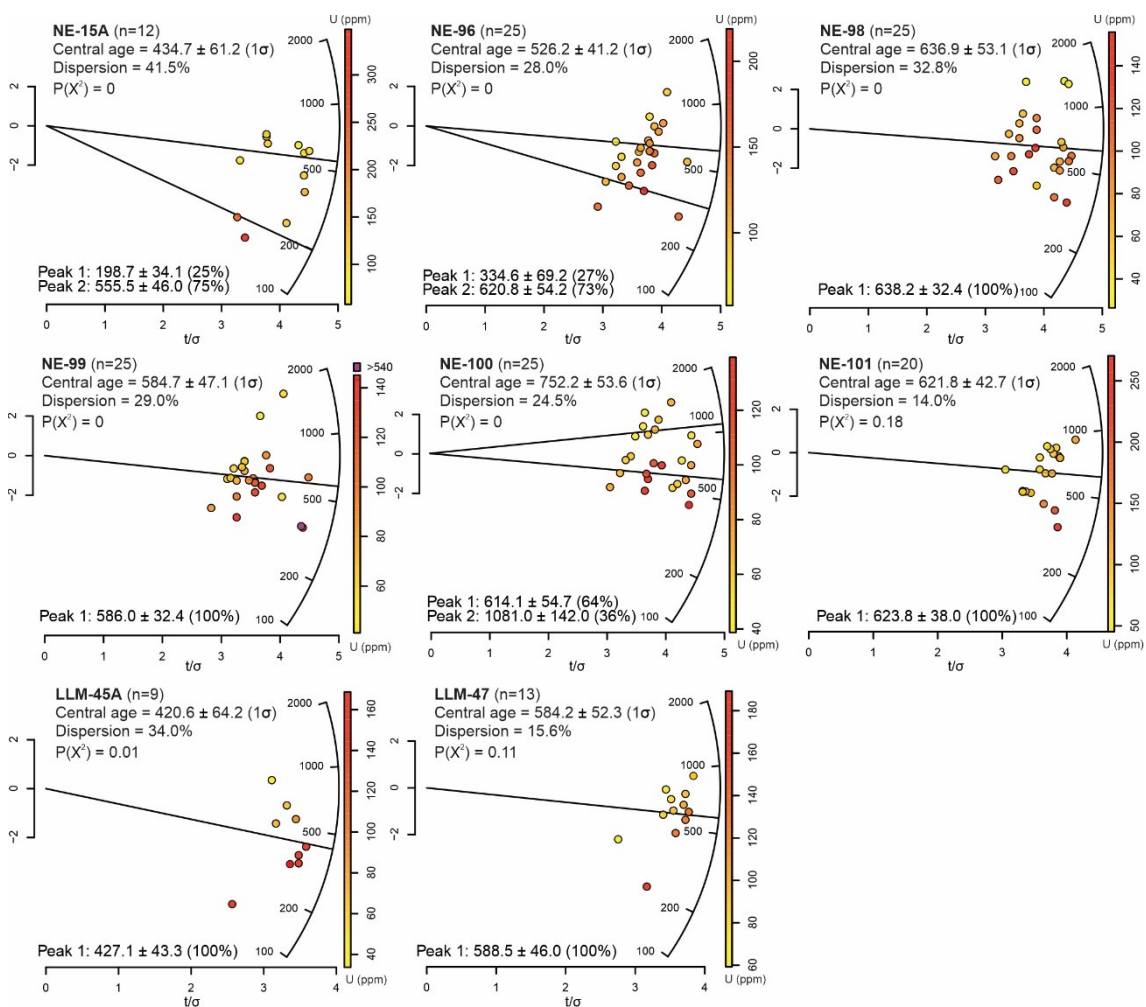
Zircon fission-track results

n: Grains.

Ns: Counted tracks.

ρ(s): Track density in the sample.

U-UNK: ^{238}U content in the sample.

P(X^2) is the chi-squared probability test that dated single-grains belong to the same statistical population (samples fails the test if values are < 0.05).

Area: Counted area .

The zeta value (ζ) of the standard Fish Canyon Tuff (FCT) used was a mean of all analytic sessions: 2.324×10^3.

The track density [ρ(STD)] of the standard Fish Canyon Tuff zircon (FCT) used was a mean of all analytic sessions: 6.80×10^6.

The ^{238}U content used for the Fish Canyon Tuff zircon (FCT) to determine the zeta value was 539.80 ± 1.5% ppm.

The matrix-matched reference material used to calculate the ^{238}U content of all unknown samples and the FCT was the 91500 standard (81.2 ± 1% ppm; Wiedenbeck et al., 1995).

References

Wiedenbeck, M. A. P. C., Alle, P., Corfu, F. Y., Griffin, W. L., Meier, M., Oberli, F. V., ... & Spiegel, W. (1995). Three natural zircon standards for U-Th-Pb, Lu-Hf, trace element and REE analyses. *Geostandards newsletter*, *19*(1), 1-23.

Sample	n	Ns	ρ(s) ×10^6	U ppm	Pooled Age Ma	Central Age Ma	P1 Ma	Fraction (P1) %	P2 Ma	Fraction (P2) %	P(χ^2)	Dispersion %
NE-15A	12	710	2.50	138.80	433.6±20.2	434.7±61.2	198.7±34.1	25.2	555.5±46.0	74.8	0	41.5
NE-96	25	879	2.99	125.30	502.8±21.9	526.2±41.2	334.6±69.2	26.6	620.8±54.2	73.4	0	28.0
NE-98	25	1311	2.41	85.30	588.9±23.0	636.9±53.1	638.2±32.4	100.0	X	X	0	32.8
NE-99	25	809	2.47	108.50	497.3±22.2	584.7±47.1	586.0±32.4	100.0	X	X	0	29.0
NE-100	25	1278	2.72	79.10	694.6±27.3	752.2±53.6	614.1±54.7	64.3	1081.0±142.0	35.7	0	24.5
NE-101	20	632	3.06	115.60	605.9±29.3	621.8±42.7	623.8±38.0	100.0	X	X	0.18	14.0
LLM-47	13	351	2.70	105.40	570.3±34.3	584.2±52.3	588.5±46.0	100.0	X	X	0.11	15.6
LLM-45A	9	181	2.01	116.10	390.4±38.0	420.6±64.2	427.1±43.3	100.0	X	X	0.01	34.0

	Ns	Area (cm²)	ρs	U (ppm)	±1σ (ppm)	Age (Ma)	±1σ (Ma)
NE-15A	97	4.00E-06	2.43E+07	92.04	0.07	584.9	132.4
	19	1.00E-06	1.90E+07	226.0	0.58	192.5	58.9
	34	1.00E-06	3.40E+07	108.3	0.15	691.2	183.3
	99	4.00E-06	2.48E+07	149.8	0.19	373.1	84.3
	55	4.00E-06	1.38E+07	130.8	0.12	239.7	58.3
	96	4.00E-06	2.40E+07	119.4	0.14	450.8	102.1
	22	1.00E-06	2.20E+07	337.4	1.09	149.8	44.0
	35	1.00E-06	3.50E+07	122.9	0.18	629.9	166.0
	20	1.00E-06	2.00E+07	95.17	0.08	470.8	141.9
	34	1.00E-06	3.40E+07	104.6	0.10	714.2	189.4
	120	4.00E-06	3.00E+07	110.5	0.11	601.8	133.5
	79	4.00E-06	1.98E+07	68.59	0.10	636.7	147.4
	Ns	Area (cm²)	ρs	U (ppm)	±1σ (ppm)	Age (Ma)	±1σ (Ma)
NE-96	28	1.00E-06	2.80E+07	111.7	0.24	557.5	154.3
	74	4.00E-06	1.85E+07	153.0	0.15	275.0	64.2
	37	1.00E-06	3.70E+07	173.6	0.29	477.2	124.4
	36	1.00E-06	3.60E+07	140.3	0.26	570.3	149.5
	31	1.00E-06	3.10E+07	212.9	0.94	329.7	89.2
	35	1.00E-06	3.50E+07	83.62	0.05	905.9	238.8
	13	1.00E-06	1.30E+07	150.6	0.21	197.6	67.8
	39	1.00E-06	3.90E+07	106.9	0.13	796.4	205.4
	48	1.00E-06	4.80E+07	126.1	0.95	828.7	205.9
	27	1.00E-06	2.70E+07	126.4	0.18	478.4	133.5
	39	1.00E-06	3.90E+07	154.6	0.26	561.2	144.8
	18	1.00E-06	1.80E+07	63.59	0.31	626.4	194.5

Ns	Area (cm²)	ρs	U (ppm)	±1σ (ppm)	Age (Ma)	±1σ (Ma)
15	1.00E-06	1.50E+07	106.8	0.08	318.5	104.4
53	1.00E-06	5.30E+07	92.12	0.06	1215.1	297.1
35	1.00E-06	3.50E+07	135.9	0.15	572.5	150.9
20	1.00E-06	2.00E+07	89.29	0.04	500.6	150.9
20	1.00E-06	2.00E+07	122.8	0.11	367.8	110.9
29	1.00E-06	2.90E+07	109.0	0.13	590.2	162.0
34	1.00E-06	3.40E+07	113.9	0.17	659.0	174.7
100	4.00E-06	2.50E+07	104.8	0.07	531.9	120.0
18	1.00E-06	1.80E+07	94.62	0.08	427.6	132.8
29	1.00E-06	2.90E+07	155.8	0.19	418.7	115.0
23	1.00E-06	2.30E+07	156.0	0.14	333.9	97.0
35	1.00E-06	3.50E+07	121.9	0.12	635.0	167.4
43	1.00E-06	4.30E+07	126.6	0.15	744.4	188.5

	Ns	Area (cm²)	ρs	U (ppm)	±1σ (ppm)	Age (Ma)	±1σ (Ma)
NE-98	39	4.00E-06	9.75E+06	57.89	0.03	380.0	98.0
	27	1.00E-06	2.70E+07	84.73	0.10	701.0	195.7
	27	1.00E-06	2.70E+07	67.81	0.04	864.7	241.4
	29	1.00E-06	2.90E+07	63.09	0.02	988.4	271.4
	61	4.00E-06	1.53E+07	99.07	0.08	348.2	83.3
	110	4.00E-06	2.75E+07	103.8	0.06	588.0	131.5
	24	1.00E-06	2.40E+07	125.1	0.09	431.1	123.9
	81	4.00E-06	2.03E+07	69.49	0.05	644.0	148.6
	91	4.00E-06	2.28E+07	151.0	0.22	340.9	77.7
	39	1.00E-06	3.90E+07	107.8	0.09	790.2	203.8
	72	4.00E-06	1.80E+07	73.97	0.02	542.1	126.9
	22	1.00E-06	2.20E+07	64.99	0.02	742.3	218.1
	31	1.00E-06	3.10E+07	41.78	0.05	1528.2	413.3
	84	4.00E-06	2.10E+07	31.25	0.03	1398.5	321.4
	39	1.00E-06	3.90E+07	91.48	0.04	921.7	237.7
	23	1.00E-06	2.30E+07	95.88	0.07	534.7	155.3
	76	4.00E-06	1.90E+07	61.14	0.03	684.6	159.2
	61	4.00E-06	1.53E+07	68.33	0.03	498.8	119.4
	18	1.00E-06	1.80E+07	113.7	0.12	357.7	111.1
	72	4.00E-06	1.80E+07	82.66	0.06	487.2	114.0
	33	1.00E-06	3.30E+07	129.4	0.08	566.9	151.3
	99	4.00E-06	2.48E+07	99.76	0.08	552.2	124.7
	38	1.00E-06	3.80E+07	135.2	0.55	622.3	161.3
	17	1.00E-06	1.70E+07	73.60	0.02	515.6	162.8
	98	4.00E-06	2.45E+07	38.21	0.02	1340.7	303.1

	Ns	Area (cm²)	ρs	U (ppm)	±1σ (ppm)	Age (Ma)	±1σ (Ma)
NE-99	92	4.00E-06	2.30E+07	148.7	1.06	349.8	79.6
	26	1.00E-06	2.60E+07	99.57	0.12	580.0	163.4
	16	1.00E-06	1.60E+07	64.97	0.07	548.3	176.3
	37	1.00E-06	3.70E+07	120.3	0.21	677.9	176.7
	12	1.00E-06	1.20E+07	86.31	0.07	315.3	111.1
	115	4.00E-06	2.88E+07	101.6	0.09	626.4	139.5
	49	4.00E-06	1.23E+07	57.38	0.07	477.9	118.3
	19	1.00E-06	1.90E+07	100.4	0.11	425.6	130.2
	27	1.00E-06	2.70E+07	108.5	0.37	553.6	154.6
	22	1.00E-06	2.20E+07	65.41	0.05	737.8	216.8
	85	1.00E-06	8.50E+07	544.3	3.02	353.1	81.0
	27	1.00E-06	2.70E+07	110.2	0.13	545.5	152.3
	18	1.00E-06	1.80E+07	60.73	0.05	654.4	203.2
	17	1.00E-06	1.70E+07	67.40	0.06	561.1	177.2
	31	1.00E-06	3.10E+07	130.2	0.18	530.9	143.6
	22	1.00E-06	2.20E+07	65.69	0.07	734.8	215.9
	51	1.00E-06	5.10E+07	59.87	0.06	1726.3	424.6
	19	1.00E-06	1.90E+07	77.77	0.16	544.2	166.4
	22	1.00E-06	2.20E+07	76.23	0.10	638.1	187.5
	24	1.00E-06	2.40E+07	95.53	0.45	558.9	160.6
	21	1.00E-06	2.10E+07	68.75	0.07	673.5	200.4
	19	1.00E-06	1.90E+07	139.7	0.55	308.5	94.4
	30	1.00E-06	3.00E+07	45.22	0.02	1382.3	376.6
	34	1.00E-06	3.40E+07	92.23	0.17	804.4	213.3
	27	1.00E-06	2.70E+07	126.8	0.23	476.7	133.1

	Ns	Area (cm²)	ρs	U (ppm)	±1σ (ppm)	Age (Ma)	±1σ (Ma)
NE-100	92	4.00E-06	2.30E+07	116.3	0.07	443.9	101.0
	31	1.00E-06	3.10E+07	121.8	0.12	566.1	153.1
	100	4.00E-06	2.50E+07	78.25	0.08	702.8	158.6
	53	1.00E-06	5.30E+07	72.18	0.05	1514.0	370.1
	42	1.00E-06	4.20E+07	134.0	0.11	689.9	175.5
	31	1.00E-06	3.10E+07	63.76	0.02	1041.2	281.6
	101	4.00E-06	2.53E+07	55.01	0.03	987.1	222.5
	28	1.00E-06	2.80E+07	50.41	0.03	1176.6	325.7
	55	4.00E-06	1.38E+07	58.21	0.02	526.8	128.1
	39	1.00E-06	3.90E+07	65.71	0.06	1249.9	322.4
	29	1.00E-06	2.90E+07	42.46	0.02	1419.0	389.6
	24	1.00E-06	2.40E+07	49.80	0.02	1032.8	296.8
	18	1.00E-06	1.80E+07	67.45	0.03	592.2	183.9
	72	4.00E-06	1.80E+07	53.38	0.03	739.5	173.1
	35	1.00E-06	3.50E+07	109.1	0.10	705.6	186.0

	Ns	Area (cm²)	ρs	U (ppm)	±1σ (ppm)	Age (Ma)	±1σ (Ma)
	22	1.00E-06	2.20E+07	62.40	0.02	771.3	226.7
	36	1.00E-06	3.60E+07	69.48	0.03	1103.9	289.3
	63	4.00E-06	1.58E+07	63.00	0.03	556.3	132.5
	30	1.00E-06	3.00E+07	109.5	0.09	607.4	165.5
	82	4.00E-06	2.05E+07	77.21	0.04	589.3	135.8
	20	1.00E-06	2.00E+07	60.31	0.04	728.0	219.5
	29	1.00E-06	2.90E+07	135.6	0.16	478.7	131.4
	100	4.00E-06	2.50E+07	110.0	0.08	507.7	114.6
	131	4.00E-06	3.28E+07	79.36	0.12	894.0	197.0
	15	1.00E-06	1.50E+07	73.07	0.05	460.2	150.9
	Ns	Area (cm²)	ρs	U (ppm)	±1σ (ppm)	Age (Ma)	±1σ (Ma)
NE-101	23	1.00E-06	2.30E+07	110.4	0.45	466.9	135.6
	39	1.00E-06	3.90E+07	111.4	0.10	766.4	197.7
	21	1.00E-06	2.10E+07	100.0	0.07	470.2	139.9
	27	1.00E-06	2.70E+07	78.68	0.08	751.9	209.9
	29	1.00E-06	2.90E+07	156.0	0.33	418.2	114.8
	15	1.00E-06	1.50E+07	53.64	0.06	619.2	203.1
	27	1.00E-06	2.70E+07	92.71	0.21	643.6	179.7
	57	1.00E-06	5.70E+07	133.4	0.34	923.3	223.2
	20	1.00E-06	2.00E+07	95.51	0.13	469.2	141.5
	37	1.00E-06	3.70E+07	94.95	0.15	847.4	220.9
	35	1.00E-06	3.50E+07	96.92	0.13	788.9	207.9
	20	1.00E-06	2.00E+07	96.63	0.13	463.9	139.9
	30	1.00E-06	3.00E+07	107.7	0.45	616.9	168.1
	38	1.00E-06	3.80E+07	262.1	1.17	328.4	85.1
	33	1.00E-06	3.30E+07	85.93	0.14	835.9	223.0
	40	1.00E-06	4.00E+07	116.8	0.15	750.5	192.7
	40	1.00E-06	4.00E+07	116.6	0.09	751.6	193.0
	31	1.00E-06	3.10E+07	77.71	0.12	866.2	234.3
	34	1.00E-06	3.40E+07	121.4	1.32	620.0	164.4
	36	1.00E-06	3.60E+07	203.6	2.34	398.4	104.4
	Ns	Area (cm²)	ρs	U (ppm)	±1σ (ppm)	Age (Ma)	±1σ (Ma)
LLM-47	37	1.00E-06	3.70E+07	87.53	0.13	914.4	238.3
	11	1.00E-06	1.10E+07	69.08	0.09	359.8	130.6
	26	1.00E-06	2.60E+07	94.69	0.09	608.5	171.4
	25	1.00E-06	2.50E+07	78.93	0.04	697.0	198.2
	32	1.00E-06	3.20E+07	93.99	0.06	746.3	200.5
	22	1.00E-06	2.20E+07	85.59	0.08	571.3	167.9
	17	1.00E-06	1.70E+07	184.4	0.32	210.7	66.6
	32	1.00E-06	3.20E+07	128.5	0.77	554.2	148.9
	31	1.00E-06	3.10E+07	104.1	0.31	657.7	177.9
	27	1.00E-06	2.70E+07	129.8	0.17	466.3	130.2
	23	1.00E-06	2.30E+07	64.08	0.03	784.4	227.9
	34	1.00E-06	3.40E+07	123.8	0.38	608.7	161.4
	34	1.00E-06	3.40E+07	123.6	28.33	609.3	161.6
	Ns	Area (cm²)	ρs	U (ppm)	±1σ (ppm)	Age (Ma)	±1σ (Ma)
LLM-45A	21	1.00E-06	2.10E+07	149.2	0.19	319.0	94.9
	20	1.00E-06	2.00E+07	67.91	0.05	650.5	196.1
	23	1.00E-06	2.30E+07	91.93	0.13	556.7	161.7
	16	1.00E-06	1.60E+07	38.77	1.33	894.2	287.5
	27	1.00E-06	2.70E+07	147.5	0.29	411.9	115.0
	24	1.00E-06	2.40E+07	163.5	0.32	332.4	95.5
	9	1.00E-06	9.00E+06	163.6	1.03	126.6	49.4
	24	1.00E-06	2.40E+07	148.3	0.20	365.6	105.0
	17	1.00E-06	1.70E+07	74.50	0.10	509.6	160.9

Apatite (U-Th)/He results

The amount of ^{4}He is given in nano-cubic-cm in standard temperature and pressure.
eU: the effective uranium content given by eU = [U]+0.235*[Th]
F$_T$: alpha-ejection correction (according to Farley et al., 1996; Hourigan et al., 2005)
No. Py.: Number of pyramidal terminations of the grain.
ESR: equivalent spherical radius.

References

Farley, K. A., Wolf, R. A., & Silver, L. T. (1996). The effects of long alpha-stopping distances on (U-Th)/He ages. *Geochimica et Cosmochimica Acta*, *60*(21), 4223–4229.

Hourigan, J. K., Reiners, P. W., & Brandon, M. T. (2005). U-Th zonation-dependent alpha-ejection in (U-Th)/He chronometry. *Geochimica et Cosmochimica Acta*, *69*(13), 3349–3365.

Sample	^{4}He (ncc)	±1σ (ncc)	^{238}U (ppm)	±1σ (ppm)	^{232}Th (ppm)	±1σ (ppm)	Th/U	Sm (ppm)	±1σ (ppm)	eU (ppm)	Uncorr. age (Ma)	±1σ (Ma)	F$_T$	Age$_{corr}$ (Ma)	±1σ (Ma)	Length (μm)	Width (μm)	No. Py.	ESR (μm)	Mass (μg)	Mean age ± SD (Ma)
NE-06A-a1	1.184	0.037	13.05	0.13	14.41	0.14	1.10	65.47	1.19	16.40	58.96	3.78	0.754	78.20	5.21	175.4	113.7	2	58.4	7.14	38 ± 24
NE-06A-a2	0.160	0.006	6.97	0.07	8.60	0.09	1.23	61.64	1.22	8.97	14.53	1.08	0.758	19.17	1.62	174.8	123.7	2	59.5	7.50	
NE-06A-a3	0.296	0.016	6.43	0.06	7.17	0.07	1.12	45.02	0.86	8.09	29.91	3.26	0.763	39.20	4.47	189.7	123.8	2	60.7	8.03	
NE-06A-a4	0.352	0.018	13.03	0.13	9.38	0.09	0.72	17.14	0.51	15.21	19.05	1.94	0.745	25.57	2.80	168.8	98.8	2	56.3	6.45	
NE-06A-a5	0.278	0.025	9.17	0.09	8.74	0.09	0.95	46.93	0.89	11.20	20.36	3.62	0.756	26.93	4.99	156.0	116.4	1	58.4	7.72	
NE-14A-a1	0.513	0.001	8.48	0.38	9.42	0.94	1.11	81.70	25.88	10.67	39.21	2.79	0.752	52.14	3.91	155.4	106.4	0	57.3	7.98	61 ± 33
NE-14A-a2	1.006	0.052	26.85	0.27	15.10	0.15	0.56	31.64	0.66	30.36	27.27	2.83	0.763	35.74	3.91	178.2	115.3	0	60.1	9.38	
NE-14A-a3	2.663	0.131	22.96	0.23	11.33	0.11	0.49	30.64	0.58	25.58	85.25	8.46	0.755	112.91	11.41	171.6	106.4	0	58.1	8.50	
NE-14A-a4	1.754	0.021	24.97	0.25	8.90	0.09	0.36	15.32	0.48	27.03	53.37	1.61	0.742	71.93	2.37	134.1	94.4	0	54.6	6.71	
NE-14A-a5	0.132	0.006	3.70	0.00	2.78	0.00	0.75	2.77	0.15	4.35	25.02	2.34	0.756	33.10	3.30	151.4	111.5	0	58.2	8.33	
NE-15A-a1	2.529	0.041	16.63	0.17	15.84	0.16	0.95	32.43	0.71	20.30	101.72	3.64	0.778	130.75	4.88	224.5	134.9	2	65.2	9.95	103 ± 26
NE-15A-a2	1.491	0.041	11.50	0.11	6.45	0.06	0.56	19.57	0.46	13.00	93.85	5.38	0.749	125.30	7.38	186.3	100.6	1	57.2	7.62	
NE-15A-a3	1.481	0.018	12.97	0.13	7.10	0.07	0.55	32.84	0.65	14.61	82.94	2.48	0.778	106.61	3.39	263.1	119.1	0	64.5	12.50	
NE-15A-a4	0.759	0.047	9.30	0.09	5.14	0.05	0.55	18.94	0.49	10.49	59.36	7.35	0.780	76.10	9.62	194.3	137.6	1	65.1	10.61	
NE-15A-a5	1.864	0.064	22.50	0.22	17.89	0.18	0.80	40.41	0.90	26.65	57.35	4.01	0.752	76.26	5.53	214.1	98.9	1	57.5	8.12	
NE-96-1a	0.215	0.007	9.75	0.10	1.84	0.02	0.19	8.62	0.32	10.17	17.48	1.18	0.748	23.37	1.78	148.0	104.8	1	56.5	6.93	43 ± 22
NE-96-a2	0.533	0.011	10.66	0.11	2.07	0.02	0.19	7.53	0.24	11.14	39.42	1.75	0.744	52.98	2.55	156.8	95.6	1	55.7	6.75	
NE-96-a3	0.734	0.003	10.18	0.10	1.74	0.02	0.17	13.83	0.41	10.59	56.96	1.18	0.752	75.74	1.77	158.9	110.6	1	57.9	7.53	
NE-96-a4	0.182	0.004	4.25	0.04	1.49	0.01	0.35	3.32	0.25	4.60	32.56	1.55	0.756	43.07	2.25	181.6	113.8	2	58.8	7.35	
NE-96-a5	0.230	0.011	10.57	0.11	1.96	0.02	0.19	22.20	0.58	11.02	17.18	1.65	0.768	22.37	2.35	215.0	122.1	2	62.1	8.82	
LLM-47-a1	1.406	0.051	19.42	0.19	22.43	0.22	1.16	15.12	0.42	24.63	46.85	3.49	0.731	64.09	4.97	148.0	104.8	1	52.4	2.91	38 ± 22
LLM-47-a2	0.091	0.005	3.32	0.03	1.66	0.02	0.50	1.90	0.13	3.70	20.30	2.58	0.719	28.23	3.79	156.8	95.6	1	50.1	2.68	
LLM-47-a3	0.097	0.005	5.30	0.05	4.77	0.05	0.90	3.91	0.20	6.41	12.46	1.25	0.744	16.75	1.88	155.9	110.6	1	55.3	3.43	
LLM-47-a4	0.200	0.012	8.85	0.09	6.20	0.06	0.70	7.78	0.29	10.29	16.05	1.92	0.759	21.15	2.73	181.6	113.8	2	59.1	4.36	
LLM-47-a5	0.352	0.021	5.38	0.05	3.94	0.04	0.73	3.28	0.18	6.30	45.96	5.52	0.774	59.38	7.33	216.0	122.1	2	64.0	4.80	
LLM-49-a1	1.184	0.024	22.11	0.22	7.98	0.08	0.36	44.67	0.85	23.97	40.62	1.80	0.759	53.52	2.57	206.7	112.8	2	59.9	8.04	44 ± 19
LLM-49-a2	0.697	0.028	21.39	0.21	7.38	0.07	0.35	50.81	1.00	23.10	24.84	2.07	0.762	32.60	2.92	246.5	105.6	0	60.0	10.31	
LLM-49-a3	0.056	0.005	2.40	0.02	1.42	0.01	0.59	17.67	0.09	2.73	16.83	3.07	0.787	21.39	4.10	211.4	135.5	0	67.3	12.90	
LLM-49-a4	1.433	0.039	32.91	0.33	13.49	0.13	0.41	65.27	1.18	36.04	32.71	1.87	0.780	41.94	2.60	207.3	128.7	0	65.1	11.86	
LLM-49-a5	2.089	0.041	29.02	0.29	8.56	0.09	0.29	34.70	0.77	31.01	55.38	2.40	0.774	71.55	3.30	195.7	124.0	0	63.2	10.88	
LLM-53C-a1	0.197	0.008	3.84	0.04	10.84	0.11	2.83	7.67	0.27	6.35	25.32	2.05	0.752	33.67	2.93	207.5	104.5	1	57.5	4.42	82 ± 45
LLM-53C-a2	1.724	0.020	6.71	0.05	32.01	0.32	4.77	79.65	25.36	14.14	98.54	2.39	0.738	133.52	3.44	280.8	92.0	2	54.7	4.34	
LLM-53C-a3	0.146	0.007	1.00	0.01	1.62	0.02	1.62	16.48	0.12	1.38	85.38	8.23	0.684	124.82	12.23	157.2	84.1	2	44.8	1.70	
LLM-53C-a4	0.768	0.031	9.87	0.01	29.47	0.29	2.99	17.85	0.46	16.71	37.57	3.03	0.765	49.11	4.16	202.8	118.2	2	61.2	4.16	
LLM-53C-a5	0.899	0.090	8.31	0.08	26.73	0.27	3.22	23.00	0.61	14.51	50.56	10.11	0.727	69.55	14.11	145.5	104.2	0	51.8	2.82	
LLM-55-a1	1.616	0.052	27.25	0.27	19.90	0.20	0.73	18.24	0.49	31.87	41.70	2.77	0.758	55.01	3.85	211.4	106.7	1	59.2	8.67	73 ± 18
LLM-55-a2	0.751	0.023	13.38	0.13	1.43	0.08	0.11	7.83	0.42	13.71	40.33	2.56	0.736	54.80	3.68	204.5	82.5	2	53.9	6.78	
LLM-55-a3	1.704	0.051	18.76	0.19	0.25	0.10	0.01	11.45	0.36	18.81	66.73	4.14	0.763	87.46	5.63	210.8	115.3	2	60.5	8.27	
LLM-55-a4	0.228	0.002	2.19	0.02	1.67	0.02	0.76	13.25	0.10	2.58	72.29	1.60	0.761	94.99	2.30	197.7	112.7	1	60.0	8.78	
LLM-55-a5	0.989	0.002	12.73	0.13	9.21	0.09	0.72	11.26	0.33	14.87	54.63	0.94	0.750	72.84	1.45	198.9	100.1	2	57.4	7.17	
LLM-59-a1	0.063	0.003	1.78	0.02	1.29	0.01	0.73	1.05	0.09	2.08	25.16	2.64	0.758	33.19	3.68	237.9	105.5	2	59.5	4.44	48 ± 23
LLM-59-a2	0.470	0.025	8.31	0.08	20.22	0.20	2.43	58.81	1.16	13.00	29.45	3.14	0.774	38.05	4.26	224.2	111.8	0	63.6	4.89	
LLM-59-a3	0.213	0.003	3.68	0.07	12.54	0.01	3.41	171.24	34.99	6.59	25.69	0.97	0.769	33.41	1.46	199.5	116.5	1	61.8	5.32	
LLM-59-a4	0.458	0.043	7.82	0.08	10.40	0.10	1.33	36.06	0.76	10.24	36.59	6.87	0.762	48.02	9.22	158.0	115.6	0	59.2	4.90	
LLM-59-a5	0.944	0.036	8.00	0.08	15.44	0.15	1.93	44.35	0.95	11.58	66.42	5.06	0.758	87.63	6.88	193.8	110.9	1	59.0	4.49	
NE-97A-a1	0.102	0.007	1.97	0.02	6.60	0.07	3.36	8.39	0.32	3.50	23.90	3.27	0.763	31.32	4.49	149.0	119.5	0	59.5	4.86	78 ± 46
NE-97A-a2	0.166	0.011	3.71	0.01	11.77	0.02	3.17	2.22	0.15	6.44	21.03	2.79	0.745	28.23	3.94	177.9	103.1	0	55.2	4.30	
NE-97A-a3	0.480	0.021	3.70	0.04	13.36	0.13	3.61	10.43	0.30	6.80	57.50	5.05	0.686	83.82	7.56	174.9	79.5	2	44.4	2.94	
NE-97A-a4	0.682	0.022	6.42	0.06	3.78	0.04	0.59	9.39	0.31	7.30	76.59	5.02	0.672	113.97	7.67	189.0	78.7	0	41.9	1.83	
NE-97A-a5	0.206	0.009	1.38	0.01	1.24	0.01	0.90	13.01	0.10	1.66	100.65	8.57	0.776	129.70	11.24	137.5	134.5	1	63.0	5.64	
NE-98-a1	1.828	0.019	10.25	0.10	25.99	0.26	2.53	22.44	3.50	16.28	91.47	2.23	0.694	131.80	3.41	173.1	85.4	1	46.5	2.00	60 ± 41

NE-98-a2	0.256	0.018	5.87	0.06	2.33	0.02	0.40	6.14	0.28	6.41	32.83	4.57	0.764	42.97	6.18	211.2	114.6	1	61.0	4.25	
NE-98-a3	0.067	0.002	1.37	0.01	2.23	0.02	1.62	15.98	0.10	1.89	28.82	1.35	0.730	39.48	2.05	166.1	106.0	0	53.0	2.60	
NE-98-a4	0.103	0.002	3.18	0.03	1.94	0.02	0.61	2.88	0.19	3.63	23.44	0.99	0.746	31.42	1.53	193.4	106.8	2	56.5	3.33	
NE-98-a5	0.115	0.001	2.22	0.02	1.26	0.01	0.57	3.47	0.19	2.51	37.72	1.09	0.708	53.28	1.74	153.9	97.4	1	48.8	2.04	
NE-101-a1	0.143	0.003	1.69	0.02	1.15	0.01	0.68	14.62	0.11	1.96	59.66	3.07	0.753	79.23	4.28	210.9	101.0	0	57.8	8.92	83 ± 16
NE-101-a2	0.136	0.001	1.51	0.09	1.38	0.01	0.91	21.30	0.50	1.83	60.09	5.58	0.760	79.07	7.54	189.4	109.6	0	59.4	9.22	
NE-101-a3	0.152	0.010	1.50	0.01	1.81	0.04	1.20	30.88	0.75	1.92	49.72	6.30	0.751	66.21	8.59	195.1	100.2	1	57.2	8.46	
NE-101-a4	1.550	0.050	16.30	0.16	2.05	0.02	0.13	32.65	0.66	16.77	75.83	5.10	0.688	110.22	7.61	166.2	82.4	2	45.1	2.16	
NE-101-a5	1.522	0.025	18.97	0.19	0.76	0.03	0.04	36.40	0.70	19.15	63.47	2.42	0.776	81.79	3.32	198.6	122.1	1	63.6	5.49	

Apatite fission-track compilation

Sample	Longitude	Latitude	Altitude (m)	Locality	Lithology	Crystallization/depositional age	Grains	Age (Ma)	±1σ	Ref.
CR-03	-38.067	-7.851	823	Triunfo (PE)	Syenite	Neoproterozoic	-	147	22	1
CR-04	-38.004	-7.86	484	Triunfo (PE)	Gneiss	Neoproterozoic	-	202	12	1
CR-13	-37.871	-8.079	611	Sitio dos Nunes (PE)	Granite	Neoproterozoic	-	211	19	1
CR-18	-36.937	-8.497	619	Pedra (PE)	Granite	Neoproterozoic	-	138	11	1
CR-20	-37.092	-8.408	640	Cruzeiro do Nordeste (PE)	Granite	Neoproterozoic	-	124	6	1
CR-25	-36.217	-8.881	531	Canhohnho (PE)	Granodiorite	Paleoproterozoic	-	68	6	1
CR-27	-35.846	-8.754	273	Jaqueira (PE)	Granite	Neoproterozoic	-	70	4	1
CR-30	-35.573	-8.681	120	Palmares (PE)	Ortho-gneiss	Paleoprotorozoic	-	69	5	1
CR-33	-38.72	-6.946	338	Cajazeiras (PB)	Milonitic gneiss	Neoproterozoic	-	130	11	1
CR-35	-39.478	-7.231	866	Exu Fm/Araripe Basin (CE)	Sandstone	Albian	-	109	6	1
CR-37	-39.743	-7.474	545	Exu (PE)		Neoproterozoic	-	184	19	1
CR-40	-38.782	-7.179	367	Barro (CE)	Coarse sandstone	Paleozoic	-	256	19	1
CR-41	-38.436	-6.664	332	Souza (PB)	Granite	Neoproterozoic	-	187	16	1
CR-45	-37.801	-5.63	93	Acu Fm/Potiguar Basin (RN)	Sandstone	Albian	-	71	5	1
CR-49	-37.905	-6.021	286	Serra do Martins (RN)	Granite	Neoproterozoic	-	76	8	1
CR-54	-37.166	-5.892	124	Triunfo Potiguar (RN)	Granite	Neoproterozoic	-	72	4	1
CR-97	-38.642	-4.976	223	Ibicutinga (CE)	Banded gneiss	Proterozoic	-	97	8	1
CR-132	-36.359	-5.581	184	Pedro Avelino (RN)	Diabase	Cretaceous	-	91	11	1
CR-133	-36.323	-5.708	503	Cabugi Peak (RN)	Micro-gabbro	late Oligocene	-	25	3	1
CR-135	-36.039	-5.654	200	Pedra Preta (RN)	Leucogabbro	Proterozoic	-	98	4	1
CR-136	-36.559	-6.215	394	Totoró (RN)	Leuco-norite	Proterozoic	-	107	5	1
CR-137	-37.198	-6.813	224	Ipueira (RN)	Leucogabbro	Proterozoic	-	99	4	1
CR-139	-38.384	-6.108	384	Dr. Severiano (RN)	Diorite	Proterozoic	-	159	10	1
CR-140	-36.367	-6.868	554	Cubati (PB)	Granite	Neoproterozoic	-	80	5	1
CR-141	-36.146	-7.22	540	Bravo, Boa Vista (PB)	Granite	Neoproterozoic	-	83	7	1
CR-143	-36.528	-7.497	508	Uruçu Farm, Serra Branca (PB)	Leucogabbro	Proterozoic	-	74	5	1
CR-146	-35.625	-6.343	174	Poço Verde (RN)	Leuco-norite	Proterozoic	-	93	4	1
TFTE-01	-37.274	-7.198	400	Teixeira (PB)	Granite	Neoproterozoic	-	85	7	1
TFTE-02	-37.274	-7.206	600	Teixeira (PB)	Granite	Neoproterozoic	-	71	5	1
TFTE-03	-37.253	-7.21	800	Teixeira (PB)	Granite	Neoproterozoic	-	73	6	1
TFPA-04	-37.276	-7.061	270	Patos (PB)	Granite	Neoproterozoic	-	78	7	1
TFTE-05	-37.387	-7.258	1000	Teixeira (PB)	Granite	Neoproterozoic	-	74	6	1
TFTE-06	-37.384	-7.252	1200	Teixeira (PB)	Granite	Neoproterozoic	-	77	5	1
MA-1	-35.695	-5.695	125	Poço Branco (RN)	Granite	Neoproterozoic	-	83	4	1
MA-3	-36.014	-5.592	160	Pedra Preta (RN)	Granite	Neoproterozoic	-	80	6	1
PAR-0301	-36.636	-6.698	250	Parelhas (RN)	Pegmatite	Neoproterozoic	-	60	5	1
94/74	-39.326	-8.077	460	Central Sector	Basement	Neoproterozoic	20	85	7	2
94/75	-39.457	-8.083	460	Central Sector	Basement	Neoproterozoic	21	76	4	2
94/76	-39.636	-8.108	450	Central Sector	Basement	Neoproterozoic	6	260	59	2
94/77	-39.734	-8.182	420	Central Sector	Basement	Neoproterozoic	20	143	13	2
94/78	-39.834	-8.257	440	Meridional Sector	Basement	Neoproterozoic	20	173	9	2
94/79	-40.011	-8.546	475	Meridional Sector	Basement	Paleoproterozoic	20	182	8	2
94/7	-37.448	-10.657	205		Basement		19	104	4	2
PP-122	-35.074	-8.102		Guarani Quarry	Gneiss	Precambrian	-	95	4	3
PP-94	-35.088	-8.194		Anhaguera Quarry	Granite	Precambrian	-	80	5	3
PP-515	-35.11	-8.292		Tapera Mill	Gneiss	Precambrian	-	94	5	3
PP-73A	-35.132	-8.352		Rio Formosa (PE)	Granite	Precambrian	-	84	6	3
PP-207A	-35.161	-8.456		Cruzeiro Hill	Gneiss	Precambrian	-	85	4	3
PP-213	-35.188	-8.562		Barrelros (PE)	Granite	Precambrian	-	110	8	3
PP-05	-35.131	-8.589		Herval Quarry	Porphytitic Granite	Precambrian	-	90	6	3
RD57-37	-39.305	-7.14	389	Caririacu (CE)	Tonalite	Neoproterozoic	20	286.6	23.4	4
RD57-38	-39.358	-7.328	423	R.Batateira Fm/Araripe Basin	Sandstone	Aptian	4	249.5	70.8	4
RD57-40	-39.335	-7.372	834	Exu Fm/Araripe Basin	Sandstone	Albian	20	131.7	12.7	4
RD57-41	-39.315	-7.546	812	Exu Fm/Araripe Basin	Sandstone	Albian	20	164.2	21.1	4
RD57-42	-39.172	-7.66	490	Mauriti Fm/Cedro Basin	Coarse sandstone	Silurian-Ordovician	20	169.7	30.3	4
RD57-43	-38.982	-7.717	482	Mauriti Fm/Cedro Basin	Coarse sandstone	Silurian-Ordovician	6	194	45.2	4
RD57-2	-36.583	-5.311	42	Tibau Frn/Potiguar Basin (RN)	Coarse sandstone	Paleocene/Oligocene?	5	134.7	30.5	5
RD57-3	-36.537	-5.468	49	Açu Fm/Potiguar Basin (RN)	Sandstone	Cenomanian	20	86.8	10	5
RD57-8	-36.535	-6.024	650	Serra do Martins Fm/Santana mesa (RN)	Coarse sandstone	Paleocene/Oligocene?	20	117.9	11	5
RD57-34	-36.592	-6.124	687	Serra do Martins Fm/Santana mesa (RN)	Coarse sandstone	Paleocene/Oligocene?	20	84.6	6.5	5
RD57-35	-36.774	-6.036	600	Serra do Martins Fm/Santana mesa (RN)	Coarse sandstone	Paleocene/Oligocene?	20	79.1	4.5	5
RD57-4	-36.588	-5.638	124	Angicos (RN)	Granite	Neoproterozoic	20	98.9	8.4	6
RD57-9	-36.521	-6.173	368	Currais Novos (RN)	Orthogneiss	Neoproterozoic	20	102.1	13.1	6
RD57-11	-36.64	-6.504	279	Acari batholith (RN)	Granite	Neoproterozoic	20	108.5	7.1	6
RD57-15	-37.12	-6.95	281	São Mamede (PB)	Migmatite	Paleoproterozoic	20	102	6.2	6
RD57-17	-37.261	-7.201	722	Teixeira batholith (PB)	Granite	Neoproterozoic	21	93.6	12	6
RD57-18	-37.375	-7.331	771	Teixeira batholith (PB)	Granite	Neoproterozoic	20	71.1	5.9	6
RD57-21	-37.846	-7.594	692	Teixeira batholith (PB)	Granite	Neoproterozoic	20	82.2	7	6
RD57-23	-38.107	-7.84	1075	Triunfo (PE)	Syenite	Neoproterozoic	20	173.3	24.1	6
RD57-24	-38.166	-7.943	475	Serra Talhada (PE)	Gneiss	Neoproterozoic	20	123.5	9	6
RD57-26	-35.115	-6.829	19	Mamanguape (PB)	Granite	Neoproterozoic	20	97.2	8.2	6
RD57-29	-35.634	-6.756	524	Solânea mesa (PB)	Granite	Neoproterozoic	20	66.8	8.1	6
RD57-31	-35.96	-6.658	436	Barra de Santa Rosa (PB)	Gneiss	Paleoproterozoic	21	52.1	4.4	6
RD57-33	-36.268	-6.464	616	Cutiê mesa (PB)	Gneiss	Paleoproterozoic	20	85.9	6.8	6
RD57-36	-36.936	-6.002	107	Jucurutu (RN)	Granite	Neoproterozoic	20	97.3	6.6	6
GC854-14	-36.817	-9.883	150-300		Granite	Precambrian	20	81.3	6.8	7
GC854-16	-36.7	-9.717	150-300		Granite	Precambrian	17	140.7	22.6	7
GC854-17	-36.883	-9.667	150-300		Granite	Precambrian	13	97.1	13.9	7

Sample	Lon	Lat	Range	Unit	Rock	Age	n	Value	Err	Grp
GC854-19	-36.417	-9.583	150-300		Granite	Precambrian	18	108.4	7.7	7
GC854-20	-36.267	-9.567	150-300		Granite	Precambrian	20	86.5	6	7
GC854-7	-38.567	-10.017	150-300		Sandstone	Early Cretaceous	9	244.4	21.7	7
GC854-11	-38.367	-10.117	150-300		Sandstone	Early Cretaceous	20	327.9	41.7	7
JT4	-38.317	-10.117	150-300		Arkose	Early Cretaceous	20	264	20	7
JT5	-38.317	-10.167	150-300		Arkose	Early Cretaceous	20	267	21	7
Seal-3	-37.039	-10.733	252		Migmatite		2	140	37	8
Seal-4	-37.434	-10.764	178		Gneiss		12	113	15	8
Seal-5	-37.358	-10.618	176		Migmatite		11	156	21	8
Seal-7	-36.935	-10.15	90		Syenogranite		3	91	22	8
Seal-10	-37.404	-9.694	174		Syenogranite		18	120	12	8
Seal-11	-37.277	-9.473	305		Granite		10	102	12	8
Seal-12	-36.82	-9.888	238		Gneiss		5	96	19	8
Seal-13	-36.444	-8.813	701		Gneiss		13	122	15	8
Seal-14	-35.931	-8.467	442		Gneiss		18	109	11	8
Seal-15	-35.516	-8.955	101		Granite		15	109	11	8
Seal-16	-35.679	-8.982	243		Gneiss		9	102	13	8
Seal-17	-35.758	-9.249	128		Gneiss		12	91	9	8
Seal-18	-36.906	-10.393	155		Granite		11	108	13	8
AFTA8	-38.563	-8.996	358		Granodiorite		20	175	19	9
AFTA9	-38.167	-9.489	240		Granite		20	167	18	9
AFTA10	-37.905	-9.35	286		Diorite		20	160	17	9
AFTA11	-38.241	-9.247	285		Migmatite		20	175	22	9
AFTA12	-38.204	-9.461	233		Granite		20	170	21	9
AFTA15	-38.103	-9.843	338		Granite		20	140	14	9
AFTA48	-38.988	-9.223	409		Granite		20	147	20	9
AFTA55	-37.897	-9.696	206		Granite		20	145	13	9
AFTA56	-37.673	-10.26	268		Gnaisse		20	199	29	9
AFTA52B	-38.693	-9.319	446		Sandstone		90	312	17	9
TF1137	-40.144	-4.2		Suíte Tamboril-Santa Quitéria (CE)	Granite	Neoproterozoic	27	80	8	10
TF1139	-39.974	-4.519		Suíte Tamboril-Santa Quitéria (CE)	Ortognaisse	Neoproterozoic	30	105	16	10
TF1141	-39.551	-4.839		Complexo Cruzeta (CE)	Granite	Eoarchean	25	184	19	10
TF1143	-39.195	-5.145		Pluton Quixeramobim-Quixada (CE)	Granite	Neoproterozoic	27	122	12	10
TF1146	-38.545	-5.828		Suite Jaguaretama (CE)	Ortognaisse	Paleoproterozoic	29	145	16	10
TF1148	-38.168	-6.098		Suite Jaguaretama (RN)	Granite	Paleoproterozoic	27	205	33	10
TF1150	-37.755	-6.337		Pluton Catolé do Rocha (PB)	Granite	Neoproterozoic	25	95	11	10
TF1152	-37.387	-6.67		Suite Poço da Cruz (RN)	Granite	Paleoproterozoic	25	128	22	10
TF1154	-36.727	-6.969		Gp Seridó (RN)	Bt Gnaisse	Neoproterozoic	28	121	13	10
TF1156	-36.233	-7.254		Comple-o São Caetano (PB)	Bt Gnaisse	Mesoproterozoic	30	106	14	10
TF1158	-35.778	-7.551		Complexo Sertânia (PB)	Bt Gnaisse	Paleoproterozoic	27	147	21	10
TF1161	-34.975	-7.997		Complexo Salgadinho (PE)	Granite	Paleoproterozoic	25	144	30	10
1	-37.398	-5.701	100		Granite	Neoproterozoic	23	113	24	11
2	-37.603	-5.756	100		Granite	Neoproterozoic	10	152	28	11
3	-37.991	-6.008	550		Granite	Neoproterozoic	112	312	51	11
4	-38.192	-6.136	200		Granite	Neoproterozoic	41	376	63	11
5	-38.255	-6.182	200		Granite	Neoproterozoic	68	323	54	11
7	-38.475	-6.215	650		Granite	Neoproterozoic	19	140	30	11
8	-38.461	-6.255	550		Granite	Neoproterozoic	71	237	41	11
9	-38.473	-6.294	450		Granite	Neoproterozoic	40	213	36	11
10	-38.67	-6.532	400		Granite	Neoproterozoic	70	181	30	11
11	-38.375	-6.496	350		Granite	Neoproterozoic	35	151	25	11
12	-38.201	-6.331	250		Granite	Neoproterozoic	99	86	14	11
13	-37.363	-5.716	150		Sandstone	Neoproterozoic	96	125	21	11
14	-37.411	-5.788	150		Granite	Neoproterozoic	69	117	20	11
15	-37.77	-5.92	150		Granite	Neoproterozoic	11	108	23	11
16	-37.877	-6.049	600		Granite	Neoproterozoic	136	107	18	11
17	-37.954	-6.044	450		Granite	Neoproterozoic	10	106	23	11
18	-38.164	-6.335	250		Granite	Neoproterozoic	55	90	18	11
SP06	-38.579	-4.44	103		Basement		17	111.6	22.8	12
SP44	-39.22	-5.284	247		Basement		12	108.2	8.8	12
SP18	-38.635	-4.729	171		Basement		41	96.1	8.1	12
SP11	-38.504	-4.59	94		Basement		37	94.6	9.4	12
SP23	-38.865	-4.766	180		Basement		102	91	6.1	12
SP24	-39.038	-4.957	212		Basement		53	36.5	6.9	12
SP41	-38.999	-5.196	153		Basement		40	62.9	6.3	12
SP12	-38.582	-4.659	141		Basement		7	64.1	11.8	12
SP04	-38.399	-4.496	63		Basement		94	67.3	5.9	12
SP36	-39.085	-5.099	224		Basement		58	67.6	8.8	12
SP34	-38.922	-4.854	217		Basement		42	70.1	7.6	12
30	-38.281	-10.084				Upper Jurassic	-	199.2	25.6	13
31	-38.207	-10.088				Upper Jurassic	-	357.2	37.7	13
32	-38.176	-10.087				Paleozoic	-	186.3	25.3	13
33	-38.173	-10.088				Paleozoic	-	246.3	29.5	13
34	-38.114	-10.087				Precambrian	-	213.9	27.9	13
119	-37.609	-9.929				Precambrian	-	87.8	8.1	13
120	-37.761	-9.638				Precambrian	-	140.3	15.7	13
122	-37.988	-9.368				Precambrian	-	121.6	7.5	13
123	-38.424	-9.43				Upper Jurassic	-	231.9	32.2	13
125	-37.807	-9.511				Devonian?	-	338.3	25.8	13
126	-37.515	-10.13				Precambrian	-	109.6	7.4	13
128	-37.436	-10.707				Precambrian	-	119	8.7	13

References

1. Galindo, A.C., Oliveira, M.J. R., 2006. Distribuição dos sedimentos cenozóicos nas bacias Pernambuco-Paraíba, Potiguar e Ceará, como função da epirogenia cenozóica da Província Borborema. Projeto CRONOBORO: UFRN-PPGG/PETROBRAS. Unpublished Report. Natal, Brasil, 335 p., 2 vol.

2. Harman, R., Gallagher, K., Brown, R., Raza, A., Bizzi, L., 1998. Accelerated denudation and tectonic/geomorphic reactivation of the cratons of northeastern Brazil during the Late Cretaceous. J. Geophys. Res. Solid Earth 103, 27091–27105.

3. Jardim de Sá, E.F. (coord) et al., 2003. Projeto Avaliação do Potencial Petrolífero da Bacia Pernambuco-Paraíba. Unpublished report. Universidade Federal do Rio Grande do Norte-Agência Nacional do Petróleo, Natal, Brasil.

4. Morais Neto, J.M., Hegarty, K., Karner, G.D., 2005. Abordagem preliminar sobre paleotemperatura e evolução do relevo da Bacia do Araripe, Nordeste do Brasil, a partir da análise de traços de fissão em apatita. Bol. Geociencias da Petrobras 14, 113–119.

5. Morais Neto, J.M., Green, P.F., Karner, G.D., De Alkmim, F.F., 2008. Age of the Serra Do Martins formation, Borborema plateau, northeastern Brazil: Constraints from apatite and zircon fission track analysis. Bol. Geociencias da Petrobras 16, 23–52.

6. Morais Neto, J.M., Hegarty, K.A., Karner, G.D., Alkmim, F.F., 2009. Timing and mechanisms for the generation and modification of the anomalous topography of the Borborema Province, northeastern Brazil. Mar. Pet. Geol. 26, 1070–1086. https://doi.org/10.1016/j.marpetgeo.2008.07.002

7. Turner, J.P., Green, P.F., Holford, S.P., Lawrence, S.R., 2008. Thermal history of the Rio Muni (West Africa)-NE Brazil margins during continental breakup. Earth Planet. Sci. Lett. 270, 354–367. https://doi.org/10.1016/j.epsl.2008.04.002

8. Jelinek, A.R., Chemale, F., van der Beek, P.A., Guadagnin, F., Cupertino, J.A., Viana, A., 2014. Denudation history and landscape evolution of the northern East-Brazilian continental margin from apatite fission-track thermochronology. J. South Am. Earth Sci. 54, 158–181. https://doi.org/10.1016/j.jsames.2014.06.001

9. Jelinek, A.R., Corrêa-Gomes, L.C., Bicca, M.M., 2020. Evolução termotectônica fanerozoica da margem continental na área do Rifte Recôncavo-Tucano-Jatobá. Pesqui. em Geociências 47. https://doi.org/10.22456/1807-9806.101330

10. Mojzeszowicz, A.G., 2009. Evolução Da Tectônica Rúptil No Nordeste Do Brasil Baseada Na Termocronologia Por Traço De Fissão Em Apatita. Undergraduate dissertation. Universidade Estadual Paulista.

11. Nóbrega, M.A., Sá, J.M., Bezerra, F.H.R., Hadler Neto, J.C., Iunes, P.J., Guedes, S., Tello Saenz, C.A., Hackspacher, P.C., Lima-Filho, F.P., 2005. The use of apatite fission track thermochronology to constrain fault movements and sedimentary basin evolution in northeastern Brazil. Radiat. Meas. 39, 627–633. https://doi.org/10.1016/j.radmeas.2004.12.006

12. Cavalcante, A.S.Á., 2006. Evolução Termocronológica do Sistema de Falhas Senador Pompeu - CE. Master dissertation. Universidade Federal do Rio Grande do Norte.

13. Japsen, P., Bonow, J.M., Green, P.F., Cobbold, P.R., Chiossi, D., Lilletveit, R., Magnavita, L.P., Pedreira, A., 2012. Episodic burial and e-humation in NE Brazil after opening of the South Atlantic. Bull. Geol. Soc. Am. 124, 800–816. https://doi.org/10.1130/B30515.1

^{40}Ar/^{39}Ar compilation

ID	Longitude	Latitude	Approach	Local	Lithology	Unit	Material	Age (Ma)	±2σ	Ref
CM-12	35.76438	5.62938	Plateau		Tholeiite	Mafic dike	plagioclase	127.1	1.3	1
JUPI-1	36.46496	8.73225	Minimum age		Orthogneiss	Jupi orthogneiss	biotite	540		2
CAC-2	36.24319	8.5219	Plateau a		Syenite	Cachoeirinha pluton	biotite	552	5	2
BA-10	35.94766	8.31298	spectrum		Orthogneiss	Caruaru Orthogneiss	biotite	546	6	2
SCC-7	36.17883	7.90892	Plateau		Monzonite	Santa Cruz do Capibaribe pluton	biotite	509	5	2
SCC-4	36.04736	7.70904	Maximum age		Orthogneiss	Alcantil Orthogneiss	amphibole	536		2
SCC-4	36.04736	7.70904	Plateau		Orthogneiss	Alcantil Orthogneiss Paleoproterozoic	biotite	519	5	2
SCC-5	36.15146	7.7025	Plateau		metagranodiorite	metagranodiorite	biotite	533	5	2
VD-4B	36.29687	5.76592	Isochron		Alkaline basalt	Cabugizinho	groundmass	7.5	0.3	3
VD-5A	36.29654	5.76526	Isochron		Alkaline basalt	Cabugizinho	groundmass	7.6	0.4	3
VD-08	36.33365	5.64059	Isochron		Alkaline basalt	Caracarazinho	groundmass	8.9	0.5	3
SP-7	36.45419	5.90776	Isochron		Alkaline basalt	Serra Preta of Bodó	groundmass	7.1	0.3	3
CN-11	36.43729	5.79118	Isochron		Alkaline basalt	Cabelo de Negro	groundmass	7.9	0.3	3
SBE-95	37.23	9.928621	Average		Quartzite	Macururé domain	muscovite	591	4	4
SBE-122	39.0613119	9.215631	Average		Mylonitic quartzite	Macururé domain	muscovite	581	2	4
SBE-38A	38.069169	9.825777	Average		Amphibolite	Marancó sub-domain	amphibole	625	3	4
SBE-33M	37.842293	9.87463	Average		garnet-muscovite schist	Marancó sub-domain	muscovite	612	7	4
4505-01	37.012217	7.558376	Plateau		mylonite	West Coixola shear zone	muscovite	511.2	1.8	5
5052-01	36.764753	7.590737	Plateau		mylonite	West Coixola shear zone	muscovite	510	5	5
4494-01	37.044577	7.685916	Plateau		gabbro	Prata mafic stock	amphibole	547	2	5
4493-01	37.044577	7.685916	Plateau		gabbro	Prata mafic stock	Biotite	530	2	5
4504-01	35.93099	7.596447	Plateau		mylonite	East Coixola shear zone	muscovite	548	2	5
4503-01	35.814872	7.585026	Plateau		mylonite	East Coixola shear zone	muscovite	547	4	5
EM	36.63	6.68888889	Plateau		Pegmatite	Parelhas	biotite	523.4	1.1	6
FCA/08A	36.285555	6.20166667	Plateau		Mylonitic micaschist	Seridó group	muscovite	504.6	1.5	6
FCA/08B	36.285555	6.20166667	Plateau		Mylonitic micaschist	Seridó group	muscovite	501	1.6	6
FCA/11A	36.2875	6.20361111	Plateau		Quartz vein	Seridó group	muscovite	500.2	1.5	6
FCA/11B	36.2875	6.20361111	Plateau		Quartz vein	Seridó group	biotite	500	2	6
FCA/15	37.1916667	6.44833333	Plateau		Altered mylonitic gneiss	Caicó Complex	muscovite	505.9	1.3	6
FCA/16	37.1725	6.40138888	Plateau		Altered granite	Caicó Complex	muscovite	520	3	6
TQ-25	36.100731	7.912677	Plateau		Metadiorite	Caruaru	amphibole	584.2	3.7	7
TQ-25	36.100731	7.912677	Plateau		Metadiorite	Caruaru	biotite	545.3	1.1	7
TQ-4A	36.024351	7.904825	Plateau		Orthogneiss	Taquaritinga	biotite	553.4	1.1	7
TQ-321	36.053618	8.001193			Gneiss	Toritama pluton	amphibole	595.5	1.2	7
TQ-57	36.093593	8.134681			Gneiss	Fazenda Nova Shear Zone	amphibole	552.8	1.81	7
TQ-57	36.093593	8.134681	Plateau		Gneiss	Fazenda Nova Shear Zone	biotite	533	1.1	7
TQ-485	36.028634	8.292439			Gneiss	East Pernambuco Shear zone	biotite	545	1.1	7
TV	37.958455	7.637387	Ideogram		Epidote-bearing granite	Tavares	biotite	538.1	1.6	8
TV	37.958455	7.637387	Ideogram		Epidote-bearing granite	Tavares	amphibole	604	7	8
BRE-07	37.262463	7.323298	Plateau age		Epidote-bearing granite	Brejinho	biotite	510	5	8
BRE-07	37.262463	7.323298	Ideogram		Epidote-bearing granite	Brejinho	amphibole	572	2	8
CR-41	38.4361111	6.66377778	Plateau	Rio Piranhas Massif	granite	Paraná Pulton	amphibole	575	5	9
CR-41	38.4361111	6.66377778	Plateau	Rio Piranhas Massif	granite	Paraná Pulton	amphibole	564	6	9
CR-41	38.4361111	6.66377778	Plateau	Rio Piranhas Massif	granite	Paraná Pulton	biotite	531	5	9
CR-41	38.4361111	6.66377778	Plateau	Rio Piranhas Massif	granite	Paraná Pulton	biotite	546	5	9
CR-41	38.4361111	6.66377778	Plateau	Rio Piranhas Massif	granite	Paraná Pulton	k-feldspar	514	6	9
CR-54	37.1664722	5.89216667	Plateau	Northern domain	granite	Rio Piranhas Massif	biotite	521	7	9
CR-54	37.1664722	5.89216667	Plateau	Northern domain	granite	Rio Piranhas Massif	biotite	516	6	9
CR-54	37.1664722	5.89216667	Plateau	Northern domain	granite	Rio Piranhas Massif	k-feldspar	389	6	9
EM-1	36.63	6.70555556	Plateau	Northern domain	pegmatite	Seridó	k-feldspar	479	16	9
LG-157	35.6635833	6.3041388	Plateau	Northern domain	mylonitic orthogneiss	S José do Campestre massif	amphibole	560	6	9
LG-157	35.6635833	6.3041388	Plateau	Northern domain	mylonitic orthogneiss	S José do Campestre massif	amphibole	569	6	9
LG-157	35.6635833	6.3041388	Plateau	Northern domain	mylonitic orthogneiss	S José do Campestre massif	biotite	546.4	4	9
LG-157	35.663583	6.3041388	Plateau	Northern domain	mylonitic orthogneiss	S José do Campestre massif	biotite	538	4	9
LG-157	35.6635833	6.3041388	Plateau	Northern domain	mylonitic orthogneiss	S José do Campestre massif	k-feldspar	506	6	9
MFG-3	36.7630278	5.75219444	Plateau	Northern domain	granitic orthogneiss	Seridó	biotite	456	8	9
MFG-3	36.7630278	5.75219444	Plateau	Northern domain	granitic orthogneiss	Seridó	biotite	267	7	9
MFG-3	36.7630278	5.75219444	Plateau	Northern domain	granitic orthogneiss	Seridó	k-feldspar	433	4	9
MFG-7B	36.8030833	5.65608333	Plateau	Northern domain	meta-pegmatite	Rio Piranhas Massif	biotite	471	19	9
MFG-7B	36.8030833	5.65608333	Plateau	Northern domain	meta-pegmatite	Rio Piranhas Massif	biotite	490	9	9
MFG-7B	36.8030833	5.65608333	Plateau	Northern domain	meta-pegmatite	Rio Piranhas Massif	k-feldspar	464	6	9
SF-11	36.5111389	5.56325	Plateau	Northern domain	Epidote-bearing granite	Seridó - Flores pluton	biotite	503.4	4	9
SF-11	36.5111389	5.56325	Plateau	Northern domain	Epidote-bearing granite	Seridó - Flores pluton	biotite	505	4	9
SF-11	36.5111389	5.56325	Plateau	Northern domain	Epidote-bearing granite	Seridó - Flores pluton	k-feldspar	404	5	9
BRE-07	37.2097222	7.37611111	Plateau	Transversal Zone	Epidote-bearing granodiorite	Alto Pajeú - Itapetim pluton	k-feldspar	467	7	9
CR-13	37.8712778	8.07922222	Plateau	Transversal Zone	Shoshonitic granite	Alto Moxotó	biotite	577	5	9
CR-13	37.8712778	8.07922222	Plateau	Transversal Zone	Shoshonitic granite	Alto Moxotó	biotite	562	5	9
CR-13	37.8712778	8.07922222	Plateau	Transversal Zone	Shoshonitic granite	Alto Moxotó	k-feldspar	513	6	9
CR-37	39.7431111	7.47352778	Plateau	Transversal Zone	epidote-free granodiorite	Bodocó pluton	biotite	545	5	9
CR-37	39.7431111	7.47352778	Plateau	Transversal Zone	epidote-free granodiorite	Bodocó pluton	biotite	540	6	9
CR-37	39.7431111	7.47352778	Plateau	Transversal Zone	epidote-free granodiorite	Bodocó pluton	k-feldspar	494	4	9

					epidote-free					
MC-35	38.9041667	7.55555556	Plateau	Transversal Zone	granodiorite	Maxixe pluton	k-feldspar	562	9	9
TV	37.9069444	7.67583333	Plateau	Transversal Zone	porphyritic granite	Tavares pluton	k-feldspar	500	6	9
028-JAB	37.3875	7.26555555	Plateau	Transversal Zone	shoshonitic granite	Teixeira batholith	k-feldspar	484	10	9
CR-18	36.9368333	8.49658333	Plateau	Southern domain	granite	PEAL	biotite	563	6	9
CR-18	36.9368333	8.49658333	Plateau	Southern domain	granite	PEAL	biotite	557	7	9
CR-18	36.9368333	8.49658333	Plateau	Southern domain	granite	PEAL	k-feldspar	506	6	9
CR-25	36.2171111	8.88069444	Plateau	Southern domain	granodiorite	PEAL	biotite	532	9	9
CR-25	36.2171111	8.88069444	Plateau	Southern domain	granodiorite	PEAL	biotite	530	8	9
CR-25	36.2171111	8.88069444	Plateau	Southern domain	granodiorite	PEAL	muscovite	550	8	9
CR-25	36.2171111	8.88069444	Plateau	Southern domain	granodiorite	PEAL	muscovite	550	8	9
CR-25	36.2171111	8.88069444	Plateau	Southern domain	granodiorite	PEAL	k-feldspar	490	7	9
CR-30	35.5734722	8.68105556	Plateau	Southern domain	paleoproterozoic banded gneiss	PEAL	biotite	529	4	9
CR-30	35.5734722	8.68105556	Plateau	Southern domain	paleoproterozoic banded gneiss	PEAL	biotite	522	4	9
CR-30	35.5734722	8.68105556	Plateau	Southern domain	paleoproterozoic banded gneiss	PEAL	k-feldspar	511	4	9
COR2	38.0628323	6.9938491	Plateau		metatexite	Coremas	amphibole	565	2	10
COR2	38.0628323	6.9938491	Plateau		metatexite	Coremas	amphibole	566.5	1.7	10
COR2	38.0628323	6.9938491	Plateau		metatexite	Coremas	biotite	549.6	1.6	10
CAJ3	38.5802163	6.92818074	Plateau		diatexite	Cajazeiras	biotite	542.1	1.6	10
CAJ3	38.5802163	6.92818074	Plateau		diatexite	Cajazeiras	biotite	544	1.4	10
CIPA	38.659835	6.840867	Plateau		diatexite	Cajazeiras	biotite	533.4	1.4	10
CIPA	38.659835	6.840867	Plateau		diatexite	Cajazeiras	biotite	533.5	1.4	10
2a	36.3208333	5.7013888	Plateau		basalt	Cabugi neck	groundmass	24.6	0.8	11
	36.3208333	5.7013888	Plateau		basalt	Cabugi neck	groundmass	23.7	1.2	12
	36.3625	5.96666667	Plateau		basalt	Serra Preta	groundmass	29.7	0.6	12
P31-D9	36.2291667	5.97777778	Plateau		basalt	Serrote Preto	groundmass	24.2	0.3	13
15BP3-2	36.186245	7.37070033	Plateau	Queimadas	Alkaline basalt	Macau-Queimadas	groundmass	21.09	0.05	14
15BP3-3b	36.1722661	7.33719128	Plateau	Juá quarry	basaltic andesite	Macau-Queimadas	groundmass	22.5	0.32	14
15BP3-5	36.2761663	6.76058901	Plateau	Cubati	basalt	Macau-Queimadas	groundmass	24.5	0.08	14
15BP5-8	36.205036	6.10869093	Plateau	Socavão	basanite	Macau-Queimadas	groundmass	33.99	0.09	14
15BP5-9	36.099167	5.93076583	Plateau	Carnaubinha	basanite	Macau-Queimadas	groundmass	33.91	0.94	14
15BP5-10	36.2270977	5.96340884	Plateau	Serrote Preto	basanite	Macau-Queimadas	groundmass	29.29	0.11	14
15BP7-14	36.6544121	5.2099372	Plateau	Macau	basaltic andesite	Macau-Queimadas	groundmass	21.6	0.58	14
15BP7-15	36.33242	5.47906325	Plateau	Serra Preta	nephelinite	Macau-Queimadas	groundmass	12.39	0.24	14
15BP9-19a	38.4267489	3.8170394	Plateau	Caruru quarry	phonolite	Mecejana	sanidine	33.48	0.15	14
15BP9-19c	38.4267489	3.8170394	Plateau	Caruru quarry	phonolite	Mecejana	groundmass	32.96	0.15	14
15BP10-20(b)	38.5226085	3.8861327	Plateau	Ancurí	phonolite	Mecejana	sanidine	30.8	0.22	14
15BP10-21a	38.8284463	3.8888561	Plateau	Pão de Açucar	phonolite	Mecejana	sanidine	33.94	0.25	14
15BP10-21b	38.8284463	3.8888561	Plateau	Pão de Açucar	phonolite	Mecejana	sanidine	35.03	0.28	14
15BP10-22(b)	38.775482	3.9586217	Plateau	Japarara	phonolite	Mecejana	sanidine	34.92	0.27	14
15BP10-23	38.854702	3.78563617	Plateau	Salgadinho	phonolite	Mecejana	sanidine	34.61	0.23	14

References

1. Ngonge, E. D., de Hollanda, M. H. B. M., Archanjo, C. J., de Oliveira, D. C., Vasconcelos, P. M. P., & Muñoz, P. R. M. (2016). Petrology of continental tholeiitic magmas forming a 350-km-long Mesozoic dyke swarm in NE Brazil: Constraints of geochemical and isotopic data. *Lithos, 258*, 228-252.

2. Neves, S. P., Monié, P., Bruguier, O., & da Silva, J. M. R. (2012). Geochronological, thermochronological and thermobarometric constraints on deformation, magmatism and thermal regimes in eastern Borborema Province (NE Brazil). *Journal of South American Earth Sciences, 38*, 129-146.

3. Knesel, K. M., Souza, Z. S., Vasconcelos, P. M., Cohen, B. E., & Silveira, F. V. (2011). Young volcanism in the Borborema Province, NE Brazil, shows no evidence for a trace of the Fernando de Noronha plume on the continent. *Earth and Planetary Science Letters*, *302*(1-2), 38-50.

4. Oliveira, E. P., Windley, B. F., & Araújo, M. N. (2010). The Neoproterozoic Sergipano orogenic belt, NE Brazil: a complete plate tectonic cycle in western Gondwana. *Precambrian Research, 181*(1-4), 64-84.

5. Hollanda, M. H. B., Archanjo, C. J., Souza, L. C., Armstrong, R., & Vasconcelos, P. M. (2010). Cambrian mafic to felsic magmatism and its connections with transcurrent shear zones of the Borborema Province (NE Brazil): implications for the late assembly of the West Gondwana. *Precambrian Research, 178*(1-4), 1-14.

6. Araújo, M. N. C., Vasconcelos, P. M., da Silva, F. C. A., de Sá, E. F. J., & Sá, J. M. (2005). ^{40}Ar/^{39}Ar geochronology of gold mineralization in Brasiliano strike-slip shear zones in the Borborema province, NE Brazil. *Journal of South American Earth Sciences, 19*(4), 445-460.

7. Neves, S. P., Vauchez, A., & Feraud, G. (2000). Tectono-thermal evolution, magma emplacement, and shear zone development in the Caruaru area (Borborema Province, NE Brazil). *Precambrian research, 99*(1-2), 1-32.

8. Sial, A. N., Vasconcelos, P. M., Ferreira, V. P., Pessoa, R. R., Brasilino, R. G., & Neto, J. M. M. (2008). Geochronological and mineralogical constraints on depth of emplacement and ascencion rates of epidote-bearing magmas from northeastern Brazil. *Lithos, 105*(3-4), 225-238.

9. Morais Neto, J. M. (2009). Thermochronology, landscape evolution and denudational history of the eastern Borborema Province, northeastern Brazil. Doctoral thesis. The University of Queensland.

10. Archanjo, C. J., Hollanda, M. H. B. M. D., & Viegas, L. G. F. (2021). Late Ediacaran lateral-escape tectonics as recorded by the Patos shear zone (Borborema Province, NE Brazil). *Brazilian Journal of Geology, 51*.

11. Souza, Z. S., Vasconcelos, P. M., Nascimento, M. A. L., Silveira, F. V., Paiva, H. S., Dias, L. G. S., ... & Carmo, I. O. (2003). ^{40}Ar/^{39}Ar geochronology of Mesozoic and Cenozoic magmatism in NE Brazil. In Short Papers of the IV South American Symposium on Isotope Geology (Vol. 2).

12. Araújo, M. G. D. S., Brito Neves, B. B. D., & Archanjo, C. J. (2001). Idades Ar/Ar do magmatismo básico mesocenozóico da província Borborema oriental, nordeste do Brasil. Resumos. XIX Simpósio de Geologia do Nordeste - Natal/RN.

13. Menezes, M. R. F., JM, M. N., Szatmari, P., & York, D. (2003). Relações cronológicas entre o vulcanismo Macau e a Formação Serra do Martins com base na datação Ar/Ar do plug basáltico "Serrote Preto"(RN, Nordeste do Brasil). IX Simpósio Nacional de Estudos Tectônicos, Búzios, Annals, 246-249.

14. Guimarães, A. R., Fitton, J. G., Kirstein, L. A., & Barfod, D. N. (2020). Contemporaneous intraplate magmatism on conjugate South Atlantic margins: A hotspot conundrum. *Earth and Planetary Science Letters, 536*, 116147